Probing the Pathways of Free Charge Generation and Recombination in Organic Solar Cells: The Role of Excess Energy and Dispersive Effects.

Kumulative Dissertation

zur Erlangung des akademischen Grades
doctor rerum naturalium (Dr. rer. nat.)
in der Wissenschaftsdisziplin Experimentalphysik

Eingereicht an der
Mathematisch-Naturwissenschaftlichen Fakultät
der Universität Potsdam
Institut für Physik und Astronomie

von

Dipl. Phys. Jona Kurpiers

Ort und Tag der Disputation: Potsdam, 15. Mai 2019

Hauptbetreuer: Prof. Dr. Dieter Neher
Zweitbetreuer: Prof. Dr. Matias Bargheer
Gutachter*innen: Prof. Dr. Natalie Banerji
Prof. Dr. Carsten Deibel
Prof. Dr. Dieter Neher

Published online at the
Institutional Repository of the University of Potsdam:
https://doi.org/10.25932/publishup-42909
https://nbn-resolving.org/urn:nbn:de:kobv:517-opus4-429099

Abstract

Organic semiconductors are a promising class of materials. Their special properties are the particularly good absorption, low weight and easy processing into thin films. Therefore, intense research has been devoted to the realization of thin film organic solar cells (OPVs). Because of the low dielectric constant of organic semiconductors, primary excitations (excitons) are strongly bound and a type II heterojunction needs to be introduced to split these excitations into free charges. Therefore, most organic solar cells consist of at least an electron donor and electron acceptor material. For such donor acceptor systems mainly three states are relevant; the photoexcited exciton on the donor or acceptor material, the charge transfer state at the donor-acceptor interface and the charge separated state of a free electron and hole. The interplay between these states significantly determines the efficiency of organic solar cells. Due to the high absorption and the low charge carrier mobilities, the active layers are usually thin but also, exciton dissociation and free charge formation proceeds rapidely, which makes the study of carrier dynamics highly challenging. Therefore, the focus of this work was first to install new experimental setups for the investigation of the charge carrier dynamics in complete devices with superior sensitivity and time resolution and, second, to apply these methods to prototypical photovoltaic materials to address specific questions in the field of organic and hybrid photovoltaics. Regarding the first goal, a new setup combining transient absorption spectroscopy (TAS) and time delayed collection field (TDCF) was designed and installed in Potsdam. An important part of this work concerned the improvement of the electronic components with respect to time resolution and sensitivity. To this end, a highly sensitive amplifier for driving and detecting the device response in TDCF was developed. This system was then applied to selected organic and hybrid model systems with a particular focus on the understanding of the loss mechanisms that limit the fill factor and short circuit current of organic solar cells. The first model system was a hybrid photovoltaic material comprising inorganic quantum dots decorated with organic ligands. Measurements with TDCF revealed fast free carrier recombination, in part assisted by traps, while bias-assisted charge extraction measurements showed high mobility. The measured parameters then served as input for a successful description of the device performance with an analytical model. With a further improvement of the

instrumentation, a second topic was the detailed analysis of non-geminate recombination in a disordered polymer:fullerene blend where an important question was the effect of disorder on the carrier dynamics. The measurements revealed that early time highly mobile charges undergo fast non-geminate recombination at the contacts, causing an apparent field dependence of free charge generation in TDCF experiments if not conducted properly. On the other hand, recombination the later time scale was determined by dispersive recombination in the bulk of the active layer, showing the characteristics of carrier dynamics in an exponential density of state distribution. Importantly, the comparison with steady state recombination data suggested a very weak impact of non-thermalized carriers on the recombination properties of the solar cells under application relevant illumination conditions. Finally, temperature and field dependent studies of free charge generation were performed on three donor-acceptor combinations, with two donor polymers of the same material family blended with two different fullerene acceptor molecules. These particular material combinations were chosen to analyze the influence of the energetic and morphology of the blend on the efficiency of charge generation. To this end, activation energies for photocurrent generation were accurately determined for a wide range of excitation energies. The results prove that the formation of free charge is via thermalized charge transfer states and does not involve hot exciton splitting. Surprisingly, activation energies were of the order of thermal energy at room temperature. This led to the important conclusion that organic solar cells perform well not because of predominate high energy pathways but because the thermalized CT states are weakly bound. In addition, a model is introduced to interconnect the dissociation efficiency of the charge transfer state with its recombination observable with photoluminescence, which rules out a previously proposed two-pool model for free charge formation and recombination. Finally, based on the results, proposals for the further development of organic solar cells are formulated.

Zusammenfassung

Organische Halbleiter sind eine vielversprechende Materialklasse. Ihre besonderen Eigenschaften sind die gute Absorption, das geringe Gewicht und die einfache Verarbeitung zu dünnen Filmen. Daher wird intensiv an der Realisierung organischer Dünnschichtsolarzellen (OPVs) geforscht. Aufgrund der niedrigen Dielektrizitätskonstante organischer Halbleiter sind primäre Anregungen (Exzitonen) jedoch stark gebunden, und es muss ein Typ II-Heteroübergang eingeführt werden, um diese Anregungen in freie Ladungen zu trennen. Daher bestehen die meisten organischen Solarzellen aus mindestens einem Elektronendonator und einem Elektronenakzeptormaterial. Für solche Donator-Akzeptorsysteme sind hauptsächlich drei Zustände relevant; das Exziton auf dem Donator- oder Akzeptormaterial, der Ladungstransferzustand an der Donator-Akzeptor-Grenzfläche und der ladungsgetrennte Zustand eines freien Elektrons und Lochs. Das Zusammenspiel dieser Zustände bestimmt maßgeblich die Effizienz organischer Solarzellen. Aufgrund der hohen Absorption und der geringen Ladungsträgermobilitäten sind die aktiven Schichten dünn, aber auch die Exzitonendissoziation und die Bildung freier Ladung findet auf kurzen Zeitskalen statt, was die Analyse der Ladungsträgerdynamik erschwert. Im Mittelpunkt dieser Arbeit standen daher zunächst die Installation neuer Versuchsaufbauten zur Untersuchung der Ladungsträgerdynamik in optimierten Solarzellen mit überlegener Empfindlichkeit und Zeitauflösung sowie die Anwendung dieser Methoden auf prototypische photovoltaische Materialien. Im Hinblick auf das erste Ziel wurde ein neuer Aufbau, der optische Methoden wie die zeitaufgelöste Absorptionsspektroskopie (TAS) mit optolektronischen Methoden, wie die zeitaufgelöste Ladungsextraktion (TDCF) kombiniert. Ein wichtiger Teil dieser Arbeit war die Verbesserung der elektronischen Komponenten hinsichtlich der Zeitauflösung und Empfindlichkeit. Zu diesem Zweck wurde ein hochempfindlicher Verstärker zur Ansteuerung und Detektion der Probenantwort in TDCF entwickelt. Dieser Versuchsaufbau wurde im Folgenden auf verschiedene Modellsysteme angewendet, mit besonderem Fokus auf dem Verständnis der Verlustmechanismen, die den Füllfaktor und den Kurzschlussstrom organischer Solarzellen limittieren. Das erste Modellsystem ist ein hybrides Material, das aus anorganischen Quantenpunkten mit organischen Liganden besteht. Messungen mit TDCF ergaben eine schnelle Rekombination freier Ladungsträger, die teilweise

durch Fallen unterstützt wurde, während Ladungsextraktionsexperimente unter quasi-konstanter Beleuchtung eine hohe Mobilität zeigten. Mit den gemessenen Parametern konnte die Kennlinie gut mit einem analytischen Modell beschrieben werden. Mit einer weiteren Verbesserung des Aufbaus konnte ein zweites Thema, die detaillierte Analyse der nicht-geminalen Rekombination in einer ungeordneten Polymer-Fulleren-Mischung bearbeitet werden. Die Messungen zeigten, dass hochmobilen Ladungen zu frühen Zeiten eine schnelle, nicht-geminale Rekombination an den Kontakten durchlaufen, was eine scheinbare Feldabhängigkeit der Generierung freier Ladung in TDCF-Experimenten verursachen kann. Andererseits wurde die Rekombination auf längeren Zeitskalen durch dispersive Rekombination in der aktiven Schicht bestimmt, wobei die Ursache der Ladungsträgerdynamik in einer exponentiellen Verteilung der Zustandsdichte liegt. Der Vergleich mit Rekombinationsdaten im stationären Zustand ergab einen sehr schwachen Einfluss nicht-thermalisierter Ladungsträger auf die Rekombinationseigenschaften der Solarzellen unter anwendungsrelevanten Bedingungen. Schließlich wurden temperatur- und feldabhängige Studien zur Erzeugung freier Ladung an drei Donator-Akzeptor-Kombinationen durchgeführt, wobei zwei Donatorpolymere der gleichen Materialfamilie mit zwei verschiedenen Fulleren-Akzeptormolekülen gemischt wurden. Diese besonderen Materialkombinationen wurden ausgewählt, um den Einfluss der Energetik und Morphologie der Mischung auf die Effizienz der Ladungserzeugung zu analysieren. Zu diesem Zweck wurden die Aktivierungsenergien für die Photostromerzeugung für einen weiten Bereich von Anregungsenergien genau bestimmt. Die Ergebnisse beweisen, dass die Bildung freier Ladungen über thermalisierte Ladungstransferzustände erfolgt und keine Aufspaltung mit heißen Exzitonen beinhaltet. Überraschenderweise sind die Aktivierungsenergien vergleichbar mit der thermischen Energie bei Raumtemperatur. Dies führte zu der wichtigen Schlussfolgerung, dass organische Solarzellen nicht aufgrund von hochenergetischen Pfaden gut funktionieren, sondern weil die thermalisierten Ladungstransferzustände schwach gebunden sind. Darüber hinaus wird ein Modell eingeführt, um die Dissoziationseffizienz des Ladungstransferzustands mit seiner mit Photolumineszenz beobachtbaren Rekombination zu verbinden, wodurch ein zuvor vorgeschlagenes Zwei-Pool-Modell für die Bildung und Rekombination von freien Ladungen ausgeschlossen wird. Abschließend werden auf Basis der Ergebnisse Vorschläge zur Weiterentwicklung organischer Solarzellen formuliert.

Contents

1. Introduction **1**

1.1. Organic Solar Cells 2
1.2. Debates about the dominant pathway of free charge formation . . . 5
1.3. Experimental Methods to Probe Transient Photovoltaic Processes in Organic Solar Cells 11
1.4. Scope of the Work 14

2. Fundamental Part **16**

2.1. Efficiency of Organic Solar Cells 16
2.2. Charge Generation and Geminate Recombination 21
2.3. Involved States and Energetics 22
2.3.1. Onsager Model 24
2.3.2. Onsager-Braun Model 25
2.3.3. Two Pool Models 28
2.3.4. Interface Energetics 31
2.4. Charge Extraction and Nongeminate Recombination 32
2.4.1. Charge Extraction 32
2.4.2. Non-geminate Recombination 35

3. Experimental Part **40**

3.1. Organic Photovoltaic Devices 40
3.2. Methods 41
3.3. Time Delayed Collection Field Experiments 46
3.4. Home-Built Amplifier 47
3.5. Field dependent Transient Absorption Spectroscopy 53
3.6. Bias Assisted Charge Extraction 57

4. Free Carrier Generation and Recombination in PbS Quantum Dot Solar Cells **58**

5. Dispersive Non-Geminate Recombination in an Amorphous Polymer:Fullerene Blend **69**

6. Probing the Pathways of Free Charge Generation in Organic Bulk Heterojunction Solar Cells **86**

7. Conclusion and Outlock **104**

Bibliography **109**

A. Appendix **i**

A.1. Organic Solar Cell Characterization and Evaluation i

A.1.1. Electroluminescence i

A.1.2. External Quantum Efficiency i

A.1.3. Current Voltage Characteristics ii

A.1.4. Rate Equation Solver - Source Code iii

A.1.5. Drift Diffusion Simulation - Source Code ix

A.1.6. Temperature-dependent time resolved Photoluminescence . . xiii

A.1.7. Temperature dependent TDCF Experiments xiii

A.2. Fluence dependent Charge Generation in MEH-PPV:PCBM blends xiii

B. Publications **xvi**

B.1. Author Contribution xviii

C. Conference Contributions **xix**

D. Acknowledgment **xx**

E. Thesis Declaration **xxi**

Chapter 1

Introduction

Solar cells convert sun energy directly into electrical power. Today, all commercial solar cells use inorganic semiconductors, *e.g.* silicon reaching power conversion efficiencies of up to 26.1% [1]. Manufacturing of crystalline inorganic photovoltaic devices requires crystal growing and elevated temperatures rendering the production costs intensive.

Organic semiconductors are an attractive alternative to their inorganic counterparts due to their easy processing and high absorption coefficients. In fact, organic solar cells (OPV) made from polymers or small molecules as donor materials blended with fullerene have shown tremendous increase in the power conversion efficiency (PCE) over the past decade of up to 12.1% [2] with the potential of future optimization. Tandem solar cells with subcells made of fully solution processed polymer-fullerene and polymer-non-fullerene acceptor solar cells have shown power conversion efficiencies of up to 17.3% [3]. This thin film technology benefits from solution processing, markedly reducing production costs. The OPV modules are flexible, light weight, semitransparent and can be of any color. Early OPV devices were very poor in their power conversion efficiency reaching only one percent [4] but a relatively high fill factor of 65% demonstrated the potential of OPV devices. In the following decades the PCE constantly increased, but yet not reaching the state of inorganic semiconductor devices. These limitations are strongly linked to free charge formation upon illumination, loss of charges and charge transport.

This motivated the main goal of this thesis, namely to improve the fundamental understanding of free charge formation, recombination and extraction in organic solar cells with regard to the energetic and morphologic landscape, the electric field and temperature.

1.1. Organic Solar Cells

All efficient organic photovoltaic systems are based on a combination of electron donors (D) blended with acceptors (A). In DA-systems, mostly soluble fullerene derivatives are combined with conjugated donor polymers and deposited from a common solvent. Due to the low entropy of mixing and the large molecular weight these DA-systems self-assemble during the drying procedure into a micro-phase-structure. Thereby an interface grows throughout the whole bulk, which is called bulk heterojunction (BHJ) and can be actively controlled by using different solvents, solvent additives or small changes to the donor polymer or acceptor fullerene side chains. Up to now DA-systems with fullerene derivatives based on C_{70} as the acceptor show efficiencies of nearly 11% [5], although blends with non-fullerene-acceptors reach 14% [6, 7].

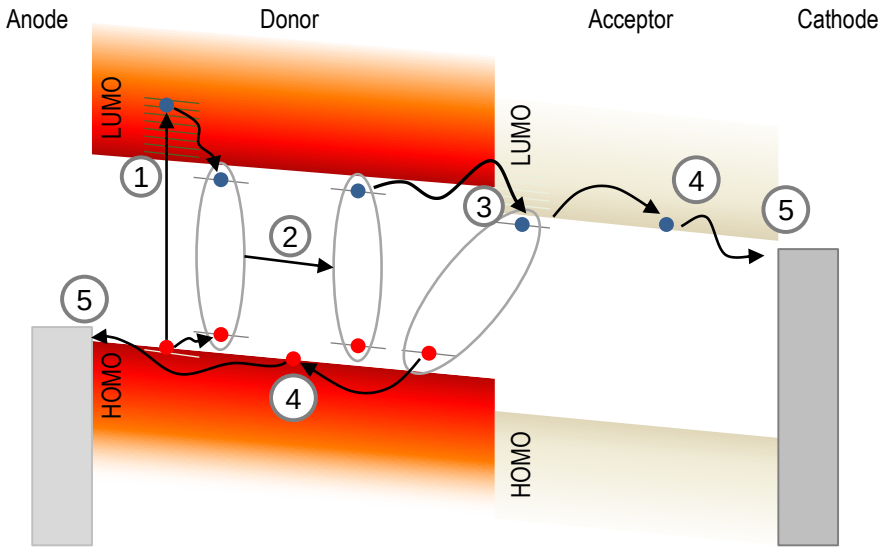

Figure 1.1.: Simplified energy diagram sceme of a DA interface: (1) if the donor material has absorbed a photon with a larger energy than the optical bandgap an electron is excited from the ground state to a electronically and vibronically excited state, an coulombically bound exciton is formed. (2) This exciton will diffuse via random walk to the DA interface, where the electron transfers to the acceptor (3) or it geminately recombines. The transferred electron forms together with the remaining hole on the donor, a CT-state which is still coulombically bound and therefore lower in energy than the (4) charge separated (CS) state. The energy of the CS-state is defined by the D_{HOMO} and A_{LUMO} difference. The separated charges are travelling through the bulk and can possibly recombine non-geminately. Free charges were extracted at the electrodes (5).

Figure 1.1 sketches all steps involved from excitation (1) to charge extraction (5) in a BHJ solar cell. Due to the low dielectric constant of organics the initially photogenerated species is a Frenkel exciton (1) with a binding energy of several hundreds of millielectronvolts. When compared to inorganic semiconductors, which have a much higher dielectric constant, this binding energy is much stronger in organics, which dictates that splitting of the exciton requires a DA interface.

Most of the high performance materials for organic solar cells have a very strong absorption already at layer thicknesses of approximately 200 nm and convert nearly every absorbed photon into an Frenkel exciton. Thus their internal quantum efficiency of the first step is close to 100% [8]. This means, that usually the first step of generating Frenkel excitons is not limiting. The critical step is that these excitons need to find an interface within their lifetime in order to be separated. Therefore a well designed BHJ morphology is helpful. Besides morphology, an important driving force for exciton splitting is the donor-LUMO, acceptor-LUMO offset which is believed to be responsible for stabilizing CT states with respect to the excited singlet state off the donor or acceptor. The role of the driving force and its importance for device performance will be discussed in chapter 6. These Frenkel excitons are neutrally charged, therefore an external field does not move the exciton, it has to diffuse to the nearest interface (2). Here, the previously mentioned BHJ plays a critical role; if the micro-phases are too large, the exciton will probably geminately recombine. If the micro-phases are too small, the exciton is split efficiently, but the CT state (3) may not be able to split into free carriers and will also recombine geminately.

CT-excitons (3) can recombine geminately, or split into free charges (4). If free charges, generated at spatially different sites in the donor and acceptor domain, form CT states and recombine before they can be extracted, this recombination process is called non-geminate and will be discussed in more detail in section 2.4, chapter 4 and chapter 5. Here, the BHJ micro structure again plays a critical role, *e.g.* small micro-phases probably lead to increased non-geminate recombination.

The overall performance of the solar cell is influenced by all of the mentioned steps; from the efficiency of exciton harvesting (1) and of CT-state splitting, to the transport (4) and extraction (5) of free charges to the electrodes. These steps relevant for charge carrier generation in such two-component systems involves a variety of processes on different time and length scales. Figure 1.2 adds the relevant time scale to the fundamental functioning shown in Figure 1.1.

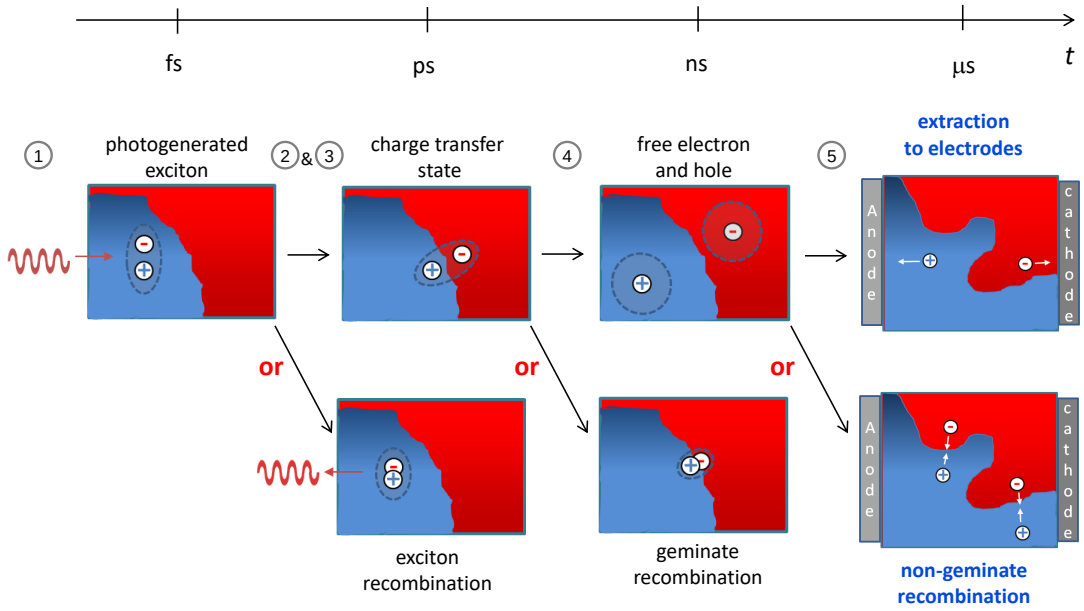

Figure 1.2.: Timeline on which charge generation and recombination takes place: An exciton is generated after photon absorption (1) in the femtosecond (fs) range and diffuses to an interface (2) where it splits up into a charge transfer (CT) state (3) or recombines radiatively in the picosecond (ps) range. The CT-state splits up into free charges (4) or recombines geminately within roughly one nanosecond, whereas free charges can be extracted to the electrodes (5) or recombine non-geminately in the ns to µs range. Figure partially adopted with permission from Ref. [9].

Primary photoexcitations in the photoactive blends are strongly bound singlet Frenkel excitons on either of the two semiconductors. These excitons dissociate at the donor-acceptor interface (step (2) and (3) in Figure 1.2) to form interfacial charge transfer states or recombine on ultrafast time scales. These intermolecular excitations will eventually split into free charges (step (4) in Figure 1.2) or undergo geminate recombination in the nanosecond range. Finally, charges are extracted to the electrodes in the ns to μs range (step (5) in Figure 1.2).

Because the low dielectric constant ϵ_r of organic semiconductors, typically close to 3.5 [10], electron-hole pairs in intramolecular excitons and intermolecular CT excitations will experience strong Coulombic binding - in apparent contradiction to the efficient and field-independent free charge generation of several state-of-the-art DA blends. This discrepancy triggered an intensive discussion regarding the pathway of absorbed photon-to-electron conversion (see Figure 1.3) and, in particular, the nature and energetics of the CT states primarily involved in free

carrier formation [11–14].

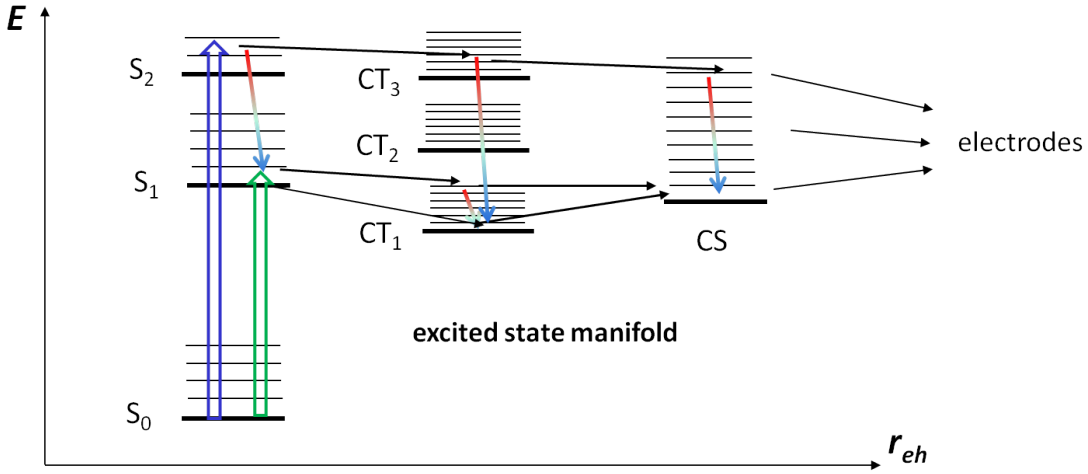

Figure 1.3.: Involved states and possible thermalization processes; The singlet state can be excited with a high photon energy (blue) or not (green), the electron is then transfered to an electronically excited CT-level (upper arrow) or if the exciton has already thermalized, the CT-state could be still vibronically excited (lowest arrow) and split up into free charges before thermalizing. The weakly bound CT-exciton is separated into free charges, referred to as CS. Both upper arrows describe the 'hot' exciton dissociation, the lower arrows the opposite. In every step, thermalization is favorable (coloured arrows).

The following section shed light on the debates in literature about whether the high energy or the low energy pathway as introduced in Figure 1.3 leads to free charge formation.

1.2. Debates about the dominant pathway of free charge formation

In general, thermalization of excitons and charges can proceed in two different ways. The first process is the on-site loss of extra excitation energy via emission of phonons. For example, singlet and triplet excitons loose their electronic and vibronic energy via internal conversion and vibrational relaxation, and the same process thermalizes CT states and excited charges. The second process is the loss of energy in an energetically disordered system by hopping to sites with lower energies. Both pathways are functional in organic semiconductors and will compete with (and suppress and assist) the dissociation of excitons, the separation of CT

states and the extraction of free carriers. It has been proposed that the extra excitation energy of the singlet exciton is partially converted into vibronic excitations of the interfacial CT states and that this excess energy assists in the split-up of the CT states into free carriers, thereby overcoming the Coulomb binding energy [15–21]. This suggests that CT exciton dissociation benefits from generation of 'hot' CT states and that these states are the predominant precursors to free charges. Transient absorption spectroscopy (TAS) was used to demonstrate that high energy excitons in the polymer preferably form excited CT-states, which split into free charge carriers within the instrument response time of one hundred femtoseconds, which corresponds to a charge generation pathway *via* an excited CT-manifold, meaning that only CT_1 is recombining (see Figure 1.3 and Figure 1.4 a, low energy CTS). For example, Grancini *et al.* proposed that higher energy excitations generate free charges even faster *via* S_4 and CT_3 or CT_4 [18] (see Figure 1.4, a). The strong coupling of the excited singlet excitons and 'hot' CT states was convincingly confirmed by theoretical calculations of, for example, Troisi *et al.* demonstrating a delocalization of the holes in the excited CT states [21]. Free charge formation via excited CT-states is also expected to occur in polymer:fullerene solar cells under application-relevant conditions.

A direct correlation between the short circuit current and the driving force for charge separation[1] was observed by Shoaee *et al.* [20]. An advantageous effect of a hot CT-exciton for the generation of free charges is also reported by measuring increased internal quantum efficiencies (IQEs) with higher photon energies [16, 22], but these results have been highly discussed in subsequent publications given the difficulty of measuring absolute IQEs [26, 27].

On the other hand, several groups have suggested that free charge formation involves thermalized CT states [26, 28–30]. Most of these studies utilized the fact that CT states can be populated directly through sub-bandgap excitation (see Figure 2.3, gray and red arrows). For example, the work by Vandewal *et al.* shown in Figure 1.5 b revealed very similar shapes of the absorption spectra and of the external quantum efficiency for free charge formation, indicating that the internal quantum efficiency does not depend on whether the primary excitation is a CT state or an exciton [28, 31]. The internal quantum efficiency was shown to be constant within a broad range in energy, but to determine the IQE many assumptions

[1] The driving force for charge separation is the difference in energy between the initial vibronically relaxed singlet S_1 state and the free charge pair [24, 25].

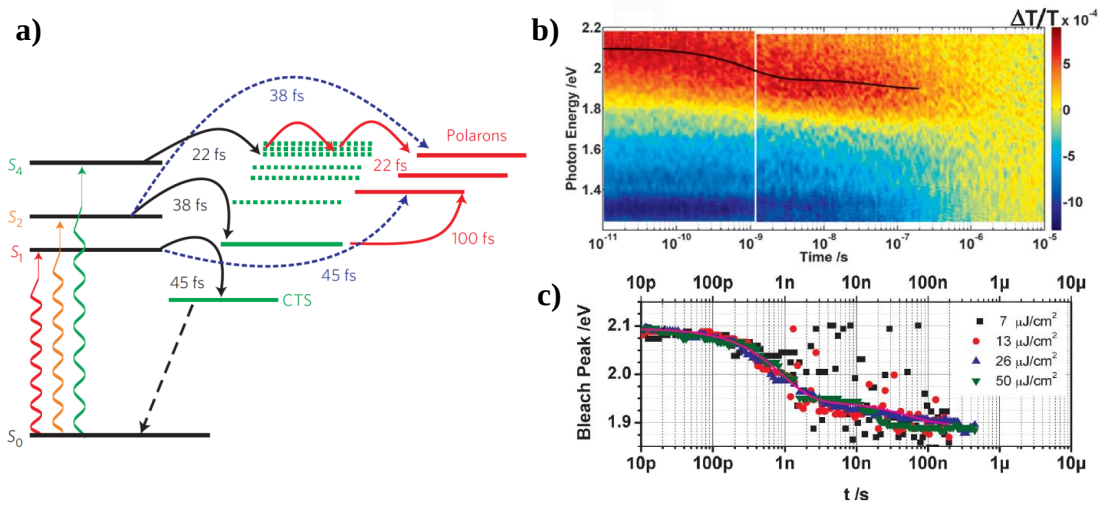

Figure 1.4.: Ultrafast spectroscopy on polymer:fullerene solar cells: (a) Proposed mechanism and states involved in charge generation for a PCPDTBT:PCBM device: singlet exciton states (represented by the black lines), interfacial CT states (green-coloured levels) and free polarons (red-coloured levels). The solid black arrows represent exciton dissociation into the CT state manifold; blue dashed arrows indicate exciton quenching into free polarons and solid red arrows represent CT state dissociation into free polarons with time scales for each process. Note, that in this picture the relaxed CT state manifold is prone to recombine geminately without being connected to the CS state at all. Reprinted with permission from Grancini *et al.*[22].(b) transient absorption false color map for a PCDTBT:PCBM device measured in transmission, the black line is a guide to the eye showing the relaxation in energy of the absorption bleach peak with time for (c) different fluencies. Reprinted with permission from Howard *et al.*[23].

are made under which a statement about the pathways of free charge generation can not be finally made.

A more direct measurement of free charge generation was investigated with time-delayed-collection-field experiments (TDCF, introduced in the following section) as a function of electric field and excitation energy for different BHJ blends (see Figure 1.6). None of these cases revealed an appreciable effect of the excess energy on the field-dependence of charge generation, thereby supporting the view that charge generation proceeds through thermalized CT states [26, 28]. But whether the field dependence of free charge formation is an adequate measurement of the activation of charge generation is controversial. A discussion in chapter 6 will contribute to this debate with an accurate measurement of the activation energy, which is expected to be temperature dependent.

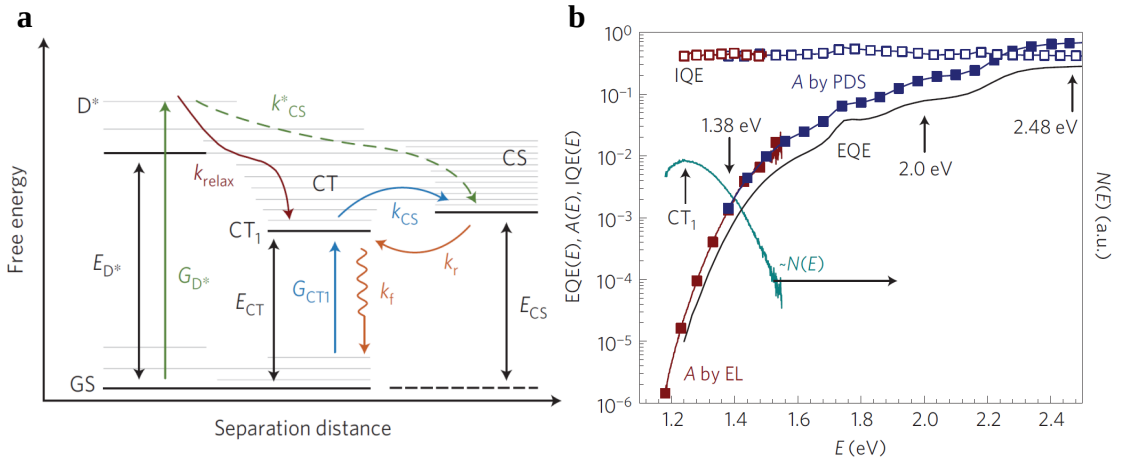

Figure 1.5.: (a) The absorption of a photon with energy greater than the donor bandgap generates an exciton in the donor D* at the rate G_{D}*. The formation of the charge separated state (CS) can follow several paths: a path at the rate k_{CS}* leads via vibronic (and electronically) excited CT states and bypasses the relaxed state CT_0. Alternatively, the system relaxes to CT_0 (rate k_{relax}). This state can relax with the rate k_f to the ground state (GS) or split into free charges (k_{CS}). The inverse process to k_{CS} is the population of CT_0 from CS at the rate k_{r}. E_D*, E_{CT} and E_{CS} denote the energies of the vibronic (and electronically) relaxed states of the donor exciton, the CT state and the charge-separated state, respectively. Picture adopted with permission from [28]. (b) IQE(E) in the energy range of CT emission for polymer:fullerene organic solar cells [28]. External quantum efficiency (EQE, black line), electroluminescence (EL) emission spectra N(E) (cyan line) and the high energy part of the A(E) spectra (blue line filled squares). In the very weakly absorbing region, the A(E) spectra are reconstructed using N(E) as described in [28] and are overlaid to the A(E) spectra from photothermal deflection spectroscopy in the overlapping region (red line, filled squares). The IQE(E) spectra (open squares) of the devices are calculated as EQE(E) / A(E). Picture adopted with permission from [28].

Most organic materials are disordered and only a few compounds form crystallites throughout the entire layer thickness [32]. As pointed out above, excitations and charges can loose energy by hopping to lower energy sites. The consequence of this are dispersive effects, with a pronounced time dependence of the relevant properties. Typical examples of time dependent properties are spectral diffusion of excitons [33–35] or time-dependent charge carrier mobilities [36–39]. In accordance with this picture, recent studies on prototypical polymer:fullerene blend devices revealed significant thermalization effects [39–44]. One example is PCDTBT blended with PCBM. In contrast to neat polymer layers, the PCDTBT:PCBM blend is nearly amorphous [45], independent of device thickness [46]. As shown in

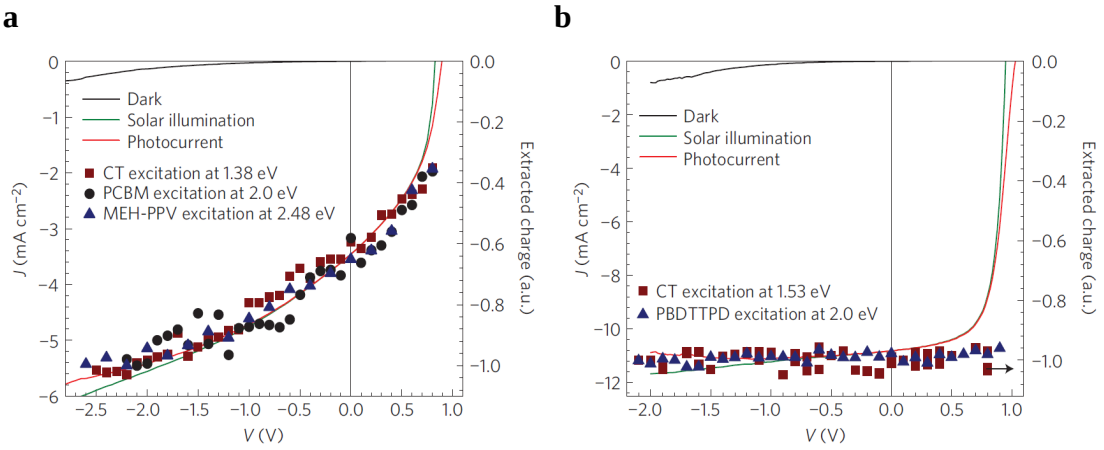

Figure 1.6.: Photocurrent density versus charge as a function of applied Bias: J–V curve (left axis) and charge (right axis) for a MEH-PPV:PCBM device (a) and for a PBDTTPD:PCBM device (b). Excitations of D*, A* and the CT state (at 1.38 eV for (a) and 1.5 eV for (b)). Reprinted with permission from Vandewal *et al.*[28].

Figure 1.4 b, transient absorption spectroscopy by Howard and coworkers revealed a progressive red-shift with time of the photoinduced absorption feature assigned to polarons on the polymer, which was attributed to the thermalization of holes [23]. The large shift of the TAS signal (of nearly 0.2 eV, see Figure 1.4 c) and the long thermalization time (up to 100 ns) was seen as an indication of considerable energetic disorder of the polymer HOMO in the amorphous blend. As a consequence, charge carrier mobilities were proposed to be time-dependent, with a more pronounced mobility decay of holes due to larger disorder in the HOMO as shown in Figure 1.7 a. It was concluded that polarons are extracted and may recombine while still thermalizing [23, 39].

Evidence for carrier relaxation at time scales above one microsecond came from Monte-Carlo-Simulations taking disorder into account [47]. Scheidler *et al.* proposed a time dependence of the recombination rate following a power law $\mathrm{d}n/\mathrm{d}t \propto t^{-1}$ upon increasing σ, while for decreasing σ, $\mathrm{d}n/\mathrm{d}t \propto t^{-2}$ is recovered at long times. The bimolecular recombination coefficient $(\mathrm{d}n/\mathrm{d}t)/n^2(t)$ shown in Figure 1.7 b decreases with time and does not approach a constant value at longer times for a large energetic disorder [47].

Time of flight (TOF) measurements suggested higher order recombination with a possible time dependent recombination coefficient [48]. The TOF experiments were performed as a function of circuit resistance, with 50 Ω, 1 kΩ and 10 kΩ.

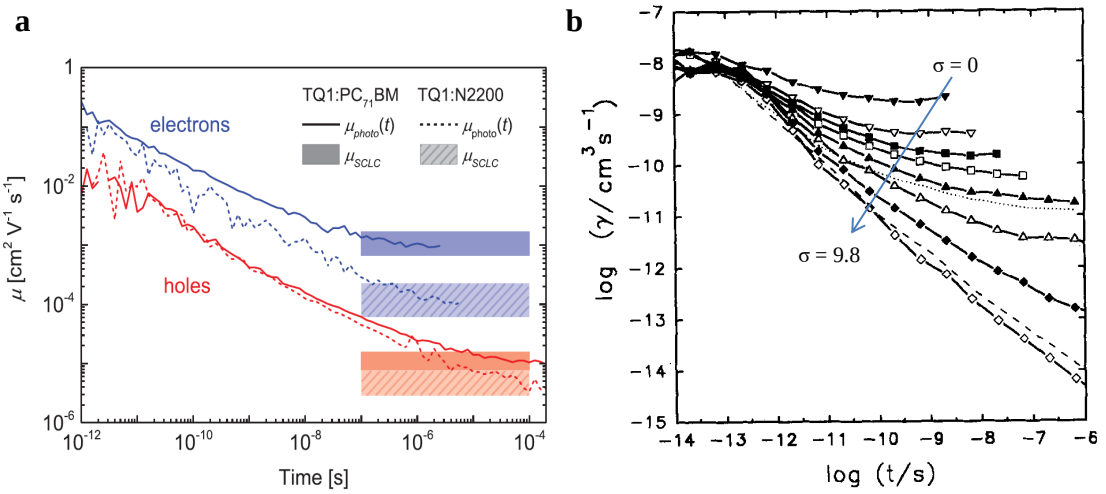

Figure 1.7.: Monte-Carlo-Simulation of the Time dependence of Mobility and the Recombination Coefficient. (a) Simulated time-dependent photogenerated carrier mobility $\mu_{photo}(t)$ for TQ1:PC_{71}BM (solid lines) and TQ1:N2200 (dashed lines). Blue corresponds to electrons; red to holes. Shaded areas indicate the estimated SCLC mobility μ_{SCLC} for TQ1:PC_{71}BM (solid fill) and TQ1:N2200 (patterned fill). Reprinted with permission from Melianas *et al.* [44]. (b) Simulated bimolecular rate constant as a function of time for different energetic disorder parameters σ ranging from 0 to 9.8. Reprinted with permission from Scheidler *et al.* [47].

The effect of altering the resistance is that charge extraction from the device takes longer with larger resistances. The bimolecular recombination coefficient was then calculated for every extraction time showing a power law decay at longer times [48]. Time dependent mobilities and recombination coefficients may be relevant for the performance of the device. For example, the performance may suffer from accelerated recombination, or improve by faster extraction at early times. Therefore, an important question is whether charges in an organic solar cell are mostly thermalized or still hot when they get extracted or recombine.

1.3. Experimental Methods to Probe Transient Photovoltaic Processes in Organic Solar Cells

The different processes involved in the photocurrent generation in organic solar cells introduced in the previous section run at different time scales, from femtoseconds to many microseconds (see also Figure 1.2). Time resolved measurements do not necessarily reproduce the steady-state conditions, for example because they are conducted at only short time scales and at much higher light intensities. Up to now mainly transient absorption spectroscopy (TAS), time delayed collection field (TDCF), time of flight (TOF) and time resolved electric field induced second harmonic generation (TREFISH) have been used to probe the pathways of charge generation and charge carrier dynamics. In the following section the methods are briefly introduced and their specific advantages and shortcomings are highlighted.

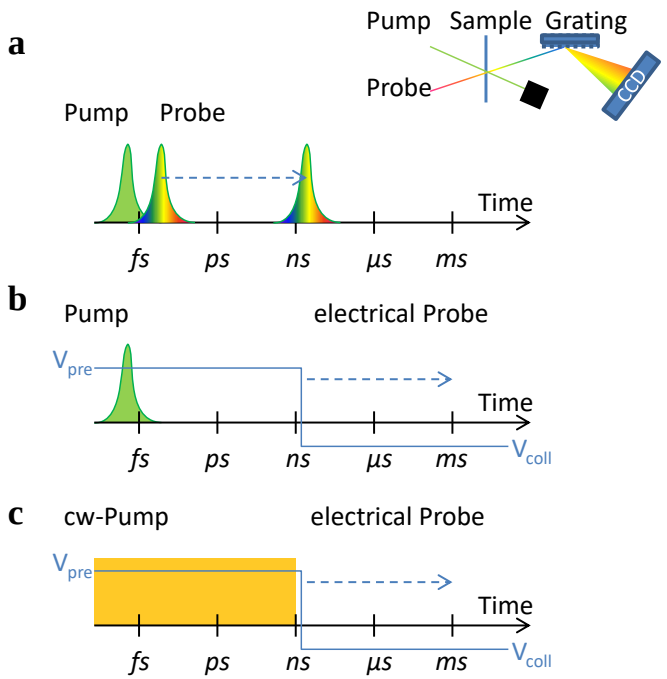

Figure 1.8.: Experimental methods: (a) transient absorption spectroscopy (TAS) with optical pump pulse (green) and white light probe pulse (colored), (b) time delayed collection field (TDCF) with optical pump pulse applied when the device is held at a certain pre-bias V_{pre} and electrical probe pulse at reverse bias V_{coll}, (c) bias assisted charge extraction (BACE) with constant illumination to have the device in quasi-equilibrium at a certain pre-bias. The illumination is switched off at the same time as the collection voltage is applied.

Ultrafast measurement techniques were made possible with the so called *chirped pulsed amplification* of ultrashort laser pulses introduced 1985 by Novel prize winner 2018 Donna Strickland [49]. First applications with the new pulsed light source in a pump-probe experiment investigating organic materials were published by Kraabel and coworkers [50]. Ultrafast transient absorption spectroscopy is an all-optical pump probe method, where a pulsed laser is used to excite electrons in the active material from their ground states to higher-energy excited states (Figure 1.8 a, green). An ultrashort white light probe pulse is used to measure the transmission through a sample at various delayed times following its excitation with a pump pulse, and to compare it to the transmission without the pump pulse (Figure 1.8 a, colored) [51]. After passing through the sample, the unabsorbed light from the white light pulse continues to a grating for spectral decomposition and a CCD array (Figure 1.8 a, inset). This allows for probing of the decay kinetics of the excited states. TAS has a great time resolution ranging from the fs- to the μs-range, depending only on the pulse width, but the difficulty lies in the seperation and analysis of the manifold of spectral features. In particular, for most organic systems, the spectral features of free charges and of charges bound in CT states are very similar and measurements over our wide fluence range are usually needed to differentiate between these two species. Also, because of the low resolution of optical detection, most TAS measurements were performed at rather high fluences, generating carrier densities well above the steady state density at application-relevant conditions. Finally, very few people applied TAS to full devices [52–54]. The reason lies in the difficulty of conducting TAS experiments well below application relevant conditions [55] to finally resolve the influence of the externally applied electric field. Additionally, if extraction is measured with TAS, the same RC-limitations are valid as for TDCF. In the setup presented in this work, TAS measurements on fully optimized organic solar cells were made possible.

The invention of time delayed collection field experiments goes back to Langevin[2], who studied the recombination of gas ions [56, 59]. Later TDCF was also applied to inorganic [57] and organic solar cells [29, 58, 60, 61]. But previous TDCF experiments suffered from a poor time and photocurrent resolution. Notable improvements to the TDCF setup will be highlighted in section 3.3. For TDCF the working device stack is held at a certain pre-bias V_{pre} during illumination with a short laser pulse (Figure 1.8 b, green). After a variable delay the remaining charge

[2]Langevin wrote his phd thesis in french, here *champ de collecte retardé* [56] is meaningfully translated into *time delayed collection field* [57, 58].

is extracted with a large reverse bias, the collection bias V_{coll} (Figure 1.8 b, blue line). TDCF is applied to a working device stack and therefore directly measures free extractable charge of a fully optimized solar cell.

Time of flight (TOF) is a powerful method to measure charge carrier mobilities in inorganic or organic materials [62, 63]. The sample needs to be very thick in comparison to a fully optimized organic solar cell, on the order of micrometers, in order to obtain reasonable mobilities. Once a short laserpulse hits the sample from the side of the transparent electrode, free charges are photogenerated in a thin layer which drifts within the externally applied electric field through the material thereby inducing a constant current which drops when the charge reaches the counter electrode. The drop in the photocurrent is the transit time t_{tr}. The drift velocity v_d and mobility μ can be calculated with $v_d = d(t_{tr})^{-1} = \mu F$, with F being the electric field and d the active layer thickness. Integration of the TOF-transient leads to the average charge density in the device. The time resolution regarding the obtained charge carrier density is limited to the μs-range, rendering conclusions about charge formation difficult to trust (see also Figure 1.2). TOF measurements were recently conducted with our new TDCF setup [64]. TDCF is also able to measure mobilities in a fully optimized device, but cannot distinguish between electron and hole mobility.

Time resolved electric field induced second harmonic generation (TREFISH) is an optical pump probe method on a device with electrodes and an externally applied electric field [65]. Excitation leads to a shift of the charge centers and induces a polarization. Due to the time-dependent change of the exciting electric field, the dipole moment oscillates with the frequency of the excitation. If its amplitude is small, the dipoles emit photons of the same frequency as the excitation (harmonic oscillation). If the amplitude is large, the vibration becomes anharmonic and the emitted photons has double the frequency of the excitation. This phenomena is called second harmonic generation (SHG). In organic materials, however, SHG is usually not observed due to the prevailing symmetries. This symmetry can be broken by the application of an external or internal electric field. The setup is comparable to TAS but must ensure the correct polarization of the pump and probe (p-polarization) and that the pump does not interfere with the probe or the SHG signal. TREFISH has a great time resolution (fs- to ns-range) but suffers from the same limitations like TAS [39]. This method needs very high fluence to generate SHG which degenerates most organic compounds. TREFISH was set up

in course of the phd but results are not presented in this thesis.

The methods presented here, as well as many other methods were used to investigate the pathways of free charge generation. Steady state methods, such as *e.g.* external quantum efficiency in combination with electroluminescence experiments, often led to the conclusion that the generation of free charges proceeds via low-energy pathways [14, 31, 66]. Also first TDCF experiments with direct excitation of the CT state supported a charge generation pathway via relaxed CT states [26, 28, 29, 67]. In contrast, time-resolved methods allowed for different conclusions. Strong support for the 'hot' charge generation pathway came mostly from ultrafast time resolved measurement techniques like TAS and TREFISH [18, 20, 44, 68–71]. The question now is which of the two points of view correctly describes the processes involved in free charge generation.

1.4. Scope of the Work

The scientific motivation of this work is based on the question whether the generation of free charges follows hot or cold pathways, as well as whether free charges thermalize within the density of states before they are extracted or recombined. Therefore, the first goal of the thesis, was to design and build up a setup that allows for TDCF, TAS, BACE and possibly TREFISH measurements on the same, fully optimized sample to cover a time scale from femtoseconds to milliseconds. In order to be able to carry out the mentioned experiments on the same sample, they have to be combined on the same optical table. Furthermore, previous TDCF setups suffered from poor time resolution, which had to be increased to access the important *n*s range. Previous TDCF setups additionally suffered from low signal to noise ratio, which also had to increase to further suppress non-geminate recombination by utilizing at least one order of magnitude lower fluences. To make this possible, a research proposal was submitted to the DFG and approved (INST 336/94-1 FUGG). In 2015, a new femtosecond laser laboratory at the University of Potsdam was inaugurated.

The highly improved and newly set up TDCF and BACE method was first tested on nanoparticle solar cells in chapter 4, because earlier experiments suggested, that the charge carrier dynamics is very fast [72]. After testing the new apparatus, we

employed time delayed collection field (TDCF) experiments to study the recombination of photogenerated charge in the high-performance polymer:fullerene blend PCDTBT:PCBM in chapter 5. Non-geminate recombination in the bulk of this amorphous blend is shown to be highly dispersive, with a continuous reduction of the recombination coefficient throughout the entire time scale, until all charge carriers have either been extracted or recombined. Rapid, contact-mediated recombination is identified as an additional loss channel, which, if not properly taken into account, would erroneously suggest a pronounced field dependence of charge generation. Especially the last finding strongly supports the strength of our new TDCF setup. A final objective of this work is to measure the efficiency of free charge formation as a function of various parameters by direct excitation of low-energy CT states. These experiments will be performed on low bandgap polymer:fullerene blends with variable energetics (tunable position of the lowest unoccupied molecular orbital (LUMO) of the donor or electron affinity of the acceptor). A field dependent generation measured with TDCF for these polymer:fullerene blends was already published [26, 73–75], but was not investigated with TAS. First results with field dependent TAS measurements are presented in chapter 6). Having proved the field dependence of charge generation with TAS, TDCF experiments were conducted as a function of electric field and temperature. Here, it was investigated, whether the field dependence of the generation observed in many systems is the expression of a thermally activated splitting of bound CT states. Or second, whether it is essentially determined by the excess energy. By TDCF measurements with variation of the excitation wavelength, it is also investigated whether the statement made by experiments at room temperature that the generation of free charges occurs almost exclusively via the splitting of thermalized CT states [26, 28] is also valid at lower thermal energies (see chapter 6). The results obtained during this work are of fundamental importance for the understanding of free charge carrier generation and recombination in polymer:fullerene solar cells and thus point the way for further improvement of the efficiency.

Chapter 2

Fundamental Part

2.1. Efficiency of Organic Solar Cells

For any solar cell only those photogenerated charges which are extractable to the electrodes contribute to the efficiency. In this limit the external quantum efficiency (EQE) of photogeneration is written as a product of the fraction A of incident photons being absorbed in the active material, the probability f that exciton dissociation populates the connected CT manifold, the efficiency η_{diss} of free charge formation from these states and the efficiency η_{coll} that these free charge carriers reach the electrodes:

$$EQE(E(\lambda), F, T) = A \cdot f \cdot \eta_{diss} \cdot \eta_{coll}. \tag{2.1}$$

The product of the four efficiencies indicates the ratio of extracted charge carriers to incident photons. Generally, all four terms may be a function of the excitation energy $E(\lambda)$ the electric field F and temperature T. Investigation of these dependencies is one main task of this work.

Fundamentally, several limitations on energy conversion in solar cells are not preventable. Typically, a solar cell is characterized by its current-voltage (JV) curve under illumination where the maximum power is delivered at the maximum power point (MPP). The largest rectangle fitting under the JV curve (red rectangle in Figure 2.1a) defines the MPP and its corresponding voltage (V_{mp}) and current (J_{mp}). The fill factor (FF) is then defined by the ratio of the red rectangle with respect to the black rectangle (with V_{OC} and J_{SC}, see Figure 2.1a) $FF = J_{mp}V_{mp}(J_{SC}V_{OC})^{-1}$.

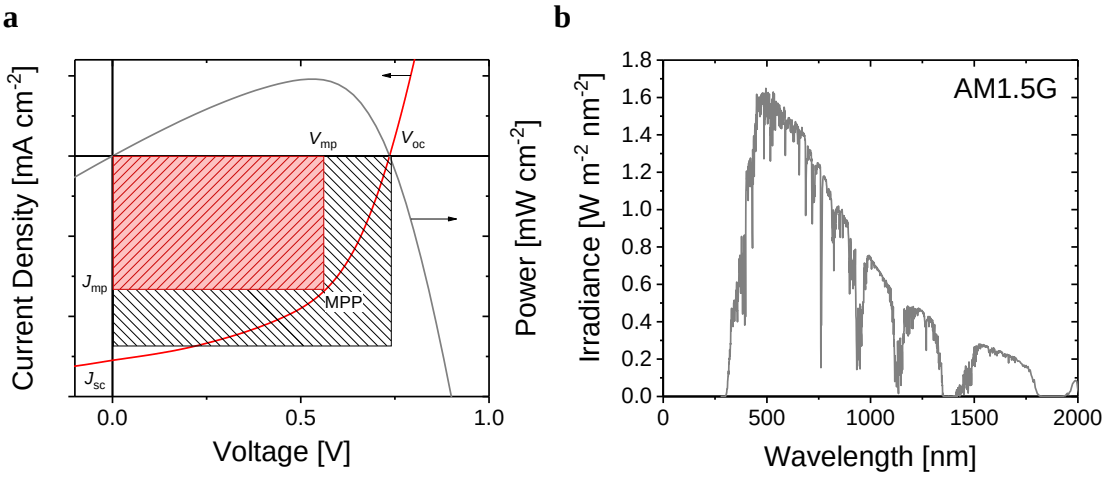

Figure 2.1.: Current Voltage Curve and sun spectrum (a) Exemplary JV curve (red line) of a solar cell with the basic parameters: maximum power point (MPP), open circuit voltage (V_{OC}), maximum power point voltage (V_{mp}), short circuit current (J_{SC}) and maximum power point current (J_{mp}). (b) AM1.5G hemispherical tilted 100 mW cm^{-2} sun spectrum.

To find the maximum power point it is helpful to also plot the power density (Figure 2.1a, grey line) and calculate the point at which the derivative is zero:

$$d(JV) = dJV + JdV = 0, \tag{2.2}$$

at the maximum power point:

$$\left(\frac{dJ}{dV}\right)_{mp} = \left(\frac{J}{V}\right)_{mp}. \tag{2.3}$$

To describe the JV curve, the Shockley equation is often used by researchers [76, 77]:

$$J = J_{rec} - J_G = J_0 \left(\exp\left(\frac{qV_{ext}}{n_{id}k_BT} - 1\right)\right) - J_G. \tag{2.4}$$

Here, J_{rec}, the recombination current and J_G, the generation current are equal at V_{OC}, q is the elementary charge, V_{ext} the externally applied voltage, n_{id} the ideality factor, k_B the Boltzmann constant and T the temperature. This equation was shown to successfully describe high fill factor solar cells *e.g.* crystalline silicon, but

is inappropriate for low mobility organic solar cells. A low mobility will severely limit charge extraction and with that reduce the internal voltage with respect to the externally applied bias. Recently, our modified Shockley equation was introduced by Neher *et al.*, which takes proper account of the low mobilities in organic materials [78, 79]. Here, the external current J and the external bias V_{ext} was related to the quasi-Fermi level splitting, which was assumed to be constant throughout the whole active layer. This led to the equation:

$$qV_{int} = qV_{ext} - qdJ\sigma^{-1} \tag{2.5}$$

with σ being the conductivity, μ_{eff} the effective mobility and n_i the intrinsic charge in the active layer:

$$\sigma = 2q\mu_{eff}n_i \exp\left(\frac{qV_{int}}{2k_BT}\right). \tag{2.6}$$

At open circuit Equation 2.4 with $V_{ext} = V_{OC}$ and $V_{int} = V_{OC}$ becomes:

$$V_{OC} = \frac{k_BT}{q} \ln\left(\frac{J_G + J_0}{J_0}\right). \tag{2.7}$$

Assuming, that the dark saturation current $J_0 = qdk_2n_i^2$ is much smaller than the generation current J_G, Equation 2.4 with Equation 2.7 attains:

$$J = J_G\left(\exp\left(\frac{q}{k_BT}(V_{int} - V_{OC})\right) - 1\right). \tag{2.8}$$

Now, the last term of Equation 2.5 can be rewritten with Equation 2.6 and Equation 2.8:

$$\begin{aligned}\frac{dJ}{\sigma} &= \frac{dJ}{\sigma_i}\exp\left(\frac{qV_{OC}}{2k_BT}\right)\left(\exp\left(\frac{q(V_{int} - V_{OC})}{2k_BT}\right) - \exp\left(-\frac{q(V_{int} - V_{OC})}{2k_BT}\right)\right) \\ &= \frac{dJ}{\sigma_i}\exp\left(-\frac{qV_{OC}}{2k_BT}\right)2\sinh\left(\frac{q}{2k_BT}(V_{int} - V_{OC})\right),\end{aligned} \tag{2.9}$$

$\sigma_i = 2qn_i\sqrt{\mu_e\mu_h}$ is the effective intrinsic conductivity. With the small angle approximation for the sinus hyperbolicus, Equation 2.9 becomes:

$$\frac{dJ}{\sigma} = \alpha(V_{int} - V_{OC}), \tag{2.10}$$

with the dimensionless prefactor α being:

$$\alpha = \frac{qdJ_G}{\sigma_i k_B T} \exp\left(-\frac{qV_{OC}}{2k_B T}\right) \tag{2.11}$$

and Equation 2.4 for strict bimolecular recombination and at V_{OC}:

$$\frac{J_G}{J_0} = \exp\left(\frac{qV_{OC}}{k_B T}\right) \tag{2.12}$$

α then is related to all relevant material properties:

$$\alpha^2 = \frac{qd^3k_2J_G}{4\mu_e\mu_h k_B^2 T^2} \exp\left(-\frac{qV_{OC}}{2k_B T}\right). \tag{2.13}$$

Here, d is the active layer thickness, k_2 the bimolecular recombination rate, μ_e electron and μ_h hole mobility. With Equation 2.10, now Equation 2.5 becomes:

$$V_{ext} = V_{int}(1+\alpha) - \alpha V_{OC}, \tag{2.14}$$

leading finally to an analytical expression of the JV curve of organic solar cells [79]:

$$J = J_G\left(\exp\left(\frac{q(V_{ext} - V_{OC})}{k_B T(1+\alpha)}\right) - 1\right). \tag{2.15}$$

Note that this equation approaches the Shockley equation if alpha gets smaller than one. According to Equation 2.13, this is exactly the case for small currents, slow recombination, or high mobilities. This model has been used to successfully describe a range of organic solar cells [79–81] but will also be applied to colloidal PbS quantum dot solar cells in chapter 4.

By definition, the same parameters that determine the JV characteristic also affects the fill factor. One commonly used expression of the fill factor as a function of the V_{OC} was proposed by Green [82]:

$$FF = \frac{u_{OC} - ln(0.72 + u_{OC})}{u_{OC} + 1} \tag{2.16}$$

with the normalized open circuit voltage u_{OC} [82]:

$$u_{OC} = \frac{eV_{OC}}{n_{id}k_BT} \tag{2.17}$$

This equation is derived from the Shockley equation and only valid, if the maximum power voltage V_{mp} is close to the open circuit voltage. However, in case of severe transport limitations and by molecular recombination, u_{OC} should be written as [79]:

$$u_{OC} = \frac{eV_{OC}}{(1 + \alpha)k_BT} \tag{2.18}$$

Unfortunately, there is no analytical solution to relate the fill factor to the parameter α. Also, Equation 2.16 is no more valid. Instead, the following empirical expression provides a good approximation of the general dependence of the fill factor on u_{OC} [79]:

$$FF = \frac{u_{OC} - ln(0.79 + 0.66u_{OC}^{1.2})}{u_{OC} + 1}. \tag{2.19}$$

Figure 2.2 shows values of the fill factor as extracted from simulated JV-curves [80] as a function of α. The simulations considered a wide range of mobilities, various recombination coefficients and thicknesses, but there is only small scatter in Figure 2.2 a (open circles) [79]. For an α smaller than 1 an ideal behavior is described. Photocurrents in organic solar cells will become strongly transport-limited for α above one, resulting in a decrease of the fill factor [79]. This (and Equation 2.13) tells already, that high mobilities are needed to obtain high efficiencies as shown in Figure 2.2 b. Here, simulated power conversion efficiencies are plotted as a function of the band gap for different mobilities [78] and compared with the model of Scharber *et al.* [83]. Given the low and unbalanced mobilities of the organic materials

studied in this thesis (10^{-3} to 10^{-5} $cm^2\,(Vs)^{-1}$), there is much room to improve the efficiency of organic BHJ solar cells in the future.

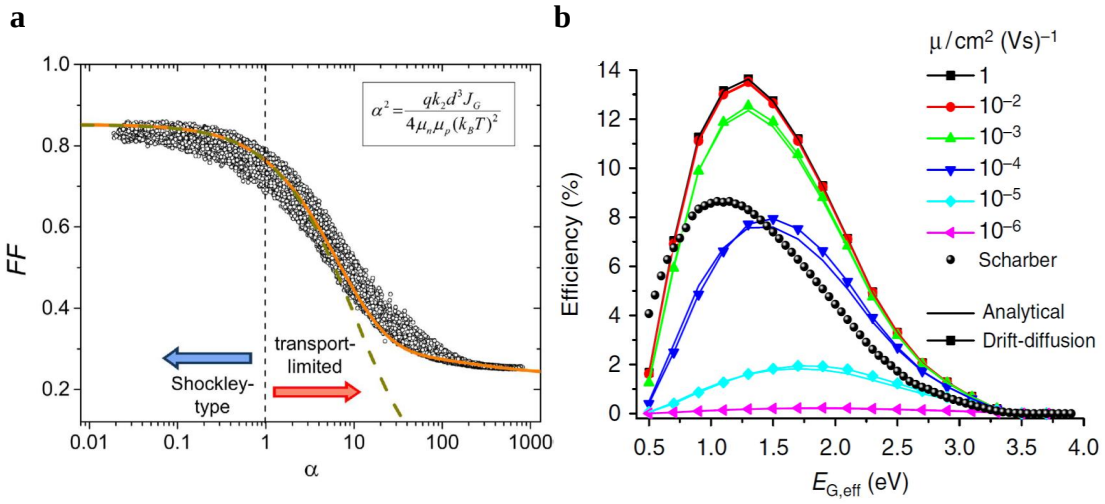

Figure 2.2.: Fill factor and Efficiencies (a) fill factor as a function of the parameter α (open circles) from simulated JV-curves [80] with the same mobilities for holes and electrons and a V_{OC} between 0.7 and 0.9 V. Dashed (solid) lines show analytical FF-α dependencies according to Equation 2.16 (and Equation 2.19). Figure reprinted with permission from Neher *et al.* [79]. (b) Power conversion efficiencies are plotted as a function of the band gap with an LUMO-LUMO offset between donor and acceptor of 0.5 eV for different mobilities calculated either via the analytical approach (thin lines with symbols, Equation 2.15) or via drift-diffusion simulations (thick lines) in comparison with the model of Scharber *et al.* [83]. Figure reprinted with permission from Würfel *et al.* [78].

Additionally, charge generation can be field dependent, which will reduce the fill factor and with that the efficiency. The analytical approach (Equation 2.19) does not account for *e.g.* field dependent charge generation, which is typically the case in organic solar cells. This motivates the work presented in this thesis to determine all parameters determining the efficiency of solar cells, from free charge formation to recombination and extraction.

2.2. Charge Generation and Geminate Recombination

There are three characteristic states which are involved in free charge generation; the singlet S_X, charge transfer (CT) (section 2.3) and charge separated (CS) states

(section 2.4). First, the formation of CT states is explained. The following discussion will focus on just one state, the thermalized CT state, which is known to be the precursor of the free charge pair [13, 84–86]. The question arises, how the charge bound in a CT exciton may finally overcome coulomb attraction. Different models were published to address this most crucial step for device performance, but up to now, none was found to precisely describe experimental results. The following sections will introduce the models which where published to describe the free charge generation process.

2.3. Involved States and Energetics

Here, the characteristic states involved in CT state formation are presented. A highly debated fundamental question is the effect of the excitation energy and how the so-called excess energy effects charge generation efficiency or field dependence. This excess energy can have its origin in the excitation of higher lying electronical (S_n, ..., S_m) with respect to S_1 or vibronically hot states. Therefore, all involved states and their transition rates need to be defined. The first step is to generate excited states by light absorption (black, green, blue arrows in figure Figure 2.3) or through injection of charges from the electrodes forming an exciton [87].

Since the majority of polymeric semiconductors have a singlet ground state of two paired electrons, light absorption usually results in a singlet excited state, which means, that they can be occupied by direct single-photon absorption. The excited state can decay radiatively or non-radiatively, via energy-transfer, dissociation or may diffuse through the material. If the excited singlet state on the donor polymer transfers one charge to the neighboring acceptor fullerene or vice versa; a CT-state is formed (red potential, Figure 2.3). The CT state is energetically located below the singlet donor and acceptor states as seen in electroluminescence experiments (Figure 2.3 b, blue line) [88].

The absorption and emission features of disordered organic semiconductors seldom consists of discrete peaks. For low frequency vibrations as shown in Figure 2.4 the spacing of the vibrational modes is smaller than thermal energy and thus CT-states are homogeneously broadened. Transitions only takes place for electronic energy levels, not for discrete vibrational modes. Optical transitions from thermally populated vibrational modes have absorption below E_{0-0} and emission above E_{0-0}.

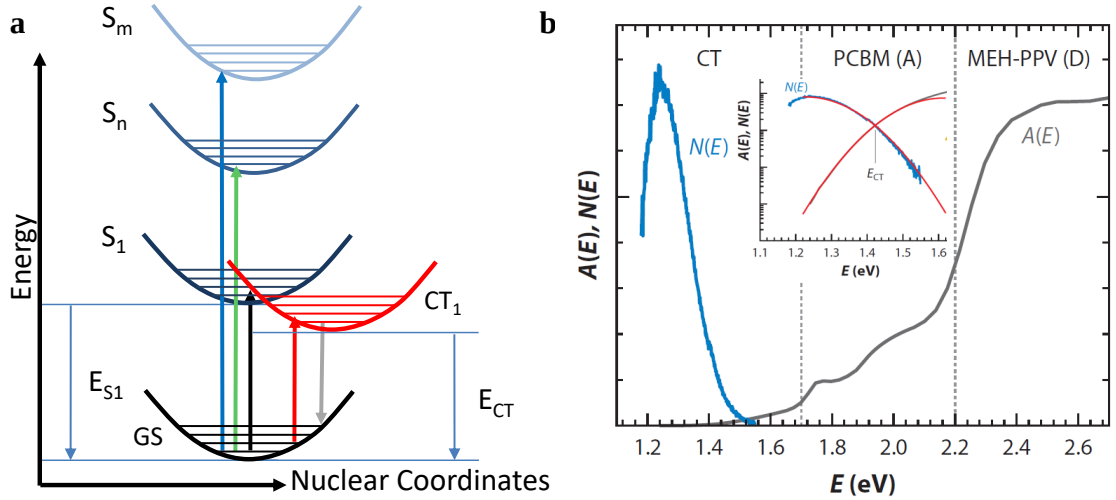

Figure 2.3.: Involved states in charge generation and excitation: (a) absorption of a photon leads to an excitation of an electron-hole pair from the ground state (GS) to an excited electronic state (S_1,... , S_n, ..., S_m in black, green, blue arrows, respectively) on the donor or acceptor, taking into account that the nuclear coordinate remains invariant during the transition (Franck–Condon principle). The lowest excited state S_1 defines the optical band gap with energy E_{S1}. If donor and acceptor materials are blended, a new state arises; the CT-state, which is per definition also coupled to the ground state and could be directly excited. The energy difference to the ground state of the vibrationally relaxed, but electronically excited CT_1 is E_{CT}. (b) Absorption $A(E)$ and emission $N(E)$ spectra of the DA blend MEH-PPV:PCBM. $N(E)$ is dominated by CT emission, which is below the optical gap. The inset shows $A(E)$ and $N(E)$ in the spectral region of CT absorption and emission, plotted on a logarithmic scale. At E_{CT}, the appropriately normalized $A(E)$ and $N(E)$ spectra cross. Figure reprinted with permission from Vandewal *et al.* [88]

If the photon energy $E_{0-0} - \lambda_L$ is within the absorption, the transition to the vibrational relaxed CT is most favorable. $E_{0-0} - \lambda_L$ is the photon energy were the emission is maximized (see Figure 2.3 b, left axis). The line shape can be described with Gaussians, if the low frequency vibrations are treated as harmonic oscillators;

for absorption:

$$A(E) \sim E \exp - \frac{(E - E_{0-0} - \lambda_L)^2}{4\lambda_L k_B T} \tag{2.20}$$

and emission:

$$N(E) \sim E^3 \exp -\frac{(E - E_{0-0} + \lambda_L)^2}{4\lambda_L k_B T}. \tag{2.21}$$

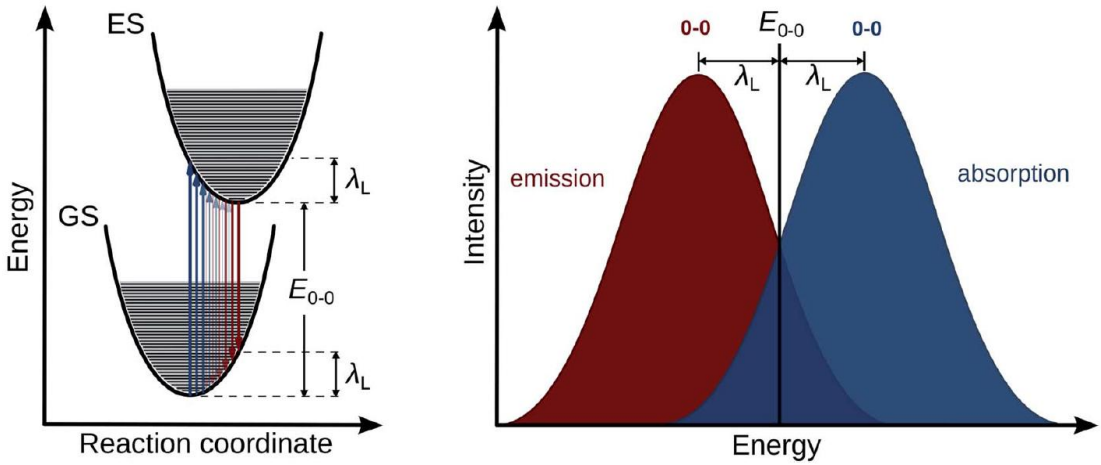

Figure 2.4.: Optical transitions depicted in an energy diagram with potentials for the ground state (GS) and excited state (E_S) Vertical blue arrows represent absorption and vertical red arrows emission. Absorption and emission spectra overlap around the electronic transition energy E_{0-0}. Peak broadening by low frequency vibrations with reorganization energy λ_L. The resulting peak width depends on temperature and λ_L. Figure depicted with permission from Ref. [89].

Here, E is the photon energy, λ_L the relaxation energy and E_{0-0} the energy difference between the vibrational relaxed ground- and excited CT state. If the corresponding reduced absorption ($A = \frac{A(E)}{E}$) and emmission ($EL = \frac{N(E)}{E^3}$) spectra are normalized to their maxima, then E_{0-0} is the crossing point as shown in Figure 2.4.

Typically, the CT state emission and absorption features of the vast majority of BHJ organic solar cells can be fit with gaussian line shapes as shown in Figure 2.3 b (inset, red lines) and also in chapter 6.

2.3.1. Onsager Model

The question, how the charge bound in a CT-exciton may finally overcome coulomb attraction was addressed by Onsager in 1938. He presented a model describing coulombically bound charge pair dissociation [90]. The main assumptions are,

that the geminate pair has an initial separation distance of r_0 and it diffuses via Brownian motion until it geminately recombines or dissociates under the influence of the Coulomb potential or the externally applied electric field. The dissociation yield at low internal electric fields is

$$\phi = \exp\left(-\frac{r_C}{r_0}\right)\left(1 + \frac{q^3\vec{F}}{8\pi\epsilon_0\epsilon_r k^2 T^2}(1+\cos\chi)\right) \tag{2.22}$$

with

$$r_C = \frac{q^2}{4\pi\epsilon_0\epsilon_r k_B T} \tag{2.23}$$

being the Coulomb capture radius. The angle between the geminate pair dipole moment and the electric field $\vec{F}$ is χ. The equation predicts that charge generation is activated by temperature and the activation energy is given by the Coulomb attraction E_b of the pair at the initial separation distance r_0.

$$\exp\left(-\frac{r_C}{r_0}\right) = \exp\left(-\frac{E_b}{k_B T}\right) \tag{2.24}$$

36 years later, this model was applied to extract the initial separation distance in anthracene single crystals excited at different photon energies and and yielded the result that high energy photons lead to an initial separation of several more repeating units when compared to low energy excitations [24]. However, a major aspect was not included; once a charge meets its counter charge, there is no probability to re-dissociate (e.g.: electrolyte [90] versus blend [91]).

2.3.2. Onsager-Braun Model

Onsager's model was extended by Braun in 1984 [92]. In Braun's theory the dissociation yield of the CT-state is expressed by competition between the field dependent dissociation yield $k_d(F)$ and the decay to the ground state k_f (black arrows in figure Figure 2.5 a):

$$\phi(F) = \frac{k_d(F)}{k_d(F) + k_f} \tag{2.25}$$

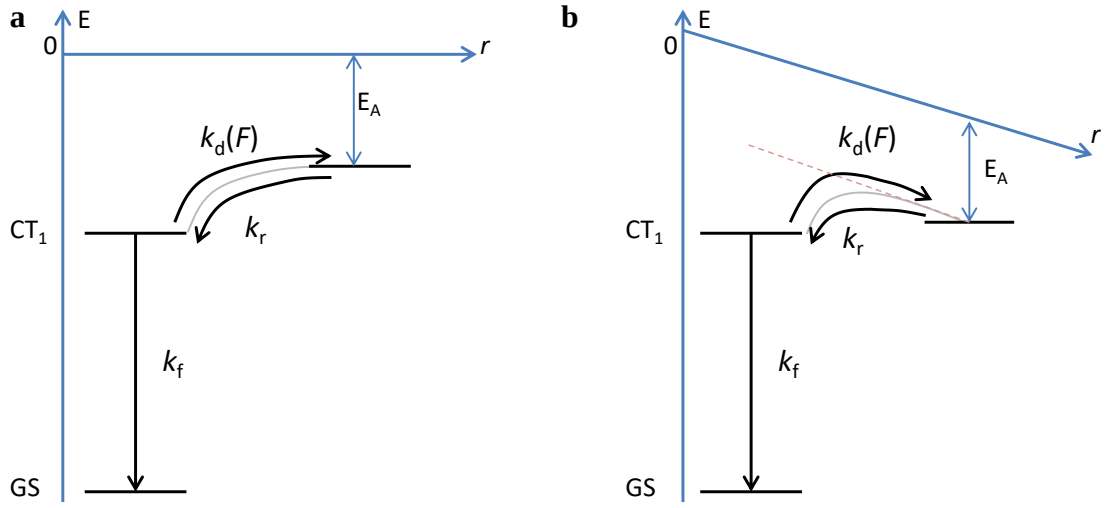

Figure 2.5.: Kinetics of charge transfer state dissociation (a) for a DA interface without externally applied electric field. From the CT state, recombination to the ground state (GS) occur with the rate k_f or dissociation with the rate k_d [92]. (b) DA interface with externally applied electric field F (dashed line) combined with the Coulomb potential (gray line from (a)) to yield the combined potential (gray line). It is evident, that for a sufficiently large electric field, the thermal energy is sufficient to overcome the remaining potential barrier. E_A is the electron affinity of the acceptor in the blend at infinite distance from the interface.

with $k_d(F)$ being field dependent according to:

$$k_d(F) = \frac{3k_2}{4\pi\epsilon_0\epsilon_r} e^{-\frac{E_b}{kT}} \frac{J_1(2\sqrt{-2b})}{\sqrt{-2b}} \tag{2.26}$$

and

$$b = \frac{e^3 F}{8\pi\epsilon_0\epsilon_r k^2 T^2}. \tag{2.27}$$

J_1 is the first order Bessel function, k_2 the recombination coefficient, E_b the Coulomb binding energy and F the electric field.

The Onsager-Braun model was applied successfully to the *e.g.* TPA:DPBDK donor acceptor system [93] and to single component materials *e.g.* MeLPPP [94].

The model relates dissociation to field and temperature which are directly accessible with TDCF. Figure 2.6 shows a comparison between measured data with TDCF (see section 3.3 and chapter 6) and the Onsager-Braun Model. All parameters were measured directly, except the initial separation distance r_0 and the built-in-field.

Nikolaos Ferdelekis conducted Monte-Carlo-Simulations on PCPDTBT:PCBM devices to closely match the JV curve and temperature dependent TDCF data. As a fit parameter the distance between two sites a_0 was assumed to be 1.8 nm and and the built in voltage 0.8 V. These values were also used in Figure 2.6.

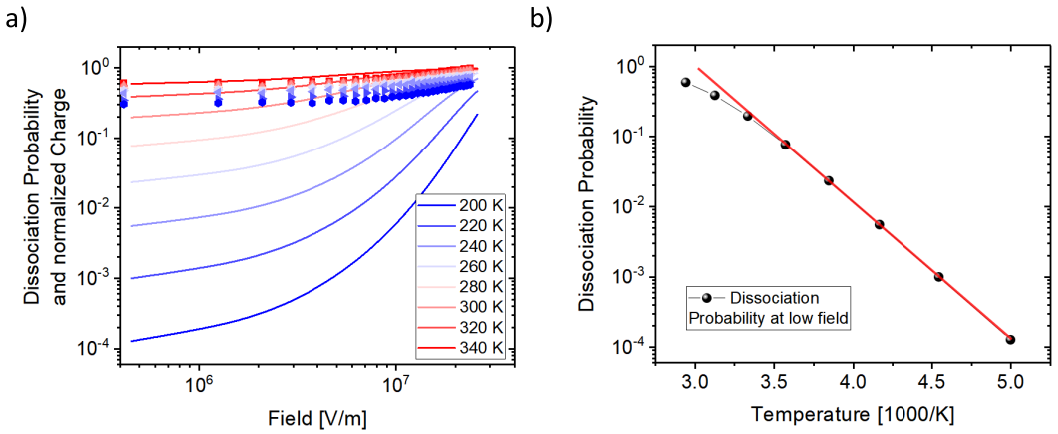

Figure 2.6.: Dissociation probability calculated with the Onsager-Braun Model (solid lines) compared to a TDCF experiment conducted at very short delay (4 ns) and at the same temperatures (symbols) as in the simulation (lines) for (a) a PCPDTBT:PCBM blend (see also chapter 6). (b) Simulated dissociation probability at low field ($5 \cdot 10^5 V/m$) for the temperatures in (a) with an Arrhenius-type fit (red line). It was not possible to simulate the measured data with values reported in literature and measured in this work.

Although successful applications exists [93], it is obvious that the model does not fit for BHJ solar cells (Figure 2.6a). Note, that temperature dependent TDCF measurements allow for a direct measurement of charge generation without the influence of non-geminate recombination. When trying to fit the photocurrent for a PCPDTBT:PCBM BHJ solar cell it turns out that fitting low field data leads to an overestimation of the large fields and vice versa (see figure Figure 2.6 a) [95, 96].

Despite the mismatch between experiment and theory regarding the absolute values for the dissociation efficiency in Figure 2.6 a, the Onsager-Braun model nicely predicts an Arrhenius type dependence of the dissociation probability on temperature as shown in Figure 2.6 b at low internal fields. The Arrhenius type temperature dependence of the dissociation probability is of general importance in chapter 6 to accurately obtain the activation energy for charge generation in BHJ solar cells.

Recently, within the framework of the Onsager-Braun model, a rate equation model was introduced by Armin *et al.* [55] to evaluate TAS data:

$$\begin{aligned}
\frac{\mathrm{d}n_{S_1}}{\mathrm{d}t} &= -k_{d,ex}n_{S_1} - k_{f,ex}n_{S_1} + \frac{n_{ph}}{t_p}\exp\left(-\frac{t}{t_p}\right) \\
\frac{\mathrm{d}n_{T_1}}{\mathrm{d}t} &= -k_{TA}n_{T_1}n_{CS} + k_{BET}n_{CT_3} \\
\frac{\mathrm{d}n_{CT_1}}{\mathrm{d}t} &= 0.25k_r n_{CS}^2 - k_d n_{CT_1} + k_{d,ex}n_{EX} + k_{ISC}(n_{CT_3} - n_{CT_1}) \\
\frac{\mathrm{d}n_{CT_3}}{\mathrm{d}t} &= 0.75k_r n_{CS}^2 - k_d n_{CT_3} - k_{BET}n_{CT_3} + k_{ISC}(n_{CT_1} - n_{CT_3}) \\
\frac{\mathrm{d}n_{CS}}{\mathrm{d}t} &= -k_r n_{CS}^2 + k_d(n_{CT_1} + n_{CT_3}) - k_{coll}n_{CS}
\end{aligned} \tag{2.28}$$

where n_{S_1}, n_{T_1}, n_{CT_1}, n_{CT_3} and n_{CS} are the densities of singlet and triplet excitons, singlet and triplet CT states and free charges, respectively. The number of absorbed photons is n_{ph} and k_{coll} is the collection rate of charges. Realistic values reported in the literature for the corresponding rates are $\sim 10^{13}$ for singlet exciton dissociation to the CT state $k_{d,ex}$ [97, 98], and $\sim 10^{10}$ for the singlet exciton decay $k_{f,ex}$ [99]. If the transient absorption experiment is not conducted at open circuit conditions, charges may be collected with the rate k_{coll}. However, features of CT states and free charges are not well distinguishable in photoinduced absorption spectra and thus, the measured signal is the sum of bound and free charge densities ($n_{CT}+n_{CS}$, see also Figure 2.7). Here, the rate equation model helps to estimate the densities in the respective states. Obviously, a plateau, which is related to the generated free charge, is reached in a dynamic equilibrium only if the initial excitation density is very low (Figure 2.7) a versus b).

The application of the rate equation model will be presented in chapter 6. Here, field dependent transient absorption spectroscopy is applied to an exemplary full device stack as described in chapter 3 in reflection and a small incident angle.

2.3.3. Two Pool Models

Several groups have proposed that photoexcitation of polymer:fullerene blends results in the occupation of multiple states, rather than a single state manifold. In particular, results from femtosecond pump-probe measurements suggested a two-pool model derived from a local morphologic or energetic perspective [100, 101].

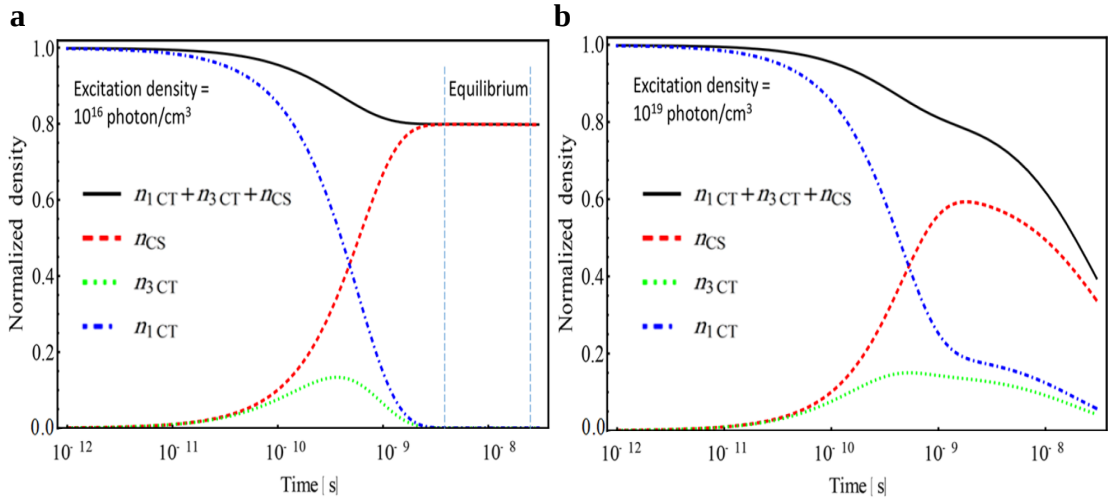

Figure 2.7.: Calculated densities and kinetics: of the CT state (blue line), CS state (red line) and the total charge (black line) for excitation densities of (a) 10^{16} cm^{-3} and (b) 10^{19} cm^{-3} photons. A plateau (black line), which is related to the generated charge, is reached in a dynamic equilibrium only if the excitation density is low (a versus b). Figure reprinted with permission from Armin *et al.* [55].

Barker *et al.* fit the TAS decay data with a distribution of recombination rates. The recombination dynamics appeared to be described by a rapid early decay that was fit with a narrow distribution of rate constants (Figure 2.8 a, red), followed by slower decay that demanded a broader distribution (Figure 2.8 a, blue). They attributed the faster decay to CT states in intermixed areas, with small separation distance which are prone to geminate recombination. Charge pairs separated in pure DA domains possess a large separation distance and split up easily into free charge carriers. This interpretation was confirmed by TAS measurements on P3HT:PCBM annealed and unannealed [101]. While the unannealed system is morphologically intermixed and leads to a stronger weighting of the faster recombination distribution, the annealed system is separated into pure phases and shows a slower distribution (Figure 2.8 a, bottom graph, red versus blue lines) [32, 101]. Other results from TAS measurements suggested, that dissociation of intramolecular excitons at the DA heterojunction forms either low energy bound CT excitons, prone to geminate recombination but contributing very little to free charge generation (Figure 2.8 b, mechanism 1), or more delocalized higher energy bound polaron pairs, which exhibit a low probability for geminate recombination but a high efficiency to split into free charges (Figure 2.8 b, mechanism 2) [100–102].

Field-induced photoluminescence (PL) quenching studies also suggested a two-pool

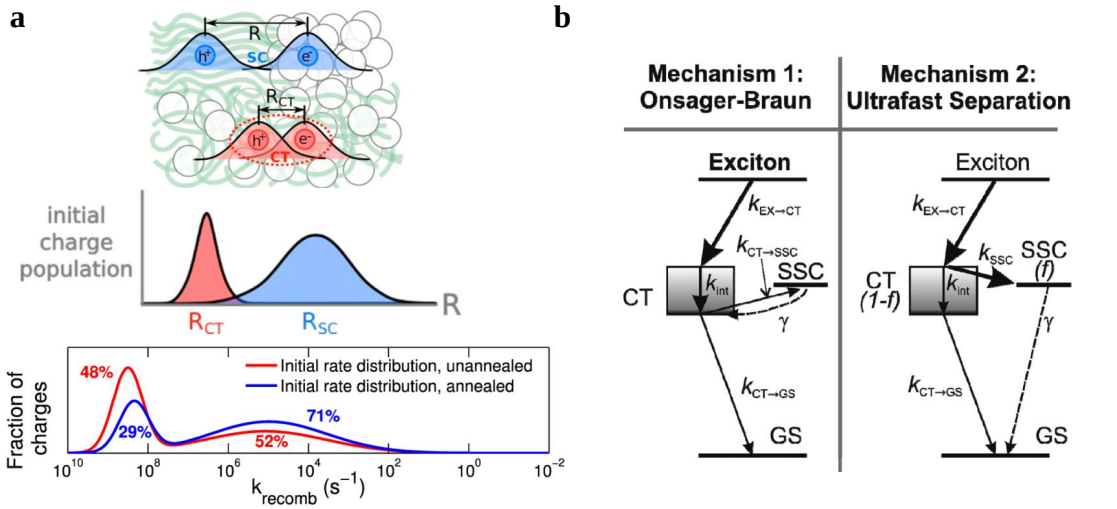

Figure 2.8.: Proposed two pool models from Ultrafast Experiments: (a) By fitting recombination dynamics obtained with TAS to distributions of recombination rates, Barker *et al.* identified populations of CT states (red) and spatially well separated charges (blue). Here, the charge separation distance is R, which is small in highly intermixed regions and large in well separated domains. The lower Graph shows the corresponding double gaussian distribution of recombination rate constants to fit TAS data for annealed (blue) and unannealed (red) P3HT:PCBM blends. Figure reprinted with permission from Barker *et al.* [101]. (b) Proposed mechanism by Howard *et al.*: In the first case the thermalization of the CT state is faster than separation; charge separation and recombination are mediated by the thermalized CT state. In the second case, the spatial separation of charges in hot CT states created directly after excitation rivals the rate of internal conversion in the CT manifold. In this case, spatially separated charges (SSC) are generated on a ultrafast time scale faster than 100 fs. Figure reprinted with permission from Howard *et al.* [100].

model derived from a morphological perspective, where photoexcitation populates CT manifolds either in the intermixed and more disordered phases and CT states at domain boundaries [87]. Only the latter are connected to the free charge reservoir, meaning that they are involved in free charge formation and emit in electroluminescence (EL). CT states formed in the intermixed phase are largely confined; they undergo geminate recombination and contribute mostly to the photoluminescence. In both models, if there is little coupling between these two state manifolds, the efficiency of free charge formation will be determined by the initial branching ratio, meaning that it is decided on a very early time scale, before thermalization is complete, whether exciton dissociation occupies fully bound or dissociable CT states [101, 103].

2.3.4. Interface Energetics

In combination with an energy driven charge separation, morphology plays a central role. There are not necessarily only two domains with either donor polymer or acceptor fullerene aggregates. Instead, the morphology at the BHJ interface might be different and a third (intermixed) phase has been proposed [104–107]. Such a different morphology introduces a slight shift of the corresponding HOMO and LUMO levels aiding in stabilization of separated charges in their respective pure donor or acceptor rich domains as shown in Figure 2.9 a. A three phase structure with an energy cascade for the electron or the hole increases the CT state splitting probability [106]. In combination with a high local charge carrier mobility and long CT state lifetime, the three phase structure explains efficient charge generation in some bulk heterojunction solar cells [106, 107]. At a nanometer length scale, charge transport from the intermixed to aggregated phases could occur along a single polymer chain, resulting in initial extremely high local mobilities [106, 108] finally assisting charge generation.

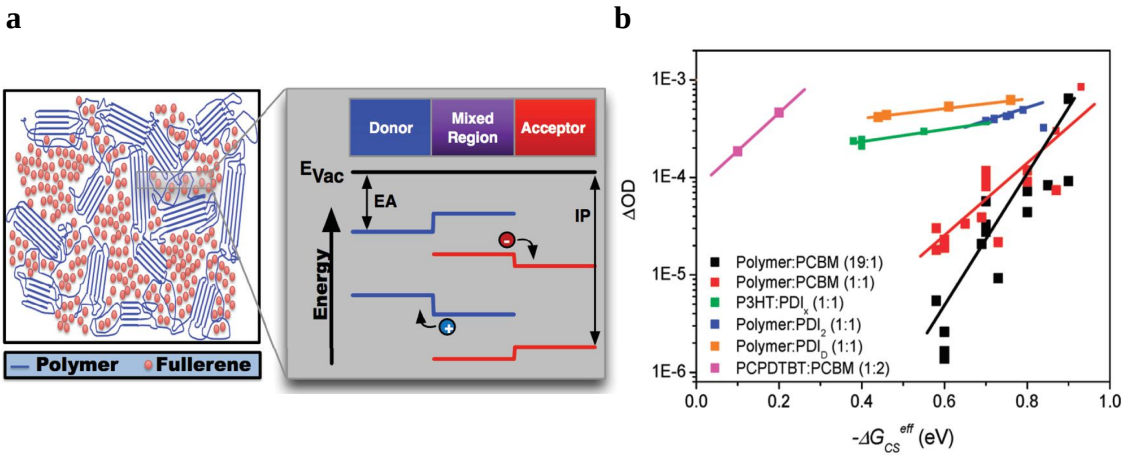

Figure 2.9.: (a) BHJ solar cell with the mixed region (left). Potential shifts in the local energetic landscape at the phase borders between the donor, mixed and acceptor (right). EA is the electron affinity, IP is the ionization potential. Figure reprinted with permission from Burke *et al.* [106]. (b) Correlation between the TAS assay of the yield of dissociated charges versus the driving force for charge photogeneration. Figure reprinted with permission from Shoaee *et al.* [104].

The energetic alignment at the BHJ interface, the donor LUMO acceptor LUMO offset is proposed to be the driving force for charge generation $\Delta G = E_{S_1} - E_{CT}$ [104]. The Coulombic attraction of CT states results in an energy barrier to their

dissociation [11, 104]. Shoaee *et al.* proposed the concept that excess thermal energy of the initially formed CT state can help to overcome the energy barrier. Here, the CT state splitting into free charges is directly linked to the magnitude of the excess vibrational energy. A direct correlation between the acceptor LUMO level and the efficiency of charge dissociation (Figure 2.9 b) was found [104]. The acceptor LUMO level offset was also assigned to the dissociation of interfacial charge transfer states being dependent upon the excess thermal energy of the initial CT state [104]. This concept was theoretically supported by Peumans *et al.* [109].

2.4. Charge Extraction and Nongeminate Recombination

The charge transfer (CT) state is split into free charges that subsequently are transported to the electrodes. The last step in this chain of events constitutes a charge transport problem that may massively influence the field dependence of photocurrent in the device.

2.4.1. Charge Extraction

Organic bulk heterojunction solar cells are examples of systems with significant morphological and energetic disorder.

Perfect conjugation of infinite long polymer chains would suggest a band-like transport along the chains as found in inorganic crystalline semiconductors. However, disruptions and defects breaks the chain in smaller conjugated units leading to an ensemble of sites with varying energetic levels and slightly different distances [111]. The charge carriers are more constrained in space and the concept of band transport is not applicable. The charge carriers have to hop from one site to the neighboring site. As a consequence, equilibrium charge carrier mobilities investigated with steady state techniques (*e.g.* space charge limited currents, lower path in Figure 2.10) in organic semiconductors are typically several orders of magnitude lower than in their inorganic opponent and present a limiting factor to device performances.

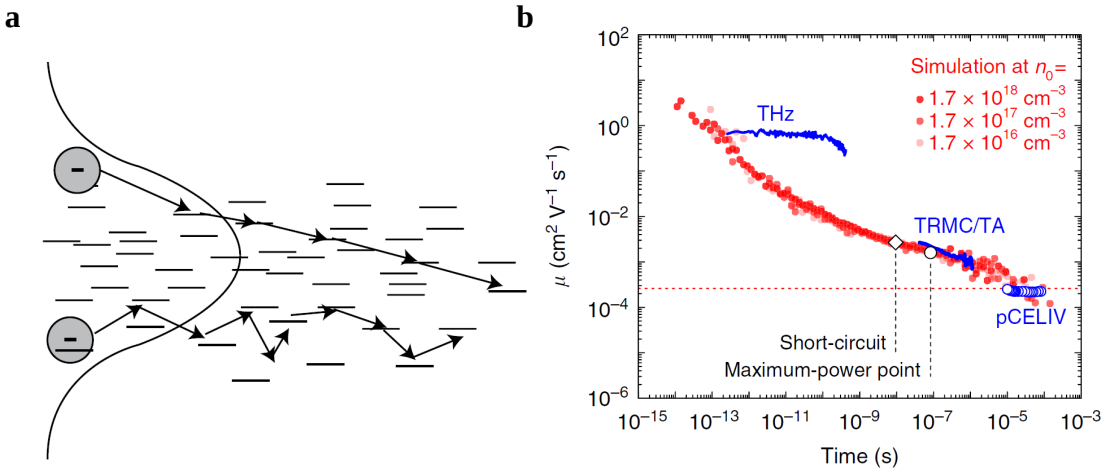

Figure 2.10.: Charge carrier thermalization. (a) An energetic cascade allows for faster carrier extraction (and recombination) compared to hopping at the low energy side of the DOS. Picture adopted from [110]. (b) Simulated time-dependent mobilities at indicated DOS occupancies n_0 compared to experiments (blue symbols). The time-dependent mobility of both the electrons and the holes is pump-fluence independent in agreement with the experiments. The red dashed line indicates the equilibrium mobility. Figure reprinted with permission from Melianas *et al.* [44].

Often, the Miller-Abrahams rate ν_{ij} is used to describe the hopping process from site i with the energy E_i to site j with E_j:

$$\nu_{ij} \propto \exp\left(-2\gamma r_{ij}\right) \begin{cases} \exp\left(-\frac{E_j - E_i}{k_B T}\right), & E_j > E_i \\ 1 & , \; E_j < E_i \end{cases} \tag{2.29}$$

where r_{ij} is the distance between the transport sites and γ is the inverse localization radius. From Equation 2.29 it is obvious that the hopping transport is temperature activated. Because the hopping sites energy also enters, the shape of the density of states, which represents the distribution of transport states in energy, dictates the properties of charge transport [112]. A Gaussian distribution with the width σ is commonly used to describe the density of states of disordered systems as shown in Figure 2.10 a [113]. Based on Monte Carlo simulations, Bässler *et al.* investigated the temporal evolution of the charge distribution [114]. The time the charge carriers need for thermalization is given by t_{th}, which can be estimated by [114, 115]

$$t_{th} = 10 \cdot t_0 \exp\left(-1.07 \cdot (\sigma / k_B T)^2\right) \tag{2.30}$$

were t_0 is the dwell time of a carrier on a site in a lattice without disorder [114]. If the probed time scales are smaller than t_{th} the charge transport becomes strongly dispersive and the mobility will decrease with time. When the equilibrium has established, the mobility is time-independent and approaches steady state mobilities (Figure 2.10 b, red dashed line) [112, 114, 115].

Melianas *et al.* combined transient electro-optical experiments (TREFISH) and kinetic Monte Carlo modeling [41] on the polymer:fullerene system TQ1:PCBM [116] to show that early time charge transport in such devices is orders of magnitude faster [44] than the reported near-equilibrium mobilities usually studied with steady state techniques [45]. The transport was found to be very dispersive, leading to orders of magnitude of spread in mobilities under operational conditions [39, 44, 117]. The motion of photogenerated charges is highly diffusive and governed by relaxation in the homogeneously broadened density of states as shown in Figure 2.10 b.

Dispersive effects such as time-dependent mobilities and dispersive recombination have been reported for a number of DA blends [23, 41, 118]. Recent studies have suggested that dispersive transport might be beneficial for efficient charge extraction [117]. This was rationalized by the high mobility of photogenerated charges at early time scales and their potentially slow thermalization in a broadened DOS. Extraction may take place before charges are fully thermalized (upper path in Figure 2.10 a).

The key parameters for extraction are the electron and hole mobilities, both set the time needed by the photogenerated charges to be extracted by the externally applied electric field F with the mobility $\mu = vF^{-1}$, and determine how fast electrons and holes recombine [119].

Furthermore, the power law slopes of $\mu(t)$ shown in Figure 2.10 b are similar to that of $k_2(t)$ [118] as discussed in the next section, and it is therefore reasonable to assume that the bimolecular recombination coefficient is directly proportional to the mobility $k_2(t) = B\mu(t)$, where B is a constant [115]. This effect plays an important role in nearly amorphous blends as will be discussed in chapter 5.

2.4.2. Non-geminate Recombination

Non-geminate recombination is defined by the fact that the two charges were generated independently of each other, in the case of organic solar cells thus come from different CT states. The recombination process is mainly characterized by its reaction order. Depending on the number of involved reactants, the recombination processes are distinguished in monomolecular, bimolecular and higher order recombination. In principle, their corresponding rate constants can also depend on the time.

Monomolecular Recombination

Here, the recombination rate depends linearly on the charge density n:

$$\frac{\mathrm{d}n}{\mathrm{d}t} = -k_1 n \tag{2.31}$$

with k_1 being the monomolecular recombination coefficient. For purely first order recombination, the temporal evolution of the charge density follows the exponential function:

$$n(t) = n_0 \exp\left(-k_1 t\right). \tag{2.32}$$

In organic semiconductors a recombination center can *e.g.* be a deep trap occupied by an electron, which recombines with a mobile hole. This trap assisted recombination was described by Shockley, Read and Hall (SRH) [120]. The recombination rate R_{SRH} is given by:

$$R_{\mathrm{SRH}} = \frac{C_e C_h N_t n p}{C_e n + C_h p} \tag{2.33}$$

where C_h and C_e are the hole and electron capture coefficients, respectively, n and p are the photogenerated electron and hole densities and N_t is the density of trap states.

Bimolecular Recombination

Bimolecular recombination involves two independent charge carriers. For photogenerated charges, electron and hole densities are equal and the recombination rate only depends on the second power of n:

$$\frac{\mathrm{d}n}{\mathrm{d}t} = -k_2 n^2, \tag{2.34}$$

where k_2 is the bimolecular recombination coefficient. Most organic semiconductors consist of materials with low mobilities. Here, the rate limiting step is the probability of two oppositely charged carriers to find each other. This process has been studied by Langevin in the last century [56, 59] for the recombination of ions in gases, a homogeneous isotropic media. Recombination inescapably takes place as the distance between the electron and the hole decreases below the Coulomb capture radius (Equation 2.23). The recombination depends on the drift velocity of the two charges in their mutual Coulomb field F towards each other when entering the Coulomb capture radius. From the point of view of the hole, the electron moves with the sum of both mobilities $\mu = \mu_e + \mu_h$ and integration of the average electron current density $J = qn\mu F$ is the total electron current entering the sphere:

$$I_e = n\frac{q^2}{\epsilon_0 \epsilon_r}(\mu_e + \mu_h) \tag{2.35}$$

The entire current I_e recombines with the hole. Hence, the Langevin recombination coefficient k_L can be defined as [56]:

$$k_L = \frac{q}{\epsilon_0 \epsilon_r}(\mu_e + \mu_h) \tag{2.36}$$

Surprisingly, this theory has been effective in describing recombination in single component systems, such as OLED devices and thus is often applied to describe recombination in DA blends, where electrons and holes are on different donor or acceptor phases and recombination occurs only at the DA interface. But, in most

cases a reduced Langevin recombination process is found [55, 61, 75, 118]. The Langevin reduction factor ξ_L can be written as:

$$\xi_L = \frac{k_L}{k_2}. \tag{2.37}$$

In some material combinations a Langevin reduction factor of up to $\xi_L = 10^4$ was reported [121]. However, the reduction factor strongly depends on the material selection and preparation conditions and therefore it has not yet been possible to predict.

Higher Order Recombination

In some material combinations a recombination order exceeding 2 has been published [122–124]. The recombination rate then becomes:

$$\frac{\mathrm{d}n}{\mathrm{d}t} = -k_\alpha n^\alpha, \tag{2.38}$$

with the reaction order α. A reaction order of three is the Auger recombination in which excess energy is given to a third carrier, which will be excited to a higher energy level without moving to another energy band. After the excitation, the third charge usually loses its excess energy *via* thermalization. This process is a three carrier interaction and is normally only relevant at very high carrier densities. Additionally, the Auger process is not easily probed experimentally, because the third particle must begin in an unstable excited state [125].

Apparent recombination orders α with values below or above two have also been observed [124, 126–128], and are rationalized by a charge carrier density dependent effect. If the mobility itself or the recombination coefficient depends on the charge carrier density the apparent recombination order might be different, although the predominant recombination process is bimolecular.

Time dependent Recombination

If the mobility is time-dependent, it may follow that the recombination rate is also time-dependent. This is the case especially in disordered organic semiconductors materials, because it is expected that the larger the energetic disorder, the

stronger are dispersive effects. A typical characteristic of dispersive recombination in a Gaussian or exponential density of states (DOS) distribution is that nongeminate recombination is competing with charge thermalization [36, 118, 129]. The recombination rate, the coefficient $k_{\alpha(t)}(t)$ and the apparent reaction order $\alpha(t)$ becomes a function of the time:

$$\frac{\mathrm{d}n}{\mathrm{d}t} = -k_{\alpha(t)} n^{\alpha(t)}. \tag{2.39}$$

Here $\frac{\mathrm{d}n}{\mathrm{d}t}$ decreases more rapidly at low initial charge densities. At higher charge densities, recombination speeds up because of the power law dependence on n [130], now competing with thermalization. Figure 2.11 a shows the situation in a Gaussian density of states (gray), where a charge carrier package (blue) is initially generated upon pulsed illumination with an energetic distribution similar to the DOS. Here, ϵ^* markes the maximum of the density of occupied states (DOOS). Upon thermalization, ϵ^* approaches the position of the Fermi level ϵ_F and the recombination coefficient becomes a sole function of carrier density. Finally, for very low carrier densities, the carrier package centers at the energy ϵ_∞ (which is a function of the width of the Gaussian distribution) and non-geminate recombination is independent of time and carrier density. In principal all three cases shown in Figure 2.11 a and b should be experimentally observable as predicted by Hofacker *et al.* [129]. After pulsed excitation by a short laser pulse the total charge carrier density is measured at different delay times. From these $n(t)$ data $\frac{\mathrm{d}n}{\mathrm{d}t}$ can be derived. With this, Equation 2.39 can be visualized plotting $\frac{\mathrm{d}n}{\mathrm{d}t}$ versus n as shown in Figure 2.11 b.

Time dependent recombination rates were originally proposed within the framework of Orenstein and Kastner [36] and Scheidler and Bässler [47]. They proposed a time dependent recombination rate following a power law $\mathrm{d}n/\mathrm{d}t \propto t^{-1}$ upon increasing energetic disorder (σ) [36], while for decreasing σ, $\mathrm{d}n/\mathrm{d}t \propto t^{-2}$ is recovered at long times [47]. The bimolecular recombination coefficient $(\mathrm{d}n/\mathrm{d}t)/n^2(t)$ shown in Figure 1.7 b decreases with time and does not approach a constant value at longer times for a large energetic disorder, whereas for small σ an equilibrium is reached at longer delay times [47]. Figure 2.11 c shows theoretical predictions for monomolecular and bimolecular recombination in transient photocurrent measurements (TPC) [36]. Here, the photocurrent is logarithmically plotted versus time. At short times n is $\propto t^{-1+a}$ for monomolecular and bimolecular recombination and

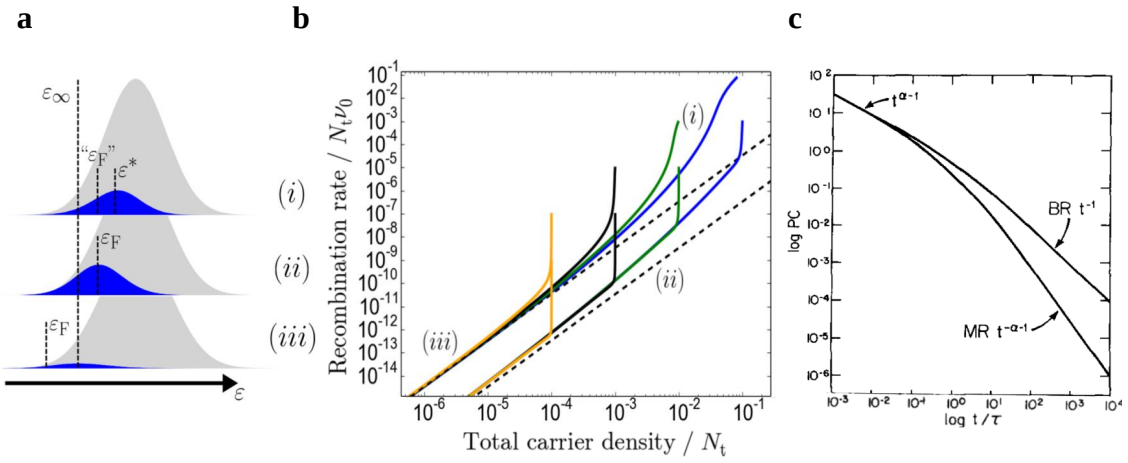

Figure 2.11.: Dispersive recombination in organic disordered semiconductors. (a) Charge carrier package (blue) in a Gaussian DOS (gray). The peak of the package is approximated by ϵ^*. (i) non-thermalized carriers with an energy $\epsilon^* > \epsilon_F$ above the quasi-Fermi level ϵ_F, (ii) thermalized carriers with $\epsilon^* = \epsilon_F$, (iii) thermalized or non-thermalized carriers with $\epsilon^* = \epsilon_\infty$. (b) Recombination rate as a function of remaining charge carrier density after pulsed excitation for different fluencies in a Gaussian DOS. Figure (a) and (b) reprinted with permission from Hofacker and Neher [129]. (c) Theoretical predictions for monomolecular (MR) and bimolecular (BR) recombination by Orenstein and Kastner [36] in transient photocurrent measurements. Here, the photocurrent is logarithmically plotted versus time. At short times n is for both cases $n \propto t^{-1+a}$ and changes only for bimolecular recombination to $n \propto t^{-1}$. Figure reprinted with permission from Orenstein and Kastner [36].

changes only for bimolecular recombination to $n \propto t^{-1}$ at larger delay times. Time dependent recombination processes will be discussed in chapter 5.

Chapter 3

Experimental Part

3.1. Organic Photovoltaic Devices

All devices studied in this work are designed according to Figure 3.1 with only slight deviations, like different materials for the active layer or the selective transport layers. The substrates were procured from Lumtec. Lumtec sputters ITO through high-precision laser cutted shadow masks on glass substrates with a sheet resistance of 15 Ω and a maximum roughness of 35 nm.

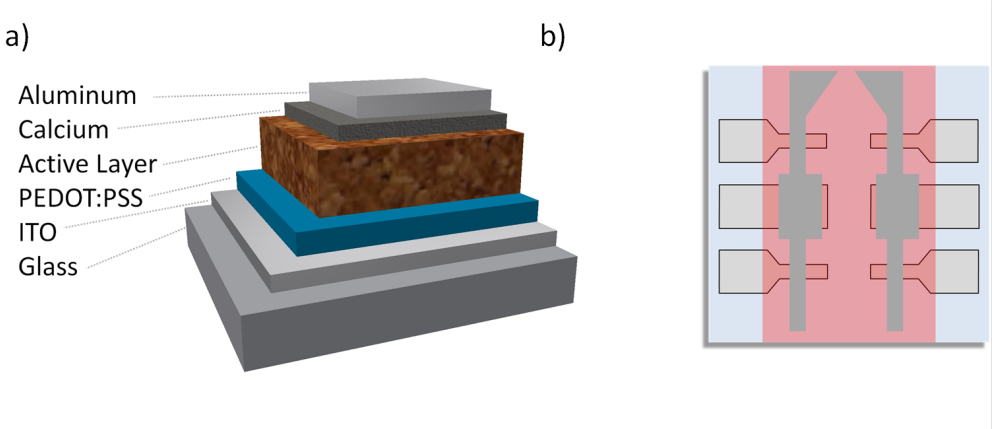

Figure 3.1.: Typical device architecture of an organic photovoltaic device: a) illumination enters the device from the bottom through the glass substrate with structured indium tin oxide (ITO) on top. A thin transparent hole transporting layer and the organic active layer are spin coated on top. The device is finalized with an evaporated calcium aluminum electrode for collecting electrons and encapsulated with epoxy resin and a glass lid. b) Structured ITO (light grey) with different sizes for transient measurements (1.1 mm^2) and steady state device characterization (16 mm^2) defined by the cross section with the electrodes evaporated through a shadow mask. The active layer (transparent light red) is sandwiched in between the structured electrodes.

As shown in Figure 3.1b) small pixels (defined by the cross section of the light and dark gray electrodes) are used for transient electronic experiments, where a low RC-time is mandatory. Therefore the sheet resistance and pixel size has to be as small as possible, but large enough to still get reliable results. The best compromise turned out to be an active area of 1.1 mm^2 in combination with a large contact pad, which could be also metalized by post-evaporation of silver or highly conductive silver ink for transient measurements and a large pixel for trustworthy steady state measurements, *e.g.* current-voltage-characteristics, as edge effects and very small deviations in the active area are nearly negligible. The active layer thickness used in this work is in the range of 70 to 400 nm. A thin layer is needed due to the poor hole mobility in most organic donor materials of $\sim 10^{-5}$ $cm^2\,(Vs)^{-1}$compared to silicon ~ 400 $cm^2\,(Vs)^{-1}$[131]. On the other hand, a thick layer is needed to absorb most of the incident light (section 2.1).

3.2. Methods

Many contradictory and unclear models for free charge generation were also developed having their origin in non-ideal measurement conditions. For instance, Transient Absorption Spectroscopy (TAS), an ultrafast pulsed all optical pump-probe-method, usually suffers from high fluences. Also, as outlined above, it is often difficult to separate the TAS signal into *e.g.* contributions from CT states and free charges. Charge carrier densities at these high fluences are in excess of that density generated at least at ten suns[1] in the best case [132]. Steady state measurement conditions, as in *e.g.* jV-, EQE and IQE measurements, are referred to as being ideal for characterizing solar cells as their later application will only be steady state. Unfortunately, it is very difficult to separate field dependent generation and extraction, and to discriminate between different recombination processes. TDCF is a powerful technique to study these processes for application-relevant carrier densities, but the time resolution is often limited. Therefore a new setup was designed to tackle the experimental challenges common established techniques are facing.

The key conditions needed to combine the "best of two worlds", ultrafast pulsed laser techniques and high resolution optoelectronic methods. First, a sufficient

[1] One sun: AM1.5G, 100 $mW\,cm^{-2}$

time resolution had to be established to be able to distinguish between free charges being generated and their recombination, second, the methods being sensitive to the extractable charge only and finally combine all methods to find their common results. In this chapter the experiments and their realization were introduced in more detail to the reader.

For the TDCF and TAS experiment a research proposal was handed to the *Deutsche Forschungsgemeinschaft* (DFG) and approved[2]; the centerpiece is a fs-TiSa Laser (Coherent Libra 4 mJ, 800 nm, 46 fs pulses) which pumps a Coherent Opera Solo Non-collinear Optical Parametric Amplifier (NOPA) (Figure 3.4) providing a large photon energy range from 290 to 2700 nm. The Coherent Libra is a *one box* system containing the seed laser (Coherent Vitesse) a stretcher, the ns pump laser (Coherent Evolution), the regenerative amplifier and the compressor. The Coherent Libra utilizes chirped pulse amplification [49]. Here, the ultrashort laser pulse (from Coherent Vitesse) is stretched in time prior guiding it to the gain medium utilizing a matched pair of gratings that are arranged such that the long-wavelength component of the laser pulse travels a shorter pathway than the short-wavelength component. After the grating pair, the laser pulse becomes positively chirped and has longer pulse duration than the original. The stretched pulse, whose intensity is now low is introduced to the gain medium and amplified with a high power (20 W) 532 nm ns-Laserpulse from the Coherent Evolution. Finally, the amplified laser pulse is compressed to the original pulse width through the reversal process of stretching with another grating pair, achieving orders of magnitude higher laser pulse peak power than laser systems could generate without amplification [49].

For all experiments presented in this work, a highly stable laser system is mandatory. Due to the non-linear conversion in the NOPA, already the fundamental has to be as stable as possible. Therefore all components were optimized before every measurement set: The internal Pockels-cells timing is ensured with a high precision (25 ps Jitter) delay Generator (8 channel Coherent SDG, see also Figure 3.3d). An optimum setting for the so called *build-up* in the regenerative amplifier (central part of the Coherent Libra), is defined by delay 1 and 2, are 3054.5 ns and 3240.75 ns respectively, whereby delay 2 is important to optimize the pre- to main-pulse contrast ratio to at least 1:10000. Once the timings are optimized and the optical parts inside the Libra are perfectly aligned, the temperature settings were optimized for a maximum output power of the coherent evolution pump laser (see Figure 3.2),

[2]INST 336/94-1 FUGG

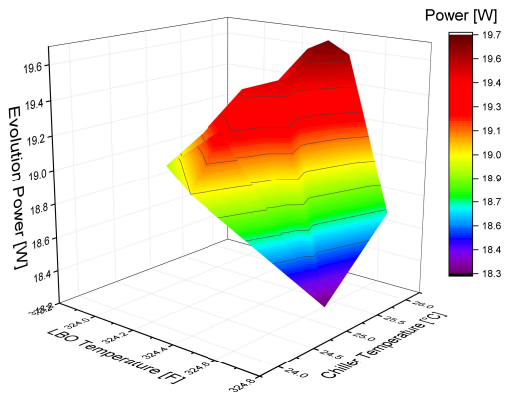

Figure 3.2.: Optimization of the Coherent Evolution Laser output power by adjusting only the LBO crystal and chiller temperature.

resulting in an Libra output power of 3.74 μJ cm^{-2} (0.25% rms / 24 h) measured with an Ophir Juno PE-10-C Powermeter. This fundamental pulse energy enables a stable (3% rms / 24 h at 520 nm) operation of the NOPAs.

The Coherent SDG delay generator has in total 8 channels and the remaining 5 channel provide central trigger signals for all experiments. Roughly 3 μs delay is enough time to start triggering other instruments earlier, such that *e.g.* for TDCF, excitation and extraction voltage pulse can start exactly at the same time or earlier. In previous versions of TDCF at the University of Potsdam the trigger pulse originated from the same laser pulse, the light needed to be delayed by the time the function generator needs from the time the external trigger pulse arrives to the actual output of the collection voltage pulse [133]. The optical delay was realized with a 85 m long silica fiber.

Once the Libra is aligned, the beam is magnified in diameter with a telescope (see Figure 3.4) and guided to both NOPAs inputs while separated in three paths with 75:25 (R:T), 50:50 ultrafast beamsplitters for white light generation and NOPAs, respectively. The mirrors in-front of the NOPAs are used to center the beam onto second irises (A2 in the Coherent OperA Solo manual). The converted light from the NOPA is delivered at four different outputs, flipping mirrors and periscopes are used to guide the light from NOPA I through the delay line, chopper, polarizer, motorized mirror, beamsplitter and finally the sample as shown in Figure 3.4. The same sample position is used for TDCF and TAS. The converted infrared light from NOPA II is used for white light generation in the near infrared part of the probe spectrum.

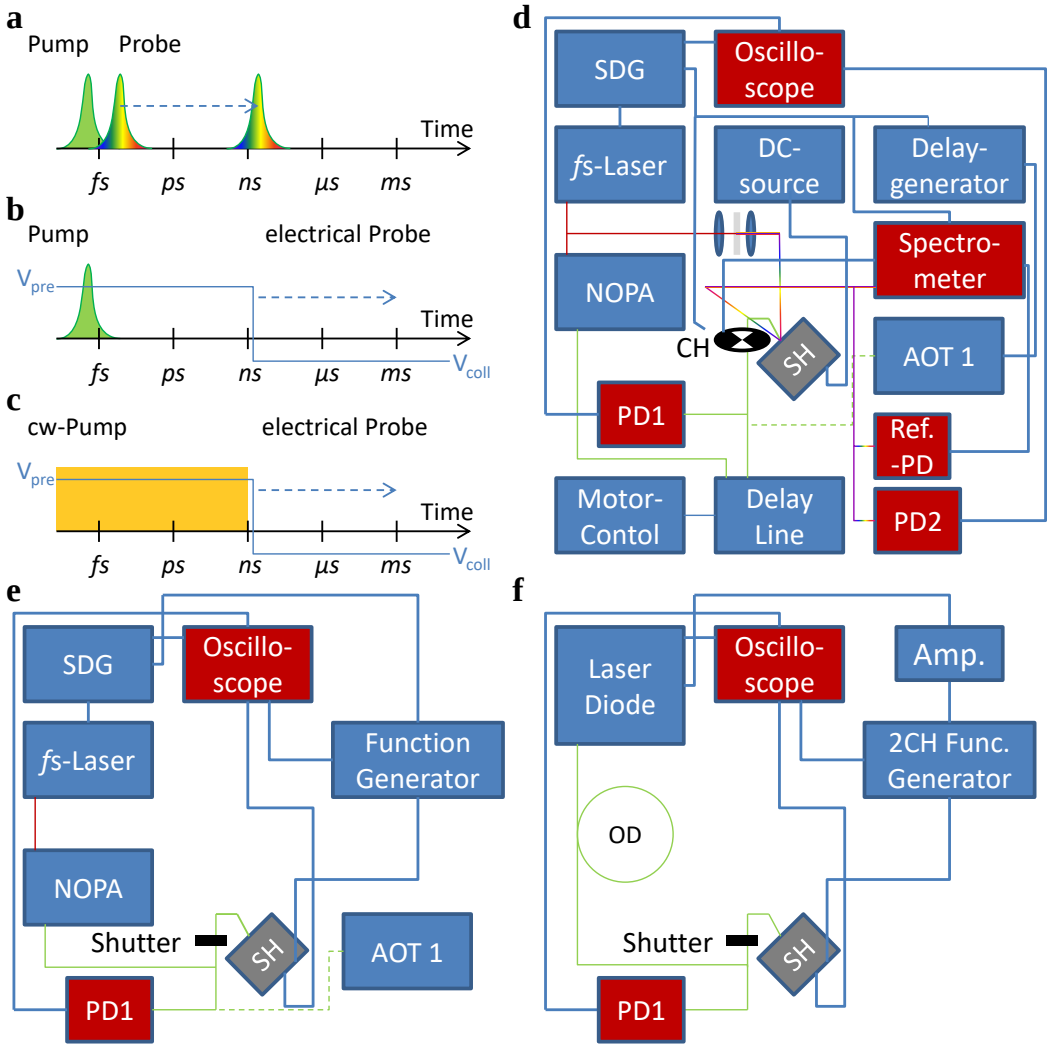

Figure 3.3.: Experimental time ranges and instrument network: time range on which a (a) transient absorption (TAS), (b) time delayed collection field (TDCF) or (c) bias assisted charge extraction (BACE) experiment could be performed. (d) Schematic of a basic TAS setup with the main time controlling unit, the synchronization and delay generator (SDG) which controls the pockels-cells of the coherent Libra regenerative amplifier (*f*s-Laser), the chopper (CH) for blocking every second pump-pulse, SRS delay-generator for electrically delayed laser pulses with a *p*s-laser (AOT 1) and delivers a trigger to the oscilloscope. With two photodiodes, the delay between pump (PD1) and probe (PD2) can be checked in order to adjust the beam path lengths. The spectrometer records simultaneously a visible and near-infrared spectrum and additionally to every spectrum, the chopper state, position of the delay-stage and reference diode amplitude. The reference diode (Ref.-PD) monitors the white-light- or pump intensity. (e) Schematic of TDCF and (f) BACE, with a fast switchable cw-laser-diode whose light is homogenized and delayed in an optical fiber (OD).

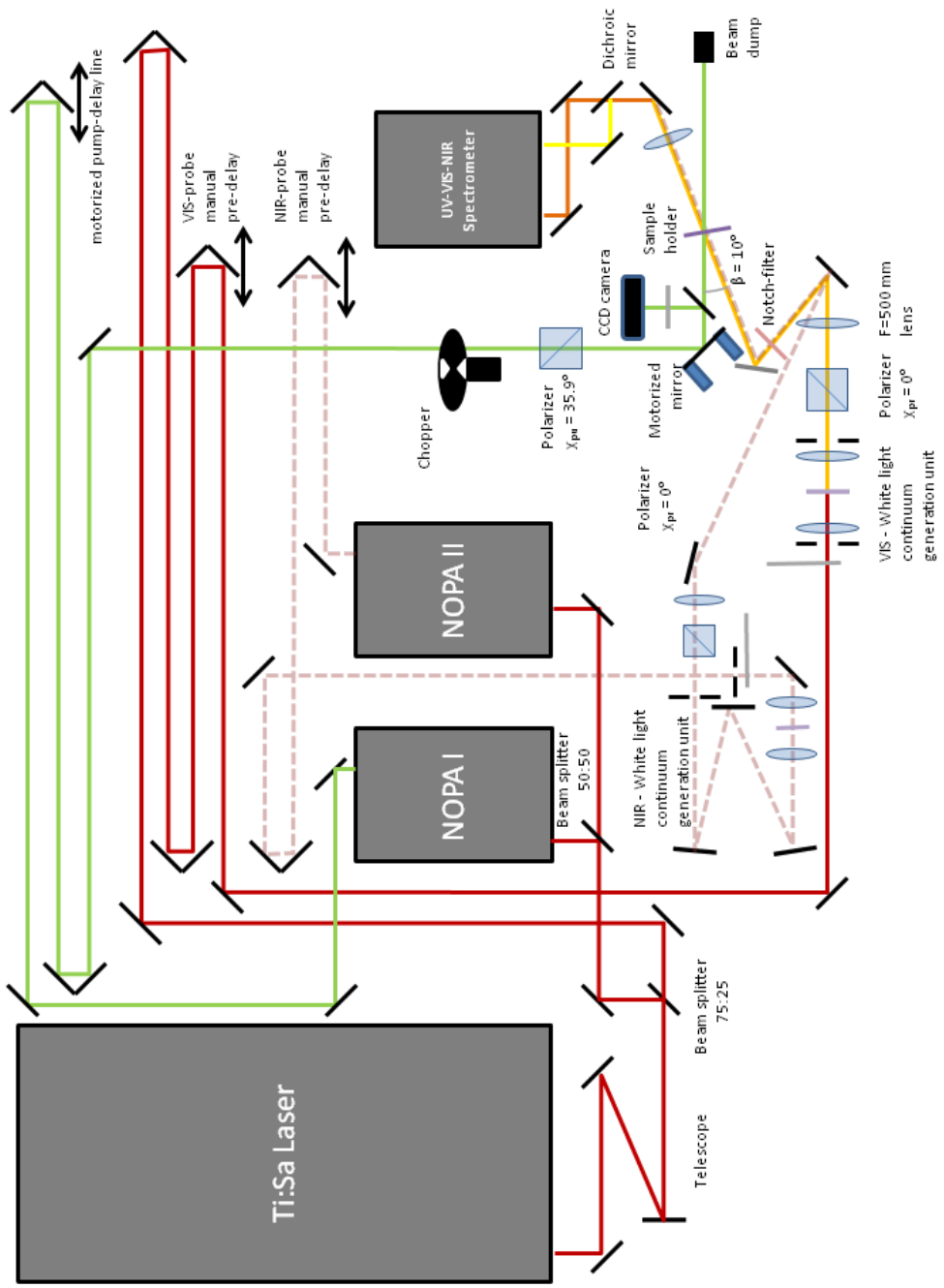

Figure 3.4.: optical path schematic of the TDCF and TAS setup: red lines describe the path of the 800 nm fundamental for VIS white light generation (yellow), pink dashed lines the 1200 nm for NIR white light generation and green for UV-VIS pump. Two manual linear stages are used to match the optimal position of the retro-reflector on the motorized linear delay line. Several mirror pairs, telescopes and periscopes are used to match beam heights and sizes (not in the sketch). The whole setup is covered on all sites with black anodized aluminum plates for laser safety and for minimizing air ventilation/ vibration.

3.3. Time Delayed Collection Field Experiments

In TDCF, the device is excited with a suitable wavelength at a varying pre-bias, followed by a delayed collection field, which should be large and fast enough to extract all remaining charge (Figure 3.3b) [56]. The experiment allows us to scan the field dependence of charge generation at short delays and recombination dynamics at large delays.

Special care must be taken to ensure that only the wavelength needed is generated by the NOPA and hits the sample and that there is no additional non-linear effect (e.g. second harmonic generation (SHG)) in the device or substrate. Therefore the spectral response was measured with a highly sensitive partially home-build UV-NIR spectrometer (electronics by *Entwicklungsbüro Stresing*, optics by *Carl Zeiss Jena*, concept and design by Florian Dornack and Jona Kurpiers) and cross checked with an Andor Solis SR393i-B spectrograph with two peltier cooled detectors: silicon DU420A-BR-DD and an Indium Gallium Arsenide DU491A-1.7.

For excitation of the CT emission maximum a slightly different setup was used, a ns-Nd-YAG Laser (Ekspla) was used instead of the *f*s-Laser (similar to Figure 3.3e) to successfully eliminate non-linear effects which can be induced by high pulse energy density *f*s-pulses (above 100 $\mu J\,cm^{-2}$) in the substrate or active material. To ensure a perfect timing and a low jitter between optical excitation and electrical probe an optical delay line (85 m long quartz fiber, LEONI) delays the light pulse with respect to the trigger diode signal before the fiber [81, 118, 133]. Additionally, for experiments were one wavelength (532 nm) is sufficient, instead of the Ekspla Laser, a ps-Laser (Innolas AOT 1) was used.

The pre- and collection bias was provided by a fast, low jitter function generator (Agilent 81150A, output connected to V_i of the amplifier) which is directly triggered by a delay generator (Coherent SDG) for the *f*s-setup and with a fast trigger diode (EOT-ET2030TTL) for the ns-setup). Special care must be taken to avoid free carrier recombination prior to extraction during a charge generation measurement at short delays. Therefore, mild excitation conditions and also fast ramp-up of the bias is needed. Fast charge extraction needs a small measurement resistor (10 Ohms) and a small capacitance (100 pF) which results in a short and large recharging current of ca. 1 A within 2.7 ns. A high fidelity home-built measurement amplifier was used to apply the pre- and collection bias and measures the

current through the device. The electrodes of the device (Figure 3.1b) are directly attached to the amplifier to reduce induction induced overshoot and ringing. A high definition oscilloscope (Agilent DSO9104H) with very low noise input amplifiers in combination with a home-written software-lock-in-amplifier was used to reach an overall high sensitivity.

For temperature dependent measurements the device was positioned on the cooling finger of a closed cycle helium cryostat (ARS-CS202-X1.AL). Electrical connection was realized through a home-built, direct attached amplifier as close as possible to the device, with the drawback of loosing cooling power and reaching only 180 K. The cryostat was heated and evacuated to 1.3×10^{-7} mbar (Pfeiffer TCP121 Turbo pump and Edwards XDS-10 scroll pump) over night to remove residual water from the vacuum chamber prior to the temperature dependent measurements.

3.4. Home-Built Amplifier

As already noted above, the key component for all field dependent measurements (TDCF, BACE, fd-TAS) is the self-made measurement amplifier which provides a large recharging current of 1 A within 2.7 ns and directly measures the current through an grounded 10 Ω measurement resistor (also 5 Ω or 1 Ω are possible). The same amplifier is also used to drive the quasi cw-laser-diode for BACE experiments.

The collection pulse is provided by an Agilent 81150A function generator, which was selected because of its fast rise time of 2.5 ns, low Jitter of 250 ps and a relatively high driving current of 400 mA for the amplifier input gates. Four fast current feedback operational amplifiers from Texas instruments THS3091 (Figure 3.5, U1-U4) are connected in parallel to provide the required recharging current and amplifying the input voltage from the function generator (V_i) by a factor of four. This factor was chosen due to the fact, that only small signals can be generated with a large bandwidth, *e.g.* fast rise time and low overshoot. Additionally, this operational amplifier family is designed for a gain range from 1 to 10 [134].

The noninverting operational current feedback amplifiers have the input pulse signal connected to its positive input (exemplary only explained for U1 Figure 3.5,

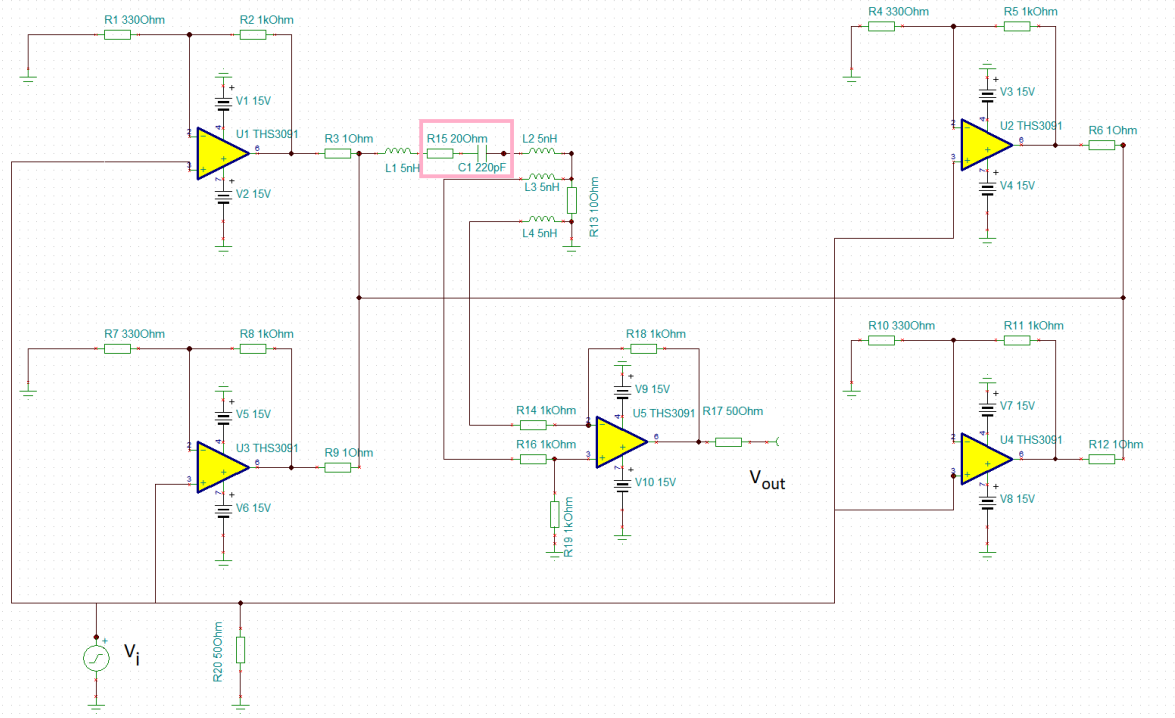

Figure 3.5.: schematic of the self-made amplifier; V_i is the input from the function generator. U1-U4 are the TI-THS3091 operational amplifiers in parallel providing together 1 A for recharging the device under test (pink box), current balancing is realized with an 1 Ω resistor at every single amplifier output, U5 measures the voltage difference across R13, the 10 Ω measurement resistor, U5 is designed as a differential amplifier and line driver (I_d) for ease of use single ended signaling. Connections to and from the amplifier are realized with a matched pair 1 m BNC cables.

here +input), thus the input impedance is infinite. Because an operational amplifier allows no offset between both, the noninverting and the inverting input, the negative input must be at the same voltage as its positive input [135]. This means, that the operational amplifier has to drive current into the external feedback resistor (*e.g.* Figure 3.5, R2) until the negative input is at the input voltage. As a result, the input voltage appears across the grounding resistor (*e.g.* Figure 3.5, R1) if *e.g.* R1 equals R2. The voltage divider rule can be used to calculate the gain, which is the output voltage V_{out} divided by the input voltage V_{in} [135]

$$\frac{V_{out}}{V_{in}} = \frac{R1 + R2}{R1}. \tag{3.1}$$

The gain is only set by the feed back loop of the noninverting operational amplifier design with the two resistors R1 and R2. The feedback resistor R2 can have almost

any value, but R1 should be chosen to get the wanted ratio.

All amplifiers provide their current via a 1 Ohm low inductive resistors into one knot close (5 mm) to the device (Figure 3.5, equivalent circuit in pink square) to reduce cable-inductivity induced overshoot and ringing. The voltage drop across the grounded high-precision 10 Ω measurement resistor is amplified with another THS3091 designed as a differential amplifier with an amplification of one and the output (V_{out}) has a 50 Ω resistor (R17) in series to build a voltage divider at the oscilloscope input (external 50 Ω through-connector). Providing the large recharging current demanded by the operational amplifiers is realized with two grounded small (0.1 μF) and large (6.8 μF) capacitors (not shown in Figure 3.5) which are attached to the power supply rails (V1 - V10) of every operational amplifier on top of each other to save space and improve signal quality.

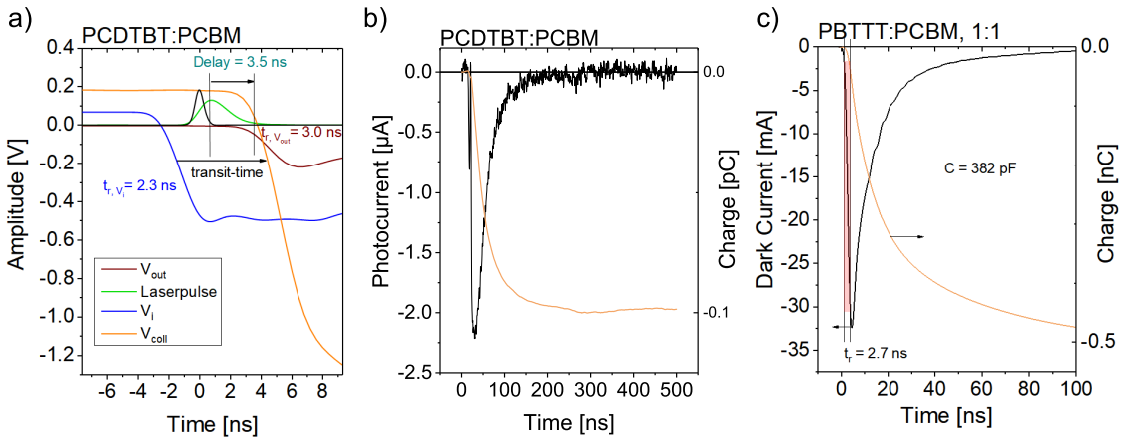

Figure 3.6.: Timings and limits: a) timing of a typical TDCF measurement at short delay; the collection Voltage (V_{coll}, orange) is applied directly after excitation (3.5 ns delay) with a laser pulse (measured pulse in green, calculated pulse in black,). Due to an internal delay (black arrow) in the amplifier circuit, V_i (blue) needs to be applied earlier. All signals are broadened by 600 ps because of the instrument response time plus 100 ps because of the totzeit within the avalanche photo diode. b) Single shot vertical resolution limit for a 70 nm thin PCDTBT:PCBM device excited at 1 nJ/cm^2 equivalent, 8 ns delay, 532 nm excitation wavelength, V_{coll} = -3 V, V_{pre} = 0.1 V. Note that the right axis is in pico-coulomb and the noise level is 30 nA. c) 50 nm thin PBTTT:PCBM blend: RC-time limitation is one of the main drawbacks of TDCF; although the rise time of the dark current transient is pretty fast, it takes roughly 100 ns to apply the full external field across the device (orange line).

Figure 3.6 a shows the timing of a typical TDCF experiment at the shortest possible delay of 3.5 ns when the laser pulse has a duration of 600 ps. The THS3091 operational amplifier has an internal delay of 5 ns, which means that V_{in} for the

operational amplifier has to be applied earlier (Figure 3.6 a, blue) in order have the collection voltage (Figure 3.6 a, orange) applied shortly after illumination. The corresponding current under pulsed illumination is shown in Figure 3.6 a, red. To improve the resolution of the current measurement, the operational amplifiers have to be low in noise and offset, because both will contribute to the integration of the photocurrent transient.

One of the biggest drawbacks of TDCF is the RC-time limitation; every fast physical process taking place within this time is hidden below the RC-time limited extraction. Figure 3.6 c shows such severe limitation for a very thin (50 nm) PBTTT:PCBM device, but its capacitance of 382 pF is already twice as much as a standard capacitance of a well performing organic solar cell. The RC time limits the build up of the voltage across the electrodes of the device. Typical RC times for very thin devices can be more then ∼50 ns. Therefore, the risk of loosing charges because of non-geminate recombination during extraction increases. Still, an uncertainty in timing and charge carrier density determination exists, promoting a careful consideration of the first tens of nanoseconds for very thin devices.

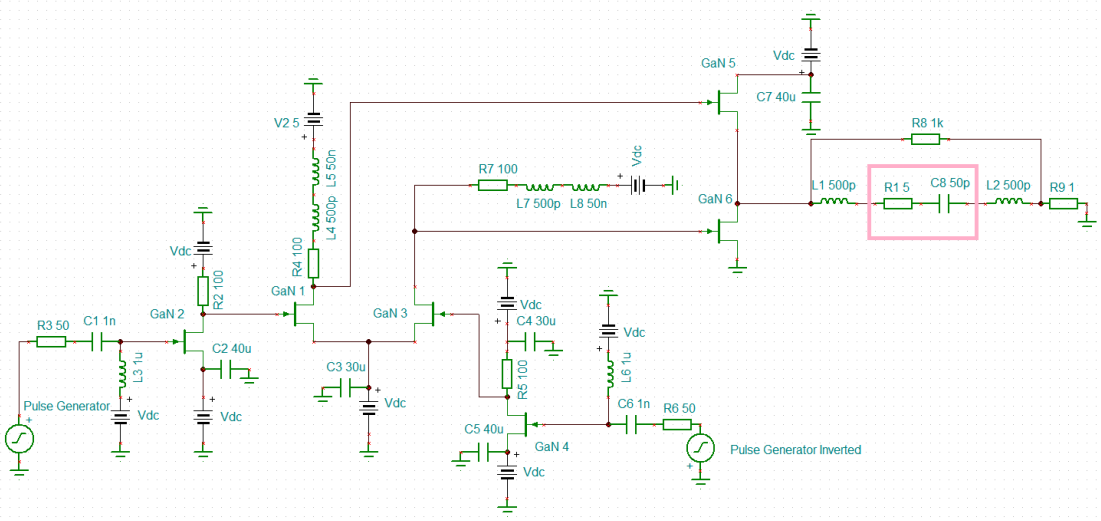

Figure 3.7.: GaN-HEMT ultrafast amplifier: complete circuit diagram using a network of 6 GaN-HEMT Transistors. The device equivalent circuit diagram is placed in the pink box.

Yet, on the basis of earlier experience, the next generation amplifier made on the basis of Gallium Nitride High-Electron-Mobility-Transistors (GaN-HEMT) [136] was developed together with the Ferdinand Braun Institute, which is able to provide 1.5 A within a rise time of 60 ps (DC-30 GHz Bandwidth) and a maximum peak-

to-peak Voltage of 40 V.

The amplifier has an differential signaling input, meaning, that the second input is inverted to the first one biasing the base of GaN 2 and GaN 4 (Figure 3.7), which are building the input transistor amplifiers. Differential instead of single ended signaling is used to apply the voltage pulse and eliminate noise incoupling prior amplification. The collector voltage is arbitrarily set in a way, that there drops enough voltage across R2 to keep the transistor on and in the linear range when it swings positive. When the collector voltage swings negative, still some positive offset across the transistor is needed that it stays linear.

The second stage, a so-called *long-tailed pair* input arrangement gives the amplifier its precision. The transistors GaN 1 and GaN 3 (Figure 3.7) are matched for initial and drift tolerances. Great care was taken in designing the transistors to insure that parameters like current gain and base-emitter voltage are matched between the input transistors, GaN 1 and GaN 3. Since the voltage sources are equal, the current splits equally between the transistors, and thus the output voltages are also equal. As long as the transistors and its parameters are matched, the collector currents are equalized [135]. A small change of one input voltage causes a mismatch in the collector currents and a differential output voltage. When, *e.g.*, temperature changes transistor parameters, it will cause no change in the differential output voltage, as long as the change is equal for both. For a high precision amplifier this behavior is mandatory in order to amplify small input signals while ignoring changes in the ambient conditions [135].

The last stage is the output stage, where an upper (GaN 5) and lower (GaN 6) output transistors is used, which are a complimentary pair. For the upper output transistor, as long as it has a small drain-source resistance it forms a voltage divider together with the sum of the series resistance of the sample and the measurement resistor (R15+R9). When the load resistivity increases or if the output current flow is small, the voltage drop across the output transistor is negligible [135]. Finally, the output current flows through the output transistor. Because, the output stage never should be unloaded, a by-pass resistor, R8, is placed in parallel to the *device under test* (pink box, Figure 3.7).

The measurement resistor, R9, could be as low as 1 Ohm. The solar cell response is measured across this resistor with a differential current probe (Keysight N2793A),

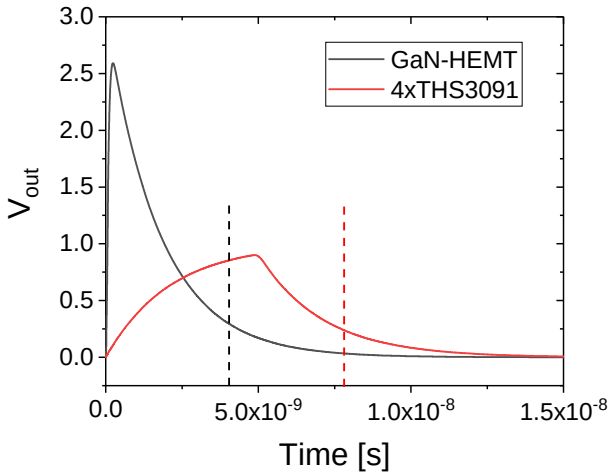

Figure 3.8.: Transient simulations comparing the GaN-HEMT ultrafast amplifier (Figure 3.7) with the 4 times THS3091 design (Figure 3.5) leaving all other components unchanged (device capacitance C=150 pF, measurement resistor $R_m = 10\Omega$, series resistance of the device R_S=7 Ω). Dashed lines are indicating the time when 90 % of the charges are extracted.

which is connected to the oscilloscope. The amplifier circuit is powered by an external 10 channel voltage source. The channels need to be switched on in a specific order defined in the corresponding LabView routine. Simulations with Autodesk EAGLE turned out to show a doubled time resolution (see Figure 3.8) compared to the home-built measurement amplifier with commercially available parts. Unfortunately, up to now, we were not able to prepare a well performing organic solar cell with a capacitance close to 100 pF. This prevents us from exploiting the full scope of the new amplifier system to access the highly interesting sub-ns range.

However, a faster driving circuit does not solve the RC time limitations, but it can speed up the loading process because of the fact, that the capacitive reactance X_C is also a function of the cutoff frequency ω of the driving circuit $X_C = (j\omega C)^{-1}$. The capacitor is loaded faster if the cutoff frequency increases. The rise time t_r becomes a function of ω: $t_r = t'_r(\varsigma)\omega^{-1}$, with t'_r being the scaled, dimensionless rise time at the output of the amplifier and ς being the parasitic functions within the circuit [137].

3.5. Field dependent Transient Absorption Spectroscopy

In the previous section the improvements and limitations of the TDCF setup were discussed. The rise time of the extraction pulse is limited by the RC time, which is depending on the material, in the best case $\sim$ 3 ns is reached. Nevertheless, in organic solar cells many processes happen already on shorter timescales like *e.g.* exciton recombination in the ps range. Also, free charge formation is reported to happen in the fs range [102, 138, 139] for some polymer:fullerene BHJ solar cells. To access and probe processes on this short timescale, Transient Absorption Spectroscopy (TAS) is used (Figure 3.3a and d). TAS is a fully optical pump probe technique which allows us to study the evolution of excitation and recombination of the singlet and CT-excitons as well as of polaron pairs. Note that TAS is sensitive to every charge in the device and not only to those that are extractable. Furthermore, in a typical TAS setup the absorption signals are measured in transmission on thin films, however for organic solar cells the interplay between active layer and electrodes can have a significant influence on processes as *e.g.* recombination and only few people applied TAS on devices with electrodes [52, 54].

To address this issue and to compare TAS data with field dependent TDCF data, the TAS setup was extended by implementing the possibility to apply an external electric field. This allows us to combine and compare external charge generation efficiencies deduced from both setups from the femto- to the millisecond time range.

The setup, which was realized in the course of this work has a time-resolution of 82 fs. Due to a large optical delay line of 1.5 m the full time range between pump and probe spans from of -300 ps to multiples of 9 ns delay. The converted light from the NOPA (green line in Figure 3.4) is guided to the motorized linear stage (OWIS limes 170-1500 & Nanotec SMCI35 stepper motor control). A high precision retro reflector (UBBR-2.5 1S, protected silver, 1 arc second parallelism) is directly attached to the linear stage car to ensure that the reflected light stays at the same position while the car is moving slightly in unavoidable different angles with respect to the table. In parallel the fundamental, which is later used for white light generation, is pre-delayed on a manual linear stage to compensate for different conversion pathways at various wavelengths in the NOPA.

The pre-delay pathway has a total length of 9 m (red line in Figure 3.4) and can be manually varied by 1.2 m, which is needed for the temporal overlap of pump and probe at the beginning of the motorized delay line. The white light continuum (∼400 to ∼1600 nm) used for the probe is generated in an un-doped, 3 mm thick YAG crystal close to the sample holder and can be pumped with 800 nm (VIS-priority) and 1200 nm (NIR-priority). The white light needs to be optimized for the spectral region of interest by slightly moving and tilting the crystal for best conversion efficiency. The 800 nm pumped continuum is filtered with a Calflex X filter which blocks 97% of the fundamental (800 nm) and is focused with a long focal length lens (500 mm) onto the sample, while the pump is ∼20 times larger with respect to the probe beam diameter. Due to air motion on the table and the moving linear stage car, the (chopped) pump spot is also moving on the sample, this movement is actively corrected for with a home-built motorized mirror setup. This setup consists of two nanotec SMCI12 controller and ST2018L0804 motors connected to micrometer screws with a cardan joint, see Figure A.5 and a CCD-camera which monitors the position of the pump beam every second. The home-written software moves the mirror such that the beam at the sample stays at the same position (allowing for 10 μm deviation).

The temporal overlap of pump and probe can be roughly estimated (∼300 ps) with two fast photo diodes (PD1, EOT ET-2030 and PD2, EOT ET-3000, Figure 3.3 d) at the position of the sample and the oscilloscope while the motorized stage is moving. The exact temporal resolution of our setup is measurable with a cross-correlation in a BBO crystal. The ultrashort pulses are too fast for electronic detection. Therefore optical methods are used; our autocorrelator utilizes second harmonic generation (SHG) in nonlinear crystals to measure the time evolution of a pulse. Strong amplification of SHG occurs when two lasers pulses are present in a nonlinear medium at the same time and in the same space. Those two pulses then produce a third pulse of light with the combined pulse energy and at half the wavelength. The setup for a simple autocorrelator is shown in Figure 3.9. The unknown incoming pulse is split into equal portions called the pump and gate. The gate beam is guided through a delay stage before meeting again the pump beam in the BBO. If the distance along the two paths is the same the pulses will overlap temporally and spatially in the crystal to create a signal at double of the incoming photon energy. The emitted SHG signal is detected by a photo diode. Great accuracy in the experimental setup needs to be taken care of, as light travels at a constant velocity, a 0.3 μm change in the path length results in a 10 fs delay

in the time the light pulse arrives at the crystal. By measuring the intensity versus delay stage position it is possible to extract the temporal evolution of the pulse.

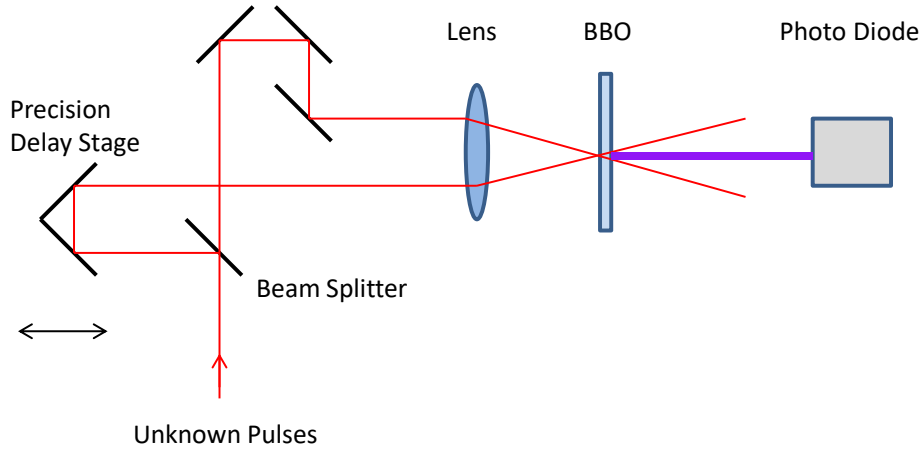

Figure 3.9.: An Autocorrelator utilizing Second Harmonic Generation: The incoming unknown pulse is split into two parts at the beam splitter. The two parts meet again in an BBO and the intensity at the photo diode increases to a maximum if both parts overlap in time and space.

The change of the white light spectrum between a pumped and unpumped sample is recorded with a highly sensitive partially home-built UV-NIR spectrometer. Originally the whole system was bought from m-u-t/tec5 GmbH because the company won the open competitive bidding due to faked specifications. The most prominent mismatch turned out to be the readout rate; m-u-t/tec5 GmbH delivered a system with max. 95 Hz for single pulse triggering, requested was min. 500 Hz. A one year extrajudicial fight against m-u-t/tec5 GmbH ended up in building our own system. The electronics were developed by Entwicklungsbüro Stresing, the optics for the VIS-spectrometer were left unchanged (Carl Zeiss Jena) and NIR-spectrometer was home-built. The concept, design and manufacturing of the compact housing was done by Florian Dornack and myself.

Our spectrometer system is now able to record a VIS and NIR spectrum with a, compared to before, nearly doubled EQE of 92% (80%) in the VIS (NIR) with full 16 bit resolution at a maximum readout rate of 1.4 kHz, improving the signal to noise ratio to the theoretical limit of a typical TAS setup (10^{-5} OD) [140] when accumulating data for 2 s for every delay point. To optimize the sensitivity of the spectrometer system, the probe pulse needs to hit a "sensitive" detector, this condition is met when the pulse arrives $\sim$15 μs before the readout takes place

(XCK level high). The spectrometer electronic is directly triggered by the SDG channel 4 which can be used to delay XCK to the correct position.

Another important point is that the white light needs to be imaged on the detector array, which turned out to be not the case for the Carl-Zeiss-NIR Spectrometer. Due to the fact, that the m-u-t GmbH glued the sensor to the spectrometer no post-optimization was possible. Another disadvantage of the system was the obsolescent NIR-sensor with an overall very low EQE. As a consequence the sensor was removed and replaced with a sensitive Hamamatsu InGaAs G11620-256DA together with the readout electronics by Entwicklungsbüro Stresing. Parts of the spectrometer were removed to clear space for tilt and shift alignment of the new sensor. As a result, the NIR- and VIS-spectrometer sensitivity is comparable to each other when detecting the broad white light spectrum.

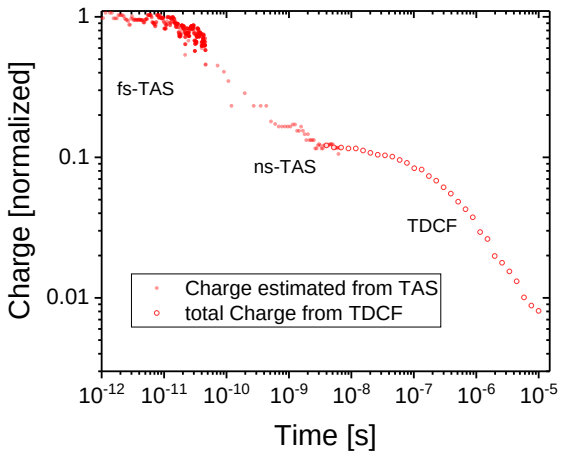

Figure 3.10.: Example of TAS and TDCF measured on the same sample: Loss of photogenerated charges in a PCPDTBT:ICBA blend with electrodes measured with transient absorption spectroscopy in reflection in the femtosecond range (optical delay), in the nanosecond range (electrical delay) and with TDCF in the nanosecond to microsecond range at an excitation wavelength of 532 nm.

The most interesting renewal is, however the possibility to measure TDCF and TAS on exactly the same device with electrodes and an applied field as shown in Figure 3.10. For field dependent TAS measurements the device needs to be measured in reflection. Alternatively, for very thin (transparent) electrodes measurement in transmission mode are feasible as well. In the case of a reflection mode measurement, only the part of the white light beam reflected from the back-electrode needs to be guided through a pinhole, ensuring that the, from the substrate reflected part

of the beam is fully blocked.

3.6. Bias Assisted Charge Extraction

Charge extraction experiments were introduced by Duffy and coworkers [141] but the method suffered from poor time resolution and poor extraction capabilities. As a consequence, Bias Assisted Charge Extraction (BACE)[3] was developed as a comparable experiment to TDCF with two important differences; first, the cw-laser illumination is switched on for 2 ms ensuring a quasi steady state in the device and switched off within 10 ns when the bias assisted charge extraction takes place (see Figure 3.3f). Second, charges are constantly generated and recombining under constant illumination during a pre-bias preferably close to open circuit conditions and extracted with a typical reverse extraction voltage. The capacitive reference experiment in the dark then starts at zero volts and the voltage jump which is applied to extract the charges is the same as under illumination. For illumination various laser diodes were tested and the laser diodes with the fastest switch off time (10 ns at 445 nm with 1 W from Insaneware, 10 *n*s at 635 nm with 0.5 W from Optnext, 10 *n*s at 530 nm with 0.1 W from SONY) were chosen for the experiments. The light is coupled to a fiber (LEONI, multimode, 85 m long) to ensure high homogeneity of the flat-top beam profile. The device is placed in the same sample holder as used for TDCF. JV-curves were recorded at the same voltage settings for the laser diode delivering the same power but with the laser in cw-mode. Results from BACE experiments were first published by Lange *et al.* [142] and Albrecht *et al.* [143].

[3]BACE was originally build up during my research internship in 2011 and was named *white light TDCF* because of the white LEDs as a constant illumination source. All related programs and subprograms have the original name.

Chapter 4

Free Carrier Generation and Recombination in PbS Quantum Dot Solar Cells

Colloidal quantum dots (CQDs) are a promising class of materials for optoelectronic applications due to their well-tunable optical and electronic properties. These devices deliver high currents but have a rather low V_{OC} and fill factor, indicating significant recombination losses. Therefore, this material class serves as an exemplary device under test for the optoelectronic methods introduced in section 3.3 and section 3.6. TDCF and BACE experiments are used to investigate the charge carrier dynamics in PbS solar cells. As an upper limit to the fill factor these devices suffer from field dependent charge generation, although BACE experiments reveal a rather high effective mobility of $2 \cdot 10^{-3}$ cm^2 (Vs)$^{-1}$, meaning that charge extraction is efficient. On the other hand, a rather high steady state non-geminate recombination coefficient of $3 \cdot 10^{-10}$ cm^3 s^{-1}is measured, meaning that nongeminate recombination competes efficiently with extraction.

This chapter is based on: Jona Kurpiers, Daniel M. Balazs, Andreas Paulke, Steve Albrecht, Ilja Lange, Loredana Protesescu, Maksym V. Kovalenko, Maria Antonietta Loi and Dieter Neher, *Appl. Phys. Lett.* **108** 103102, 2016, https://doi.org/10.1063/1.4943379. The paper is reprinted with permission from Applied Physics Letters under the license number 4593560908052. Copyright, 2016 AIP Publishing LCC.

A better and cleaner synthetic processing has largely improved the quality of CQDs, which has stimulated their use in a diversity of applications [144–150]. The quantum confinement in the quantum dots can be tuned via precise tuning of the QDs dimensions. Close proximity of QDs is achieved through the ligand exchange process, by which the original, bulky organic ligands are replaced with shorter ones, enhancing the electronic coupling. Lead chalcogenide quantum dot solids exhibit a very broad absorption range, extending into the near infrared region [151, 152], which makes them attractive for photovoltaic devices [153]. The early Schottky devices suffered from limited open circuit voltage (V_{OC}) and fill factors (FF) [151, 153]. Great improvement in the device structure and in the choice of ligands led to a record PbS CQD solar cell with efficiencies up to 10%. That record device showed a short circuit current of up to 22 mA cm^{-2}, V_{OC} of 0.63 V and FF of 0.7 [154]. Still, the device performance seems to be limited by the V_{OC} and the FF, due to recombination [155, 156]. The nature of traps and the recombination mechanism in CQD solar cells is not yet fully understood.

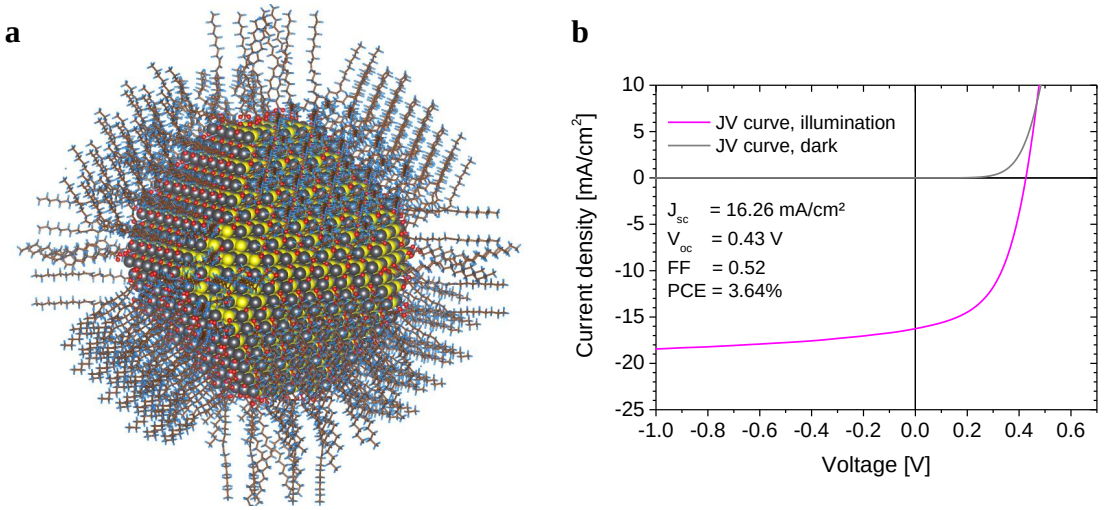

Figure 4.1.: PbS colloidal quantum dots: (a) Calculated atomic structure of a 5-nm-diameter QD passivated with oleic acids (OA– and OH– ligands) adopted with permission from Ref. [157]. These QDs are crosslinked with BDT. (b) JV-curve under 100 mW cm^{-2}, AM1.5G illumination (pink) and in the dark (grey) of a device with 140 nm active layer thickness and an active area of 16 mm^2.

TDCF, BACE and steady state measurements are excellent methods to investigate free charge generation and recombination in PbS CQDs Schottky structure solar cells. Schottky-junction solar cells based on 3.8 nm PbS CQDs were fabricated by Daniel M. Balazs at the University of Groningen. Oleic acid-capped PbS nanocrystals (Figure 4.1 a) were synthetized following a previously published recipe [152,

157]. The active layers were prepared on clean ITO by sequential spin-coating and ligand exchange. A layer of nanocrystals was deposited from a 10 mg/ml chloroform solution. Each layer was exposed to 20 mM acetonitrile solution of benzene-dithiol (BDT) for 30 s, and the liquid was spun dry. The process was repeated 10 times to reach the desired thickness of 140 nm, then the layer was annealed at 140 °C for 10 min. A top electrode consisting LiF/Al was evaporated finishing the fabrication. All the fabrication steps were performed in nitrogen atmosphere and at the end, devices were encapsulated with epoxy resin and a glass lid. The active device area for TDCF and BACE experiments is 1.1 mm^2 and 16 mm^2 for JV-measurements.

The JV-curve and parameters of the device investigated here are shown in Figure 4.1 b. BACE was utilized to measure the carrier density in the devices at V_{OC} under different illumination conditions. A blue 445 nm continuous wave laser diode was used as a light source. To avoid carrier losses due to free carrier recombination, the illumination was switched-off within 10 ns and the external bias was simultaneously switched from V_{OC} to the collection bias V_{coll}.

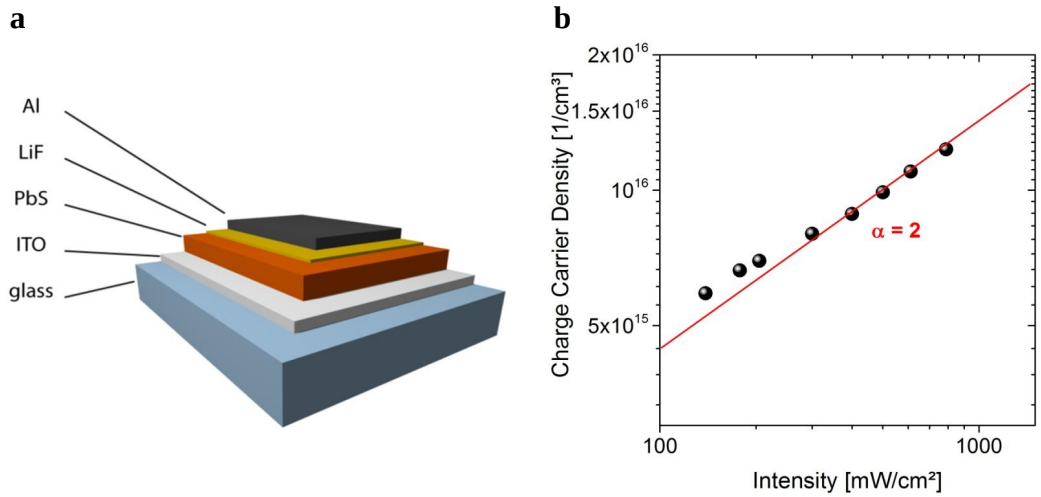

Figure 4.2.: (a) Schematic device structure, the PbS QDs are cross-linked with BDT. (b) Charge carrier density measured with BACE at different illumination intensities at a bias which equals Voc (black circles), with the red line showing the slope for strict bimolecular recombination, with a recombination coefficient $3 \cdot 10^{-10}$ $cm^3\,s^{-1}$.

Figure 4.2 b shows the resulting carrier density as a function of the steady state light intensity. At V_{OC}, the net current in the device is zero, meaning that all photogenerated carriers must recombine. If the generation rate G is proportional to light intensity and independent of field, the extracted charge density n as function of illumination intensity at the respective V_{OC} yields the order of recombination

via:

$$n = \left(\frac{G}{k_\alpha}\right)^{1/\alpha} \tag{4.1}$$

In Figure 4.2 b, data approximate a slope of 1/2 for higher illumination intensities, in accordance with a strict bimolecular recombination process (recombination order $\alpha = 2$) with a density independent free carrier recombination coefficient k_2. At lower illumination intensities, the extracted charge carrier density is expected to deviate from the true average carrier density in the active layer, due to an inhomogeneous charge distribution [158]. Therefore, results for illumination intensities below ca. 1 sun (100 mW cm^{-2}) have been omitted. To determine the absolute value of k_2, the generation rate was estimated from the saturated reverse photocurrent J_{sat}. With $J_{\mathrm{sat}} = 20$ mA cm^{-2} at an illumination intensity of at AM1.5G at 100 mW cm^{-2} a reverse bias of -1.5 V and an active layer thickness d of 140 nm, k_2 amounts to $3 \cdot 10^{-10}$ cm^3 s^{-1}. This value is significantly larger than for most organic donor-acceptor blends, for which k_2 is typically between 10^{-12} and 10^{-11} cm^3 s^{-1} [61, 73, 75, 159–161]. As a consequence of rapid free carrier recombination, the charge density in the device extrapolated to 1 sun illumination intensity is fairly small, around $n = 5 \cdot 10^{15}$ cm^{-3}, while polymer-based bulk heterojunction cells typically exhibit n in excess of 10^{16} cm^{-3}, [143, 159, 162].

At V_{OC} all photogenerated carriers must undergo recombination. Thus, the energy loss from the bandgap to qV_{OC} are due to recombination. This rapid free carrier recombination and the resulting low steady state carrier density at an illumination intensity of one sun is a major reason for the low V_{OC} and underperformance of these cells. Despite that, the devices exhibit a reasonably high FF, meaning that photogenerated charges are rapidly extracted from the active layer. Balazs *et al.* reported impressively high electron mobilities $\sim 10^{-2}$ cm^2 (Vs)$^{-1}$ in colloidal quantum dot solids, but rather low hole mobilities $\sim 10^{-4}$ cm^2 (Vs)$^{-1}$. Both mobilities were measured in a field effect transistor (FET) geometry. FET-mobilities for CQDs with BDT ligands were significantly lower [163], but these values were shown to be strongly affected by interfacial traps between the CQD layer and gate dielectric [163]. Thus mobilities in the FET architecture are not necessarily applicable for understanding solar cell operation. Therefore, BACE was applied to

determine an effective mobility

$$\mu_{\text{eff}} = \frac{2\mu_e\mu_h}{\mu_e + \mu_h} \tag{4.2}$$

within a solar cell at working conditions. In Equation 4.2, μ_e is the electron and μ_h the hole mobility. To determine μ_{eff}, the same carrier density n is obtained in two ways: either by illumination at intensity I_1 and V_{OC} conditions, where the current density is zero or by keeping the device at a lower bias $V < V_{\text{OC}}$, but at higher illumination intensity I_2, with a measurable net-current $J(V)$. With these data, the effective mobility is calculated via [143]:

$$\mu_{\text{eff}}(n, V) = \frac{J(V)d}{2e\ n(V)(V_{OC} - V)}. \tag{4.3}$$

Figure 4.4 a summarizes values for the steady state charge carrier densities at open circuit (open circles), n(V_{OC}), measured with increasing illumination intensity, together with n(V) for a fixed illumination intensity (dark yellow squares) corresponding to the JV-curve (black line) with a short circuit current of 24 mA cm^{-2}. n(V_{OC}) increases exponentially with V_{OC} at increased intensities, as expected [143, 159]. In contrast, n(V) varies more smoothly with bias (dark yellow squares in Figure 4.4 a) and intersects with n(V_{OC}) at the particular V_{OC}. In the working range of this device, μ_{eff}, as derived with Equation 4.3, varies between 1.5-3 $\cdot 10^{-3}$ cm^2 (Vs)$^{-1}$, slightly depending on bias and illumination intensity. For comparison, the mobility of the faster carrier type was estimated from the initial decay of the photocurrent transients (see Figure 4.3 a), which yielded a value of 8 $\cdot 10^{-3}$ cm^2 (Vs)$^{-1}$(Figure 4.3 a, inset). In view of the results by Bisri *et al.* discussed above, we assign this to the motion of electrons. As μ_{eff} is markedly lower than μ_{TDCF} we conclude that the extraction of photogenerated charges out of the active layer is limited by the slow motion of holes.

In addition to issues with charge extraction, the FF can be limited by the field dependence of charge generation. TDCF experiments were performed with excitation wavelengths of 410 and 532 nm, using a delay of only 4.5 ns between pulsed illumination and the onset of charge extraction with an applied V_{coll} of -1.5 V. This delay was chosen to ensure non-geminate recombination had not yet commenced. For these conditions, Figure 4.3 b shows that the bias dependence of the total

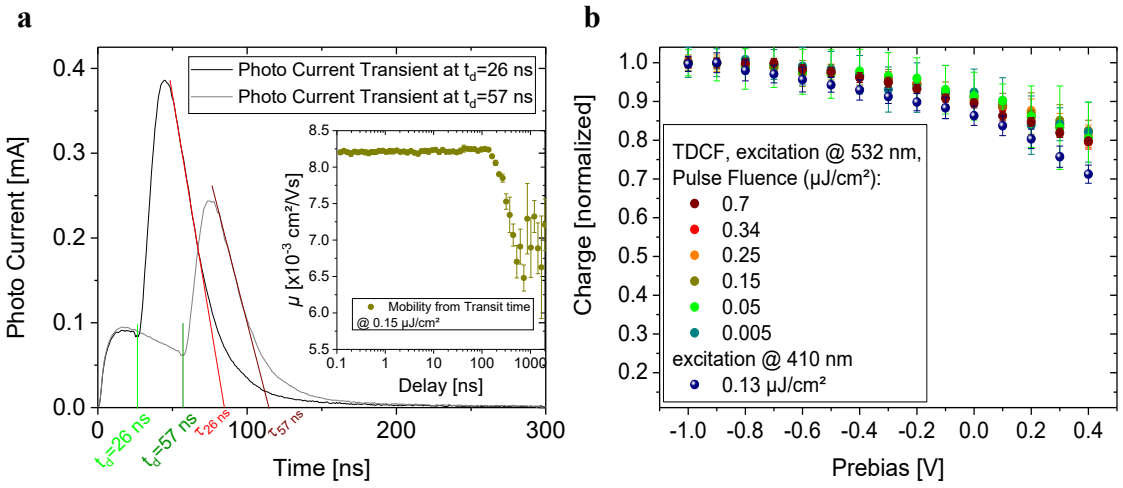

Figure 4.3.: Mobility of the faster charge and field dependent charge generation (a) The faster carrier mobility (inset) calculated from the photocurrent decay of a TDCF transient at V_{coll}=-1.5 V as a function of delay (right) with $\mu\mathrm{TDCF} = \frac{d^2}{(t_{\mathrm{tr}}-2\mathrm{RC})}(V_{\mathrm{OC}}+0.03V-U_{\mathrm{ext}})$, d is the device thickness, t_{tr} the transit time of the remaining photogenerated charges after a certain delay, R is the resistance and C the capacitance of the sample. The pre-bias during delay was V_{pre}=0.3 V. (b) Total extracted charge as a function of pre-bias for different pulse fluences and wavelengths (delay 4.5 ns and 10 ns for excitation at 532 nm and 410 nm respectively, V_{coll}= -1.5 V).

extracted charge is independent of the fluence, meaning that the extracted charge scales strictly linearly over a wide range of fluences (between 0.005 $\mu\mathrm{J\,cm^{-2}}$ and 0.7 $\mu\mathrm{J\,cm^{-2}}$), ruling out any significant losses by higher order processes as the data series overlay at reverse and forward bias. In the following, the generation efficiency (EGE), expressed by the total extractable charge in relation to the number of incident photons, is discussed at a rather low fluence (of only 0.15 $\mu\mathrm{J\,cm^{-2}}$), as this yielded a charge carrier density comparable to steady state conditions under one sun (AM1.5G, 100 $\mathrm{mW\,cm^{-2}}$). Charge generation with excitation wavelength of 532 nm was found to have a slight field dependence, which becomes somewhat stronger if the sample is instead excited with higher photon energies at 410 nm (Figure 4.3). An EGE of 0.5 at short circuit conditions indicates that 50% of the incident photons contribute to the amount of total charge, and that at reverse bias this improves to almost 55% as the stronger electric field suppresses geminate recombination. The field dependent EGE data is overlaid on the steady state JV characteristics in Figure 4.4 b. It becomes clear that when driving the device at reverse bias, the increasing photocurrent can be directly attributed to the improved generation efficiency at these stronger fields, and reduced free carrier recombina-

tion. However, as the device approaches V_{OC} the current becomes more strongly affected by the internal electrical field, which cannot be ascribed entirely to generation, but rather is attributed to free carrier recombination (light area in Figure 4.4 b).

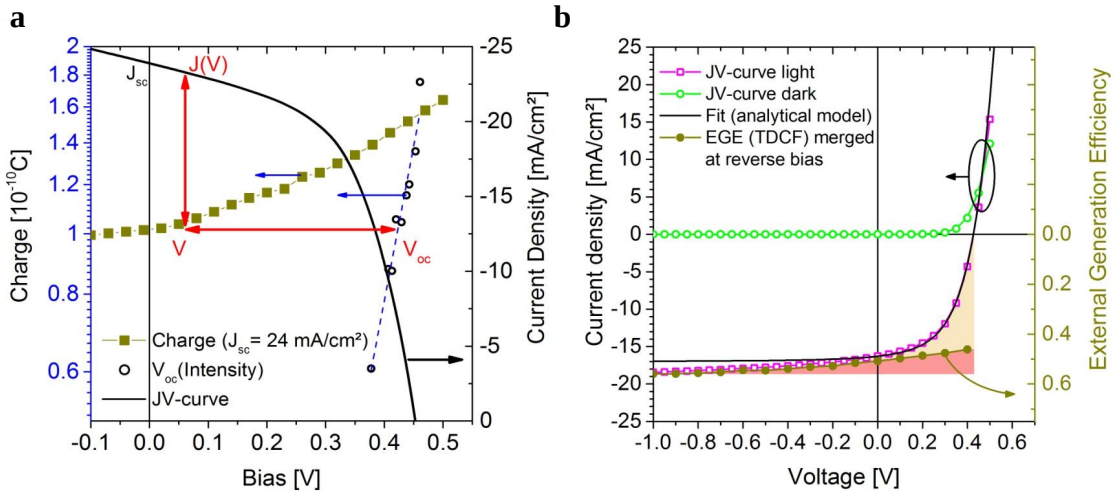

Figure 4.4.: PbS CQD solar cell devices: (a) BACE measurements of the steady state carrier density at different illumination conditions in the operating voltage range. Shown are measurements with increasing intensity at V_{OC} (black circles) and at a fixed intensity (yielding a short circuit current of 24 mA cm^{-2}, dark yellow squares). The corresponding JV-curve is shown by a black solid line. (b) Bias dependent current in the dark (open green circles) and at AM1.5G (pink open squares), compared to the field dependence of free charge generation measured with TDCF (wavelength 532 nm, delay time 4.5 ns, dark yellow circles). The area above the measured EGE shows non-geminate losses and the area below geminate losses. The solid line is the prediction from an analytical model based on experimentally determined parameters.

To check for the consistency of the results, in Figure 4.4 b the experimental JV-curve is compared to an analytical model based on second order recombination, as published recently by U. Würfel and D. Neher [78]. To describe the JV-curve quantitatively by means of an analytical expression, the Shockley equation is often used [76, 86, 164]. Here, the current density J and the external bias V_{ext} are written as functions of the internal voltage V_{int}, where V_{int} is a direct measure of the quasi-Fermi level splitting in the bulk of the photoactive material:

$$J(V_{int}) = J_0 \left(\exp\left(\frac{eV_{int}}{k_B T} \right) - 1 \right) - J_G \tag{4.4}$$

By the time Shockley *et al.* derived Equation 4.4, their devices comprised pn-

junctions made from high mobility materials such as Ge, Si or GaAs. In contrast, organic semiconductors usually display quite low mobilities. Therefore, the internal voltage differs significantly from the applied bias. Assuming a constant tilt of the quasi-Fermi levels for electrons and holes yield:

$$V_{ext}(V_{int}) = V_{int} + \frac{d}{2e\mu_{eff}\exp\left(\frac{eV_{int}}{2k_BT}\right)}J(V_{int}) \tag{4.5}$$

Here, J_G is the generation current, k_B Boltzmann's constant, T the temperature and $J_0 = edk_2n_i^2$ is the saturation current density which depends on e the elementary charge, k_2 the recombination rate and n_i the intrinsic charge carrier density. To calculate $J(V)$, k_2 and μ_{eff} were taken directly from the BACE measurements, n_i was taken from extrapolating the high charge carrier density range measured with BACE to $V_{\text{OC}} = 0$ V (Figure 4.5 a), and J_G was assumed to be equal to the short circuit current.

Note that this approach does not implement field dependent charge generation. Yet, despite the simplicity of the approach, very good agreement between the measured JV-curve and the prediction by the analytical model is seen (black line in Figure 4.4 d), using the measured parameters. The model works particularly well at forward bias, where the JV-curve is mainly governed by non-geminate recombination.

Parameters used for the analytical description of the JV-curve in Figure 4.4 b are: μ_{eff}=2x10^{-3} cm^2 (Vs)$^{-1}$ for the effective mobility, J_G=J_{sc}=17 mA cm^{-2} generation current, d=140 nm thickness, k_2=3x10^{-10} cm^3 s^{-1} bimolecular recombination coefficient and n_i=1.18x10^{12} cm^{-3} intrinsic charge carrier density from Figure 4.5 a. To obtain a good approximation of the intrinsic charge carrier density, the V_{OC} and $n(V_{\text{OC}})$ is measured at different illumination intensities. Figure 4.5 a displays eV_{OC}-E$_g$ versus n and the linear approximation fitted to the higher charge density part prolonged to a situation were V_{OC} equals zero. The obtained charge carrier density is then the intrinsic charge n_i. In Figure 4.5 b the V_{OC} is plotted versus light intensity. This is a simple way to independently determine the order of recombination. In the semilogarithmic presentation in Figure 4.5 b, the slope of the V_{OC}versus ln(I/I$_0$) plot is $2k_BT/\alpha q$, where α is the recombination order and k_BT/q is the thermal voltage. In case of pure bimolecular recombination at high intensities, α is 2, while α is 1 for trap-assisted recombination at low intensities, which is consistent with results on other CQD solar cells [165, 166].

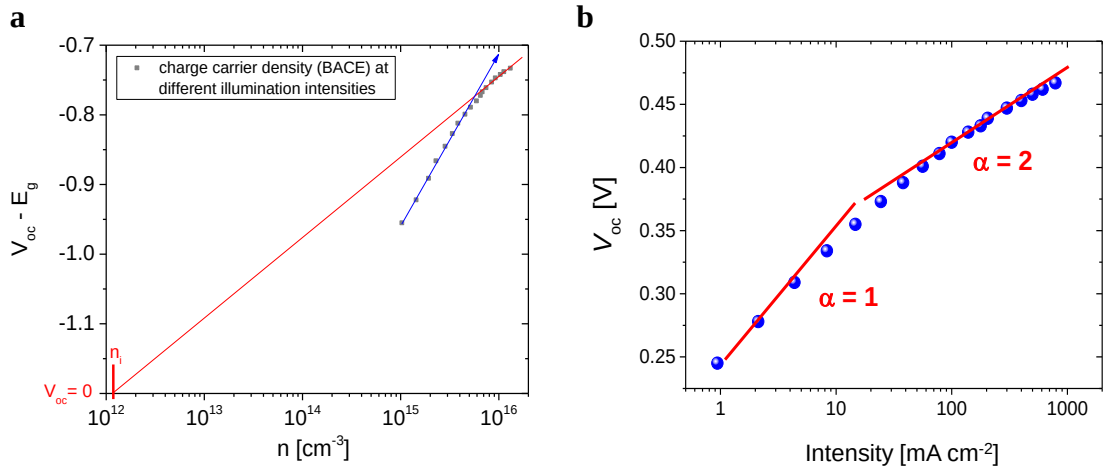

Figure 4.5.: Intrinsic charge and recombination order: (a) charge carrier density measured with BACE at different illumination intensities with their corresponding V_{OC} versus V_{OC} - E_g. Extrapolating the high charge carrier density range to V_{OC}=0 V gives the intrinsic charge carrier density n_i. (b) V_{OC} versus light intensity for a wide range of constant monochromatic (445 nm) illumination intensities, the red line below 0.1 sun corresponds to α=1, primary monomolecular recombination, changing to α=2 above 1 sun (bimolecular recombination).

To give a deeper insight into the recombination dynamics, TDCF was performed with increasing delay time between the excitation laser pulse and the onset of extraction at a pre-bias close to V_{OC}. Figure 4.6 a displays the charge flowing out of the device during pre-bias, Q_{pre}, the charge collected upon application of the collection voltage, Q_{coll}, and the sum, Q_{tot}, plotted as function of delay time for three different fluences. Also, before each series of measurements, the charges present in the dark at the given pre-bias, Q_{dark} were measured with BACE, but with the device kept in the dark. With increasing delay time, Q_{pre} increases continuously, as more and more charge carriers leave the device before the collection bias is applied. On the other hand, Q_{coll} exhibits a continuous decrease, as the charge left in the device after the delay becomes diminished by both extraction and non-geminate recombination. Thus, the decrease of Q_{tot} is only because of non-geminate recombination.

Interestingly, the course of the normalized Q_{tot} as function of the delay is nearly independent of fluence, meaning that non-geminate recombination after pulsed illumination initially does not depend on charge density. This implies recombination follows a recombination order of one as discussed later (Figure 4.6 b, gray lines). This is in clear contrast to the results from steady state BACE outlined above,

which showed non-geminate recombination (NGR) to be bimolecular under steady state illumination conditions above 1 sun illumination intensity (Figure 4.2 a and Figure 4.5 b). It suggests that the initial decay of the photogenerated free carriers in TDCF may involve initially empty traps. Reported trap densities, N_T, in PbS CQD are typically quite high, up to 10^{17} depending on the type and density of the ligand [167].

A closer analysis of the TDCF data reveals that the decay characteristics are inconsistent with a simple first order decay process. To further understand the recombination order and dynamics in this system, an approach was adopted to analyze the non-geminate recombination loss, following the procedure outlined in Ref [168, 169]. The incremental change of Q_{tot} over a time increment, $\Delta Q_{tot}(t)/\Delta t$, is plotted versus Q_{coll}(t) in a log-log fashion. $\Delta\ Q_{\mathrm{tot}}$(t) is the loss due to NGR and Q_{coll}(t) is the charge remaining in the device at time t. Therefore, for any given delay time, the slope of $\log(\Delta Q_{tot}(t)/\Delta t)$ versus $\log(Q_{\mathrm{coll}}(\mathrm{t}))$ yields the recombination order. At short delays, when Q_{coll} is large, the slope of the equitemporal line for the three fluences indeed gives α=1 (Figure 4.6 b, grey line), which indicates a first order recombination process. However, if the system followed a simple recombination process with a time-independent recombination coefficient, meaning that the recombination rate is an exclusive function of the charge density in the device, all points in the differential decay plot would fall on a single curve, which is clearly not the case.

An explanation of both facts is that the non-geminate recombination dynamics up to 100 ns are governed by a first-order process but that the recombination process slows down with time. Although it is not yet clear what the physical processes governing this phenomenon is, one idea is that the initial rapid decay may be due to trapping of the faster carrier while trapping and free carrier recombination of the slower carrier dominates the dynamics at longer times. For even longer delays, all data finally approach one common curve, which now follows strict bimolecular recombination in presence of dark charge, according to:

$$\frac{(Q_{pre}(t+\Delta t)-Q_{pre}(t))+(Q_{coll}(t+\Delta t)-Q_{coll}(t))}{\Delta t}=\frac{\Delta Q_{tot}}{\Delta t} \tag{4.6}$$

$$\frac{\Delta Q_{tot}}{\Delta t}=\frac{1}{eAd}k_2(Q_{coll}^2+2Q_{coll}Q_{dark}). \tag{4.7}$$

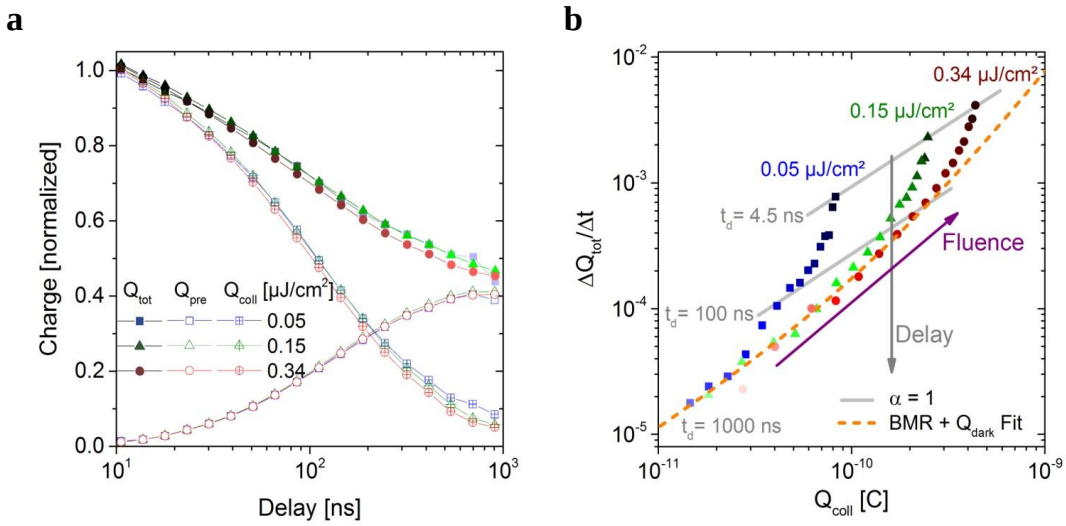

Figure 4.6.: Recombination dynamics: (a) TDCF experiments with increasing delay (until Q_{coll} is not detectable anymore) measured for three different fluencies; 0.05 (green), 0.15 (dark yellow), 0.34 (blue) μJ cm^{-2} at V_{pre}=0.3 V (b) a direct plot of the recombination order, which is two for longer delays (dashed orange line) and one (gray line) for all others. The fit (dashed orange line, equation (5) is done with k_2 = 1.5x10^{-10} cm^3 s^{-1} and Q_{dark}= 8x10^{-11} C.

The dark charge as determined by BACE experiments on the same device in the dark is 8×10^{-11} C. The value for k_2 = 1.5x10^{-10} cm^3 s^{-1} from TDCF is slightly smaller than when determined by BACE. However, this is quite understandable considering the much lower carrier densities present in the device at long delays.

A picture arising from these measurements is that a rather high density of traps exists in the active medium. In the TDCF experiment, these traps are initially empty and become rapidly occupied with photogenerated carriers. This explains the first order initial carrier loss in the TDCF experiment. Under intense steady state illumination these traps are permanently filled. Therefore, recombination at and above 1 sun steady state conditions is second order. Following this line of arguments, recombination at low steady state illumination should become dominated by a first order Shockley-Read-Hall process.

Chapter 5

Dispersive Non-Geminate Recombination in an Amorphous Polymer:Fullerene Blend

Geminate and non-Geminate Recombination of free charge carriers are central limitations to the performance of organic solar cells. Especially for low mobility materials non-geminate recombination is strongly linked to the poor movement of charges and their thermalization in the inhomogeneously broadened density of state distribution. Here, the apparent field dependence of charge generation and dispersive recombination of photogenerated charge is studied in a strongly disordered polymer-fullerene blend.

This chapter is based on: Jona Kurpiers and Dieter Neher, *Scientific Reports* **6** 26832, 2016.
https://doi.org/10.1038/srep26832.

The most organic solar cells consist of at least two semiconducting components. When these components are spincoated from a common solution, upon drying, they form an inter-penetrating, partially phase-separated network, comprising donor- and acceptor rich domains. The presence of the acceptor often affects the order and orientation of the polymer chains [32, 170], in some cases the crystallization of the polymer component is suppressed [46]. It is expected that these amorphous regions in the polymer-fullerene blend exhibit higher energetic and positional disorder than within crystallites.

Neutral excitations such as excitons or charged excitations such as polarons may undergo thermalization for amorphous materials, leading to a time-dependence of their fundamental properties on different timescales like spectral diffusion of excitons [33, 35, 171] or time-dependent charge carrier mobilities [36, 37, 114, 172, 173].

In accordance with this correlation, recent studies on prototypical polymer:fullerene blend devices revealed significant thermalization effects [23, 40, 42–44, 174, 175]. One example is PCDTBT (Poly[N-9'-heptadecanyl-2,7-carbazole-alt-5,5-(4',7'-di-2-thienyl-2',1',3'-benzothiadiazole)]) blended with PCBM ([6,6]-Phenyl-C71-butyric acid methyl ester). The PCDTBT:PCBM blend is nearly amorphous [45, 176, 177] independent of device thickness [46]. TAS measurements by Howard and coworkers revealed a progressive red-shift with time of the photoinduced absorption feature assigned to polarons on the polymer, which was attributed to the thermalization of holes within the amorphous polymer network [23]. The large shift of the TAS signal (nearly 200 meV) and the long thermalization time (up to 100 ns) was seen as an indication for considerable energetic disorder of the polymer HOMO in the amorphous blend.

TAS measurements were repeated recently with our setup as introduced in chapter 3 measuring in reflectance while having applied an external voltage (see example in Figure 5.1 a). The spectral features shown in Figure 5.1 b compare very well to the spectra published by Howard and colleagues in Figure 1.4 a [23]. The red shift with time of the photoinduced absorption feature is well resolved, in Figure 5.1 c the maximum shifts from 2.1 eV at 2 ps to 2 eV at 1 ns, which is in good agreement with [23]. This red shift has only a very weak dependence on the externally applied voltage (Figure 5.1 c and red lines in Figure 5.1 d), which is mainly because of electroabsorption in the blend [54]. Evaluating the spectral range from 725 nm to 775 nm, which corresponds to the signature of free charges in a PCDTBT:PCBM

blend [23], reveals a bias independent decay as shown by the well overlapping blue lines in Figure 5.1 d. This finding indicates, that charge generation in the strongly disordered blend PCDTBT:PCBM must be field independent. Obviously, when TAS is measured in a fully optimized device structure with the electrodes on both sides, the decay of the free charge signature speeds up by approximately 4 ns when compared to a measurement in transmission [23]. Recombination fo free charges sets in at 400 ps (Figure 5.1 d, blue lines)

Interestingly, the combination of TAS with kinetic Monte Carlo simulations suggested significant thermalization of the electrons in PCDTBT:PCBM as well, with an initial strong relaxation within the first 10 picoseconds, followed by a successive decay (Ref. [23] and also shown in Figure 5.1 c, 0.8V) which extends into the microsecond range [23]. Hole and electron mobilities were proposed to be time-dependent, with a more pronounced mobility decay of holes due to larger disorder in the HOMO. It was concluded that polarons are extracted and may recombine while still thermalizing [23, 178]. Note that previous conclusions regarding the initial thermalization of charges in PCDTBT:PCBM blends were based on TAS experiments on freestanding layers, without electrodes and without an external bias applied, which is another reason to perform TAS in reflection on a real device structure. Evidence for carrier relaxation at longer time scales (above 1 μs) came from current extraction by linearly increasing voltage (CELIV) while bulk generation time of flight measurements suggested higher order recombination with a possible time dependent recombination coefficient [48].

In this chapter, the method of time-delayed collection field (TDCF) was employed to follow non-geminate recombination (NGR) in an actual device, at charge carrier densities comparable to those found at 1 sun steady state illumination (AM1.5G, 100 mW cm^{-2}), and biases in the actual working range of a solar cell. It is demonstrated that NGR exhibits a continuous slow-down over several orders in time and that most carriers have recombined or are extracted prior to complete thermalization.

By using a short delay and a low fluence, losses from NGR can be neglected and TDCF directly measures the efficiency of free charge generation. Information on the absolute carrier generation yield can be obtained as a function of electric field by varying the pre-bias or photon energy. This condition is usually met when choosing a delay time of ca. 10-20 ns and pulse fluences below $\sim$ 0.2 μJ cm^{-2}[26, 61, 73, 75, 81, 159, 179, 180].

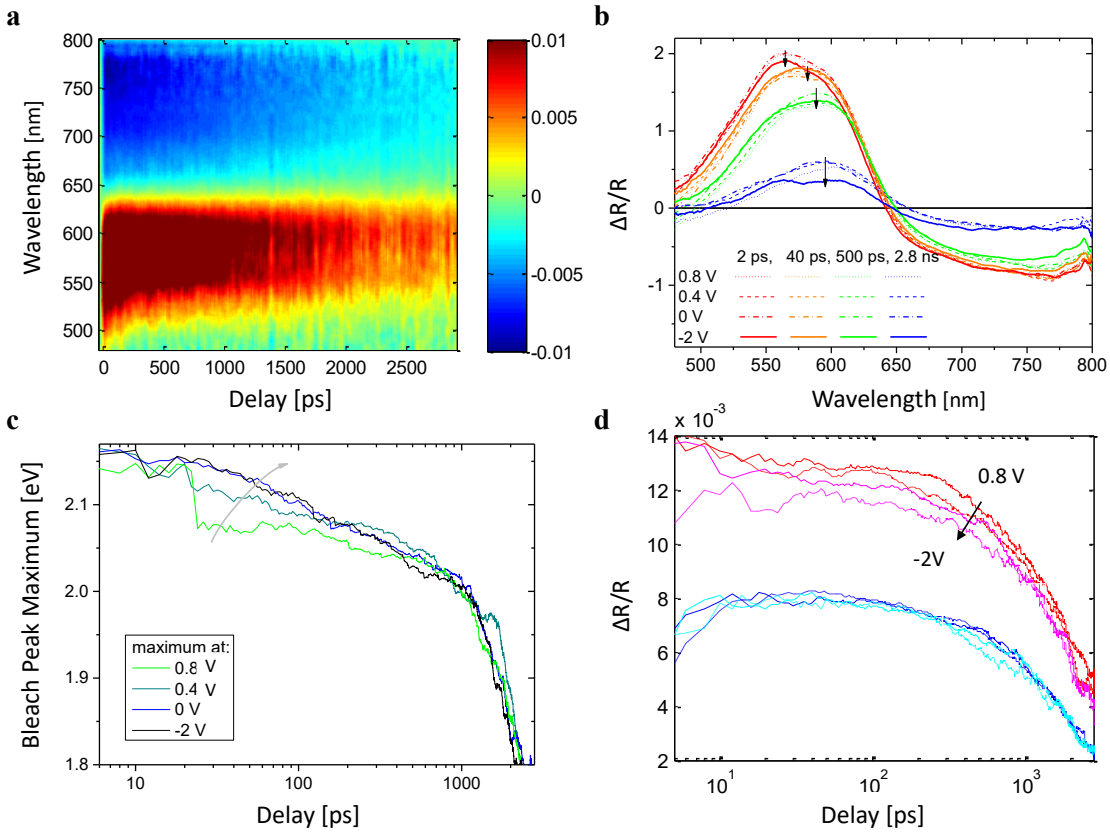

Figure 5.1.: Transient Absorption Spectroscopy in Reflection: (a) Transient reflectivity map recorded after excitation at 400 nm and a fluence of 7 μJ/cm^2 with an applied bias of 0.43 V. (b) Spectra collected after different delay times showing the shift of the bleach peak for different applied biases and (c) its temporal evolution. (d) Line outs showing the influence of the electric field on the bleach peak (red lines) and on the charge density estimated from integrating the polaron peak from 725 to 775 nm (blue lines) for -2 V, 0 V, 0.4 V and 0.8 V.

Surprisingly, when the external generation efficiency (EGE), expressed by the total charge Q_{tot} in relation to the number of incident photons, was measured as a function of pre-bias for the PCDTBT:PCBM blend, an apparent field dependence of generation was observed. This is, however, inconsistent with the high fill factor under steady state one sun illumination (AM1.5G, 100 mW/cm^2), as shown in the comparison between total charge from TDCF and the JV-curve in Figure 5.2a. Additionally, transient absorption measurements with applied biases in the range from -2 V to 0.8 V suggest a field-independent generation of polaron pairs (Figure 5.1d, blue lines). Note that all devices were optimized before the TDCF measurements and exhibited state of the art power conversion efficiencies (PCE), with PCE =

6.8% and 3.9% for an active layer thickness of 70 nm and 220 nm, respectively. These TDCF experiments were performed with the previous TDCF setup with a delay time of 12 ns between photo-excitation and the start of the extraction ramp, and a moderate fluence of ca. 0.1 $\mu J/cm^2$. The apparent field dependence of the EGE in our TDCF experiments, which becomes more pronounced with increased pulse fluence suggests a significant contribution of NGR under the present measurement conditions. If NGR is non-linear in free carrier density, this loss will show up in a sublinear dependence of the total extracted charge on fluence above a certain threshold value. Figure 5.2b shows the result of such a control experiment (red triangles) with a delay time of 12 ns. Interestingly, the charge never scaled linearly with the laser fluence, even for the smallest possible fluence of 0.05 $\mu J/cm^2$. This suggests efficient initial NGR in the PCDTBT:PCBM blend at the time scale of a few nanoseconds.

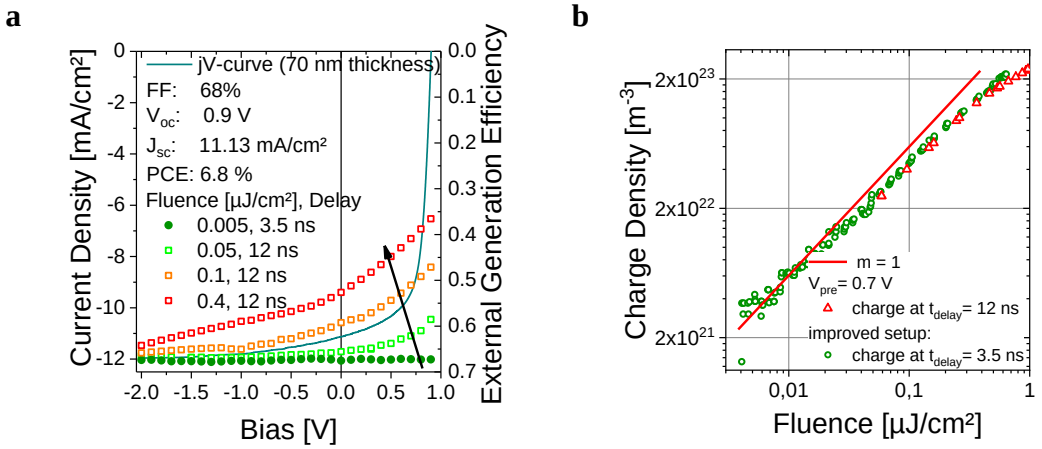

Figure 5.2.: TDCF traces at short delay to probe the apparent field dependence and modified TDCF measurement scheme used to record initial non-geminate recombination losses. (a) The external generation efficiency of a 70 nm thick PCDTBT:PCBM device, measured with TDCF as a function of pre-bias for 3.5 and 12 ns delay time and fluences of 0.005, 0.05, 0.1 and 0.4 $\mu J/cm^2$. Pulsed illumination was at an excitation wavelength of 532 nm with a laser pulse length of 0.6 ns or 6 ns for 3.5 ns and 12 ns delay, respectively. For comparison, the JV-curve of the same device under simulated AM 1.5G light calibrated to 100 mW/cm^2 is shown by a solid line. The scaling of the two y-axes was chosen to overlay the low fluence EGE at a reverse bias of -2 V with the current density at the same bias. (b) The total collected charge density as a function of laser fluence measured with a pre-bias of 0.7 V and a collection bias of -3 V.

Since non-geminate recombination impairs the determination of the free charge generation yield even at the smallest fluence and the shortest delay possible with

our previous TDCF setup [61, 75], significant improvements in the sensitivity and time response of the setup were made. Details can be found in section 3.3. This new setup made TDCF measurements possible with fluences as low as 5 nJ cm^{-2} and with delays of only a few nanoseconds.

With these improvements, full suppression of the initial fast NGR was seen at a very low fluence and at a delay of 3.5 ns. In Figure 5.2b NGR is seen to set in at a fluence of about 0.02 $\mu J\,cm^{-2}$(green circles). TDCF data shown in Figure 5.2a (green circles) prove unambiguously that free charge generation in PCDTBT:PCBM is indeed field-independent if measured under these conditions, consistent with TAS (Figure 5.1 d, blue lines) and other efficient blends [23, 28, 61, 75, 159, 181]. The comparison of Figure 5.2 a and b shows that great care must be taken to choose a suitable fluence and delay time to exclude NGR, otherwise one may make faulty conclusions about the device performance on the basis of TDCF experiments.

Because of the fast response time of the new setup, it is obvious to track dynamics of NGR in more detail. TDCF experiments were performed with different delays and for a wide range of fluences. Special attention was paid to the fact that due to the sample capacitance, the external voltage rise across the device is slower than at the output of the amplifier. Therefore, in addition to classical TDCF experiments, our measurements also included negative delay times, where the collection voltage rise is initiated before the laser pulse hits the sample. Figure 5.3 a discusses these different cases. For a large positive delay, for $t_d >> 0$ (first case), free charges are generated under a certain pre-bias, but undergo significant NGR during the delay before being extracted upon application of the collection bias. When the delay is decreased, (second case) free charge generation still occurs under the pre-bias, but now the collection voltage is initiated shortly after the laser pulse, and non-geminate losses are largely reduced. This is the condition typically chosen to determine the field dependence of charge generation. However, due to the RC-time (τ_{RC}) of the circuit, which is given by the output resistor of the amplifier, measurement resistor, resistivity of the electrodes, capacitance of the sample and cables), a certain fraction of the initially generated charges might still recombine non-geminately before the extraction bias is fully applied across the active layer.

For a small negative delay $t_d < 0$ but $|td| < \tau_{RC}$ (third case in Figure 5.3 a), the initial bias under which charges are generated and extracted is somewhere between pre- and collection-bias. As the internal electric field is not yet fully built up, rapid NGR might still take place. At even larger negative delays (situation 4 in

Figure 5.3 a, $t_d << 0$), charge carrier generation takes place at the fully applied collection-bias. Since NGR is strongly suppressed under the full collection bias, all photo-generated charges are extracted to the electrodes. As shown in Figure 5.2 a (green circles) the EGE to be bias-independent, Q_{tot} for $t_d << 0$ serves as a reference value.

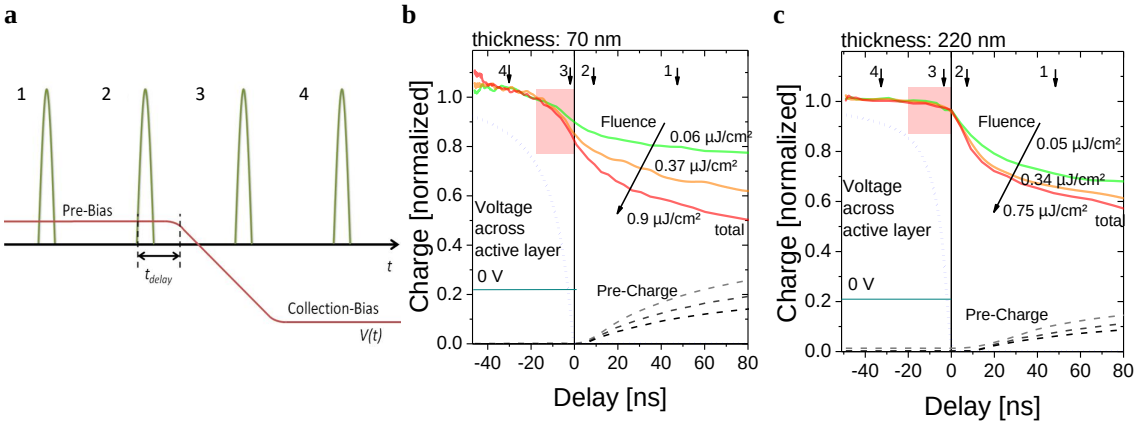

Figure 5.3.: Early time evolution of carrier recombination dynamics for different layer thicknesses. (a) TDCF traces at different delays. Zero delay $t_d = 0$ was defined by the condition that the laser pulse (green line) and the applied extraction voltage ramp (red line) overlay in time at 10% of their final value. (1) $t_d >> 0$, laser pulse (green) under pre-bias, charges are generated well before collection is initiated and will, therefore, experience significant non-geminate recombination. (2) $t_d > 0$, laser pulse under pre-bias but some charges might be lost by fast non-geminate recombination. The example t_{delay} shown in the figure (black arrow) is depicted for this case. (3) $t_d < 0$, laser pulse under increasing collection-bias, but the final bias not achieved; (4) $t_d << 0$, laser pulse under constant collection-bias, geminate and non-geminate recombination is highly reduced. (b-c) The total extracted charge (solid colored lines) and pre-charge (dashed lines) are plotted as a function of delay for different laser fluences including negative delays for 70 nm (b) and 220 nm (c) active layer thickness. The laser pulse width was 600 ps. Data have been normalized to yield the same total charge at a delay time of –35 ns. Also shown is the build-up of the electric field across the device as estimated by integrating the transient recorded in the dark (dotted blue line). The situation where short circuit condition (0 V across the active layer) is reached is indicated by a dark cyan line. Recombination already sets in during the rise of the extraction field for the 70 nm thick sample, but not for a 220 nm active layer thickness. For the thick (thin) device, an active area of 1 mm^2 (0.5 mm^2) was chosen to closely match the RC-time of both devices. The experimental conditions where the same as in Figure 5.2 b, with the pre-bias being close to the maximum power point at 1 sun illumination.

Figure 5.3 b shows results of these measurements for a layer thickness of 70 nm and an active area of 0.5 mm^2. As a consequence of the high capacitance of this

device, because of the small thickness, the RC-time is approximately 12.5 ns and the electric field takes up to 20 ns in order to be fully applied across thin devices (blue dotted line). On the other hand, with an initial pre-bias of 0.7 V and a collection bias of -3 V, short circuit condition (0 V across the sample) is attained already after $\sim$2 ns (Figure 5.3 b, blue dotted and green solid line). According to the JV-curve in Figure 5.2a, short circuit, or applying any negative bias is sufficient to suppress most NGR losses under steady illumination conditions. Therefore, if measured at negative delay, non-geminate recombination should be suppressed.

This is apparently not the case, in the thin device, a significant reduction of total charge is observed even at short negative delay, denoted as a red transparent rectangle in Figure 5.3 b. As free charge generation is independent of field, this loss must be entirely due to NGR. We conclude that for an optimized layer thickness of the PCDTBT:PCBM blend, there is efficient NGR at fast time scales, which already occur during the build-up of the electric field. This rapid and bias-dependent NGR is the reason for the apparent field dependence of the extracted charge carriers in Figure 5.2 a for fluences above 5 nJ cm^{-2}.

When discussing possible reasons for this early-time NGR, it is worth noting that no such effect was seen in the TAS experiments by Howard *et al.* [23] despite using higher fluences. They showed that NGR sets in no faster than 10 ns at a fluence of 7 $\mu J/cm^2$. The two experiments, TAS and TDCF, differ mainly in the fact that while TAS is performed on freestanding thin films in Ref [23], TDCF is measured on the full device structure, with the electrodes on each side of the active material. As already mentioned before, TAS on the full device stack led to the result that recombination sets in earlier (Figure 5.1 d, blue lines). Both experiments reveal, that the rapid NGR is therefore proposed to be mediated by the contacts.

Support for this interpretation stems from numerical drift diffusion simulations. A combined study using Jan Anton Kosters steady state simulation tool Zimtwinkel [182] to determine dark charge carrier profiles and a Matlab routine Listing A.2 which additionally takes into account the competition between extraction, diffusion and recombination at every spatial and time step was applied to support the explanation of TDCF experiments. The results are shown in Figure 5.4. Parameters for the simulation are: μ_e= 10^{-4} $cm^2\,(Vs)^{-1}$, μ_h= 10^{-6} $cm^2\,(Vs)^{-1}$and k_2 = 10^{-17} $cm^3\,s^{-1}$, no trapping, no surface recombination at the contacts, a barrier of 0.8 V for holes and electrons at the anode (right electrode) and cathode (left electrode),

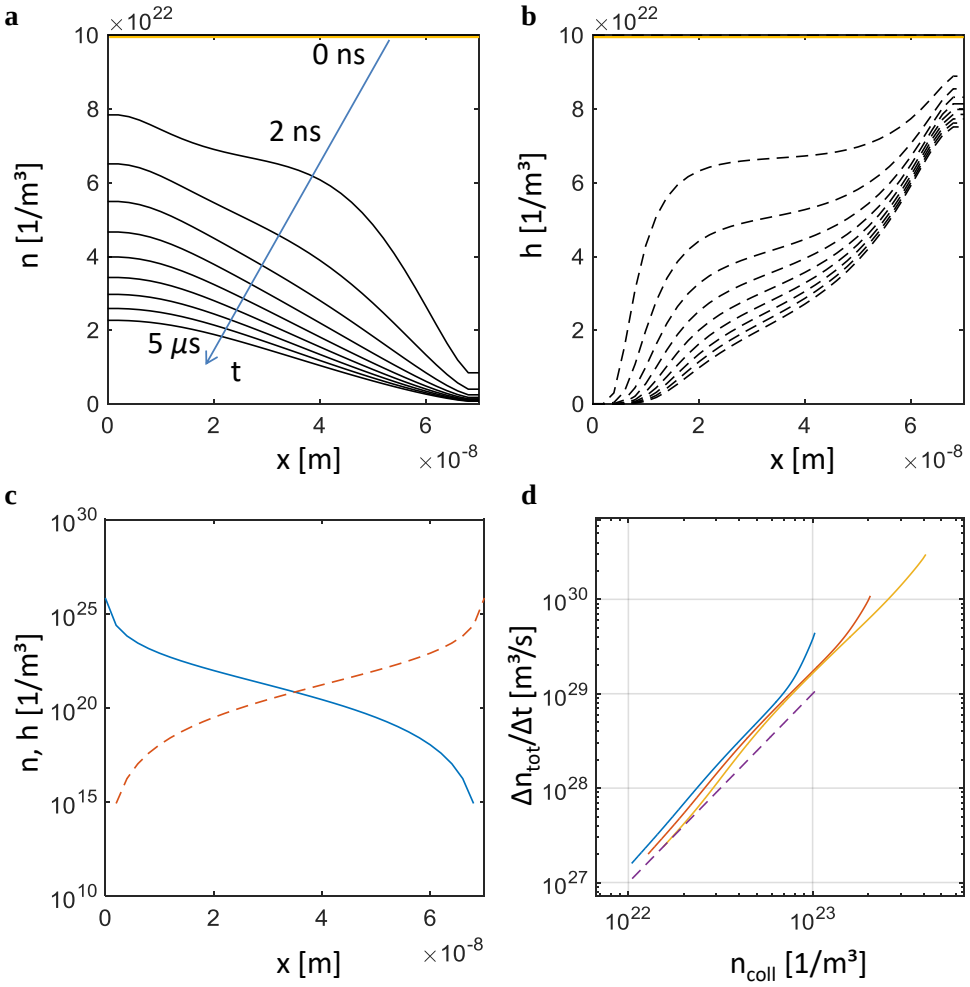

Figure 5.4.: Drift Diffusion Simulation for a d =70 nm thin blend without time dependent parameters. Photogenerated charge carrier density after homogeneous illumination (orange lines in (a) and (b)) in the active layer at 10 different time line outs in the range from 0 ns to 1 mus experiencing bimolecular recombination and extraction under no-flux conditions at the contacts ($\Delta n_e(x = d) = \Delta n_h(x = 0) = 0$) for (a) electrons and (b) holes. (c) Background charge distribution as obtained from simulations of the JV curve in dark with Zimtwinkel introduced in Ref [182] for electrons (blue line) and holes (red dashed lines) (d) Corresponding differential plot of the difference in total charge per time unit versus remaining charge in the active layer derived from (a) and (b) for three different fluences while neglecting time dependent processes ($k_2(t) = const.$). An apparent time-dependent effect is seen in the first 20 ns which exactly monitors contact mediated recombination. The recombination order of one evolves to a strict bimolecular recombination after ∼20 ns. Parameters for the simulation are: μ_e= 10^{-4} cm^2 (Vs)$^{-1}$, μ_h= 10^{-6} cm^2 (Vs)$^{-1}$and $k_2 = 10^{-17}$ cm^3 s^{-1}.

respectively and an optical bandgap of 2 eV. Although no time dependent recombination coefficient was introduced, charges are more rapidly lost within the first

20 ns (upper right part of Figure 5.4 d) than the actual recombination coefficient predicts which was set as input parameter to the simulation ($k_2 = 10^{-17}$ cm^3 s^{-1}, dashed line in Figure 5.4 d). Another interesting outcome is, that for the thin device, 30% of the initially homogeneously photogenerated charge (10^{23} cm^{-3}) are already lost within the first 2 ns, which is in good agreement with TAS measurements (Figure 5.1 d) on a device with the same thickness. The reason for this fast initial loss in the simulation is the large amount of background charges located in the vicinity of the contacts and the low mobilities of the freshly photogenerated charge. The photogenerated charge (0 ns, orange line in Figure 5.4 a) is staying in the device and recombines with the large number of background charges (Figure 5.4 a, black line at 2 ns) before extraction sets in.

Increasing the layer thickness to 220 nm alters the early time recombination dynamics significantly. To better match the RC-time of both devices this sample had a larger active area ($1.1mm^2$), meaning that the capacitance and with that the RC time was only slightly smaller than for the 70 nm sample ($0.5mm^2$). With an active layer being now three times thicker, the initial NGR loss at $t_d < 0$ diminishes because of a smaller contact region to volume fraction. The total charge, recorded as a function of the pre-bias for a short delay time of 3.5 ns is now independent of fluence (see Figure 5.5). An intermediate situation is encountered for an active layer thickness of 150 nm (Figure 5.5, middle). Note that the thickest device exhibited a weak bias-dependence for all fluences which is assigned to a weak field dependence of free charge generation, possibly originating from a slightly different morphology in the thick device [45].

Figure 5.5 b shows that the fast initial recombination loss in the vicinity of the contacts becomes more dominant when the excitation wavelength is changed such, that the generation profile maximum moves from the middle of the active layer closer to the PEDOT:PSS anode (to the near infrared). Increasing the active layer thickness reduces the probability that photo-generated carriers move close to the contact via diffusion, consistent with our finding that thicker devices don't display such an initial decay.

The above data combined with the simulation results provide consistent evidence for a fast initial NGR loss, which is most pronounced for the thinnest device and is most prominent at biases near open circuit. Holes and electrons are generated in the bulk of the active layer, and may diffuse the same direction where they recombine in the region close to the contacts.

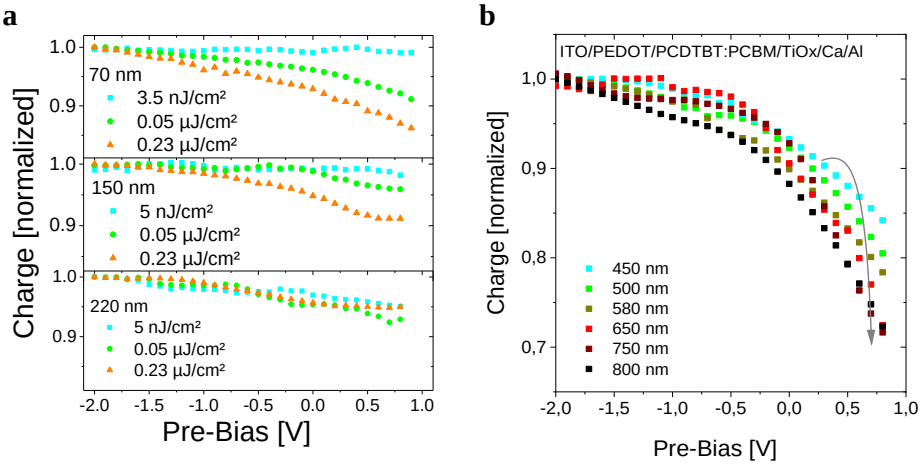

Figure 5.5.: Effect of layer thickness on the initial fast recombination loss. Normalized total charge measured for three different fluences at a delay of 3.5 ns, is plotted as a function of pre-bias for an active layer thicknesses of 70 nm, 150 nm and 220 nm. The decrease in extracted charge with increasing pre-bias becomes less fluence dependent and overall weaker when the active layer thicknesses increases to 220 nm, indicating that the fast initial loss is less significant in thicker active layers. (a) Shown is the normalized total extracted charge for a delay time of 12 ns. Excitation was with different excitation wavelengths, with the fluence adjusted to give approximately the same initial carrier density as for illumination at 532 nm with 0.1 μJ cm^{-2}. The active layer thickness was 70 nm.

Increasing the internal field will speed up charge extraction and reduces the probability for NGR. A comparison of the thin and thick layer of Figure 5.3a and b shows that the charges can be more easily extracted from the thinner device because the pre-charge increases more rapidly with longer delays.

For positive delay times in Figure 5.3 a, b the data show an initial step decrease, followed by a more gradual decay. Attempts to fit these traces with the iterative approach [61, 73, 75], using a constant, time independent recombination coefficient, turned out to not agree with the data. We therefore analyzed the recombination dynamics with a new approach as outlined in Ref [81, 169]. The incremental change of the total extracted charge density per time increment, $\Delta n_{tot}(t)/\Delta t$, with $n_{tot} = Q_{tot}/eAd$, is plotted versus $n_{coll} = Q_{coll}/eAd$ for different delay times and fluences. As $\Delta n_{tot}(t)$ is the nongeminate recombination loss and $n_{coll}(t)$ the remaining charge density at the time t,

$$\frac{n_{tot}(t+\Delta t) - n_{tot}(t)}{\Delta t} = \frac{\Delta n_{tot}}{\Delta t} = -\gamma(t) n_{coll}^{\alpha} \tag{5.1}$$

where α is the order of recombination and $\gamma(t)$, the possibly time-dependent recombination coefficient. According to equation Equation 5.1, the slope of $\Delta n_{tot}(t)/\Delta t$ versus $n_{coll}(t)$, plotted for the same delay but with increasing fluence in a log-log fashion, yields the recombination order. On the other hand, any time dependence of the NGR coefficient will show up as a gradual change of $\Delta n_{tot}(t)/\Delta t$ for a fixed n_{coll} with increasing delay. This general analysis scheme is detailed in Figure 5.6a, where the fluence increases from left to right and the delay increases from the top to the bottom of the graph. Noise in the data was reduced by fitting the original traces with at least three ($s = 3$) stretched-exponential functions

$$f_{\beta_i}(t) = \sum_{i=1}^{s} e^{-t^{\beta_i}}. \tag{5.2}$$

Equation 5.2 is often used as a phenomenological description of relaxation in disordered systems. It was first introduced by Kohlrausch to describe the discharge of a capacitor [183] with glass as dielectric. The resulting differential losses were then binned logarithmically to reduce the number of data points in the differential decay plots.

For all PCDTBT:PCBM blends shown in Figure 5.6, the incremental loss at a given $n_{coll}(t)$ slows down with increasing delay. This points to the NGR coefficient being strongly time dependent. The situation is very different for a well-crystallized thermally annealed P3HT:PCBM sample (see Figure 5.6e, data from [181]), where incremental recombination data for a wide range of fluences and delays lay on the same line, implying a time-independent recombination mechanism at all times studied here. This is in accordance with insignificant spectral relaxation in TAS experiments on P3HT:PCBM blends [100] and the nearly absence of time dependent mobility in the nanosecond range obtained with TREFISH (time resolved electric field induced second harmonic generation) experiments [42]. Therefore, the pronounced slow-down of recombination in the PCDTBT:PCBM sample is attributed to the amorphous nature of this blend.

A comparison of the differential recombination plots in Figure 5.6b and d would suggest that slow-down of recombination proceeds over a longer time scale in the 220 nm sample. Two underlying causes lead to this outcome. First, there is nearly no initial NGR loss for this thicker device, meaning that the differential plot captures nearly all recombination events. Secondly, 6 times the volume, the 220 nm

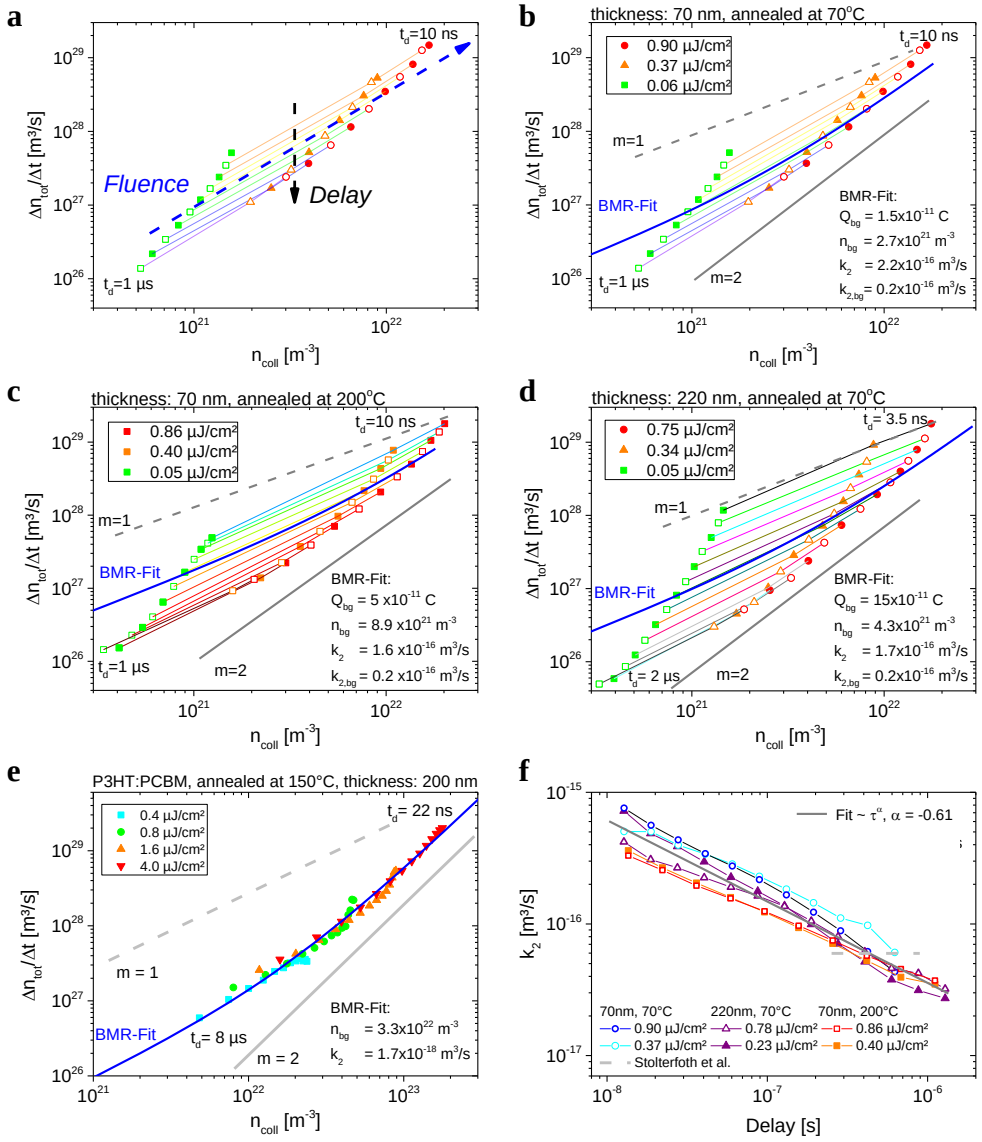

Figure 5.6.: Dispersive Recombination Dynamics in PCDTBT:PCBM. Figures (a)-(e) are differential decay plots showing the charge loss per time unit versus remaining charge in the device for three different fluences. The pre-bias was 0.7 V in all cases. The delay increases from the top (10 ns) to the bottom (1 µs), the fluence increases from left to right. Charge losses for 70 nm devices annealed at b) 70 °C and c) 200 °C, and a device with a d) 220 nm thick active layer annealed at 70 °C. The solid gray line represents a recombination order of 2, the dashed line an order of 1. (e) 200 nm P3HT:PCBM device for four different fluences, data depicted from Ref [181]. (f) The time dependent recombination coefficient in PCDTBT:PCBM nicely follows a power law (grey), which is explained by thermalization of photogenerated carriers in an inhomogeneously broadened DOS. The dashed gray line denotes the recombination coefficient determined from previously measured values of the carrier mobilities and the Langevin reduction factor [184].

devices contains a larger amount of charge than the thinner device, allowing us to follow the recombination dynamics with high precision to longer delay times. In fact, the kinetics of bulk recombination is nearly the same for all three devices.

According to Equation 5.1, the analysis also allows one to determine the time dependence of the recombination order α, which is the slope of the equitemporal lines. Interestingly, this slope always falls in the range between 1 and 2 for all samples. This is because recombination of the photo-generated charge also occurs with the background charge in the active layer (dark injection, unintentional doping or immobile charge on the metal electrodes). In previous analysis of TDCF data, bimolecular recombination with background charge was fitted with a simplified model (Equation 5.3) not taking time dependent effects into account [61, 73, 75, 159, 181]

$$\frac{\Delta n_{tot}}{\Delta t} = k_2(n_{coll}^2 + 2n_{coll}n_{bg}). \tag{5.3}$$

Here, k_2 is the bimolecular recombination coefficient and n_{bg} is the background charge density.

The situation is more complicated for the PCDTBT:PCBM blend, because background charge is fully thermalized while most photogenerated charge is not, meaning background and photogenerated charges may have different recombination coefficients. To cope with this problem it is assumed that the dispersive recombination dynamics is dominated by the thermalization of a single charge carrier. Blends annealed at 70°C and 200°C exhibit almost the same recombination dynamics, despite the fact that annealing significantly broadens the DOS of the HOMO of PCDTBT and negatively affects charge transport [45]. Also transient photocurrent (TPC) measurements as well as Monte Carlo simulations of TAS data consistently revealed much higher electron than hole mobilities [23, 185] across the relevant timescales. Therefore, it is presumed that the motion of electrons dominates the rate of NGR.

The differential decay plots were now analyzed with

$$\frac{\Delta n_{tot}}{\Delta t} = k_2(n_{coll}^2(t) + n_{coll}(t)n_{bg}) + k_{2,bg}n_{bg}n_{coll}(t), \tag{5.4}$$

where recombination of photogenerated electrons is described by a time dependent $k_2(t)$, irrespective of whether the recombination partner is a photogenerated hole or a background charge. Following the same line of arguments, the time-independent recombination coefficient $k_{2,bg}$ is used for the recombination of background electrons with either photogenerated or background holes. To get a reasonable estimate of $k_{2,bg}$, NGR in the 220 nm device was analyzed with Equation 5.3 for the longest delays ($\sim$2 μs) as shown in Figure 5.7a. The density of background charge was determined independently by applying bias assisted charge collection in the dark, using the very same bias conditions as in our TDCF measurements (Figure 5.7 b) [159].

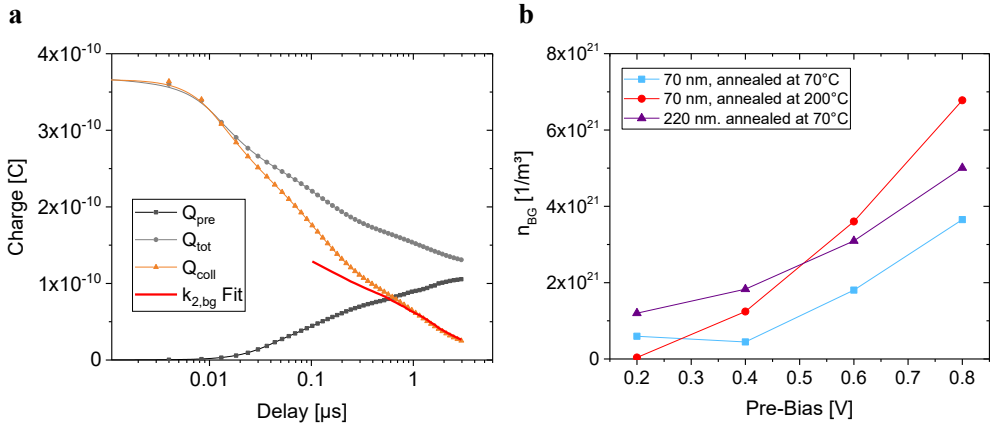

Figure 5.7.: Dispersive Recombination Dynamics in PCDTBT:PCBM. (a) Iterative fit according to Equation 5.3 to the collected charge at delays in the range of 1 to 2 μs yields $k_{2,bg} = 2 \cdot 10^{-17}$. (b) Background charge was measured in the dark with bias assisted charge extraction (BACE) for the devices studied here. The continuous increase in the background charge density with increasing bias indicates that it originates mainly from injection. These values are listed in the corresponding differential decay plots in Figure 5.6.

With this information, the differential plots were fit with Equation 5.4 and $k_2(t)$ as the only variable. Excellent agreement to the data is obtained, as demonstrated with the solid blue lines in Figure 5.6(b-d). Therefore, it is concluded that NGR in PCDTBT:PCBM is strictly bimolecular in nature, but with a time-dependent bimolecular recombination coefficient. The only exception is the early time recombination of the 220 nm thick devices, which follows a first order process. We attribute this to an initial free carrier loss by trapping, in line with the interpretation of transient photocurrent experiments by D. Moses and coworkers [186] in combination with a small loss at the electrodes (see Figure 5.4), which also appears

as an initial first order loss.

The recombination coefficient $k_2(t)$ is plotted for two fluences for all three devices as a function of delay time. It reveals a common power-law-type time dependence of $k_2(t) \propto t^{-\alpha}$, which is assigned to dispersive recombination in the amorphous active layer, as the kinetics of this process are independent of layer thickness (see Figure 5.6f). These particular (power-law) decay kinetics are characteristic for a continuous thermalization of carriers in the inhomogeneously broadened DOS, which progressively slows down carrier motion [40, 47, 174]. The decay proceeds until all charge carriers have either been extracted or recombined, meaning that the carrier distribution in PCDTBT:PCBM never reaches thermal equilibrium. Importantly, the decay dynamics are not affected by the initial carrier concentration. This implies that under all conditions, including the presence of background charge, unoccupied states are always available for the thermalization of photogenerated charge in the tail of the DOS.

Time dependent recombination was not seen in well-ordered samples as studied previously with TDCF [61, 73, 75, 100, 159, 181, 187]. Previous experimental evidence for time dependent NGR dynamics came mostly from all optical pump-probe measurements on freestanding blend layers [17, 19, 188–192], or on complete devices with transient photocurrent methods such as CELIV [193, 194]. Though optical pump-probe techniques exhibit sufficient time resolution to capture the entire NGR dynamics, their limited sensitivity usually requires higher fluences. Because of the contactless sample design for these methods, they are insensitive to the effect of the contacts or an electric field on the recombination dynamics. However, CELIV is capable to work with application-relevant carrier concentrations, but the time resolution is quite poor (above 1 μs).

The dispersive recombination reported here implies a significant slow-down of carrier motion in the time range considered, in agreement to the TAS and simulation data published in Refs [23, 44]. Figure 5.8 compares the Langevin recombination coefficient calculated from the time dependent mobilities in Ref [44] to the time dependent recombination coefficients measured here. This comparison suggests that the recombination coefficient is only slightly reduced compared to Langevin recombination at early times, while it relaxes more quickly than would be expected from hole and electron mobilities alone. As a consequence, the Langevin prefactor falls below 0.1 on longer timescales; consistent with recently published Langevin reduction factors in PCDTBT:PCBM [19, 195].

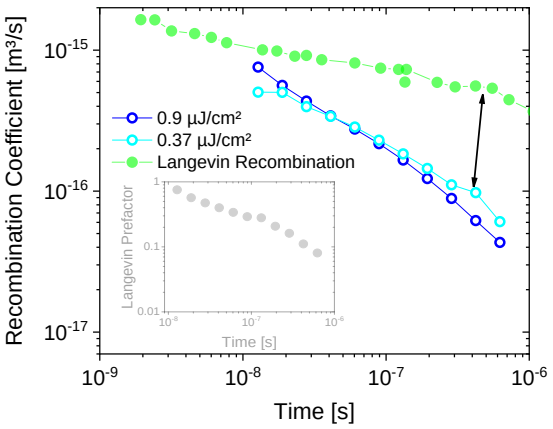

Figure 5.8.: Time dependent Langevin Reduction Factor. Comparison of the Langevin recombination coefficient (green filled circles) calculated from the time dependent mobilities with the time dependent bimolecular recombination coefficients obtained with TDCF experiments (from Figure 5.6 f) for two different fluences. The Langevin pre-factor (Inset) derived from this comparison exhibits a continuous decrease as a function of time, from 0.7 at 10 ns to 0.08 at 1000 ns.

These studies show that non-geminate recombination in PCDTBT:PCBM is bimolecular at all times and intensity studied here. This is in accordance with the findings from a large number of experiments on other organic solar cells, with various methods including transient and steady state techniques [196]. For PCDTBT:PCBM, as free charge generation is field-independent, the only process which determines the field dependence of the solar cell current under illumination is indeed non-geminate recombination, which is shown here to be dispersive and mediated by the contacts.

This study demonstrates the need for a rapid and sensitive measurement of charges in a TDCF experiment. Otherwise, a measurement with poor time resolution and insensitive charge detection due to rapid recombination will result in a virtual field dependence of the generation in a TDCF experiment. Such a result can not fully describe the course of a JV curve.

Chapter 6

Probing the Pathways of Free Charge Generation in Organic Bulk Heterojunction Solar Cells

That organic solar cells perform efficiently despite the low dielectric constant of most photoactive blends initiated a long-standing debate regarding the dominant pathways of free charge formation. In this chapter free charge formation is adressed through the accurate measurement of the activation energy for photogeneration over a wide range of photon energy, using the method of time-delayed collection field at different device temperatures. The most important result of this study is that the activation energy does not depend on the excitation energy. The activation energy is a measure of the additional thermal energy needed to dissociate thermalized CT states into free charge.

This chapter is based on: Jona Kurpiers, Thomas Ferron, Steffen Roland, Marius Jakoby, Tobias Thiede, Frank Jaiser, Steve Albrecht, Silvia Janietz, Brian A. Collins, Ian Howard and Dieter Neher, *Nature Communications* **9**, 2038 (2018) https://doi.org/10.1038/s41467-018-04386-3.

Primary excitations in organic semiconductors are strongly bound singlet-excitons. They split at the D-A interface and form interfacial CT-states. Because of the low dielectric constant in organic semiconductors CT-excitons experience strong Coulomb binding, which is in stark contrast to the field independent charge generation in several well performing devices [6, 61, 118, 179]. A lively debate was born about the nature and energetics of the CT-states involved in free charge formation [11–14, 70, 197, 198].

The aim of the work summarized in this chapter is to contribute to the current debate regarding the dominant pathway of free charge generation in bulk heterojunction solar cells. To this end, we performed precise measurements of the temperature dependent charge generation for a wide range of excitation energies including direct CT excitation. It has been shown that the temperature dependence of free charge generation is very sensitive to the energy landscape involved in the free charge generation pathways [199, 200]. If excess energy would alter this pathway, temperature dependent experiments should show it. Interestingly, this approach has been rarely applied to photovoltaic bulk-heterojunction blends, and before this work has been published, there was no publication which performed a direct measurement of the generation efficiency as a function of temperature over a wide range in excitation energies.

The choice of the material system has some specific requirements: first, the system should have a broad absorption range, allowing for a wide range of excitation energies, from the CT-state to high energy excitons. Second, the system should exhibit an appreciable field dependence of generation, where we also expect a significant effect of temperature on the generation efficiency. Third, the material family should be chosen such that the morphology and performance can be easily controlled by small changes of the chemical structure and the fullerene cluster size should be small enough to not give any own contribution to the field dependence of generation in neat fullerene domains [54]. And last and most importantly, the system should be free of dispersive effects, as shown in the previous chapter 5, this would aggravate the determination of free carrier generation efficiency from the TDCF experiments.

In neat polymers or fullerenes excitation with higher energy photons results in a higher efficiency and a lower activation energy for free charge generation [94, 201]. To confirm these findings we applied TDCF to a sample of the well-known

polymer (poly([N,N-9-bis(2-octyldodecyl)-naphthalene-1,4,5,8-bis(dicarboximide)-2,6-diyl]-alt-5,59-(2,29-bithiophene)) (P(NDI2OD-2T), also known as N2200). This particular polymer was chosen because of its proven bipolar transport characteristics and its low intrinsic disorder [202]. Figure 6.1 shows, that direct excitation of the intramolecular CT state at 800 nm leads to inefficient photogeneration with a much higher activation energy than for the excitation of the π-π^*-transition at 400 nm.

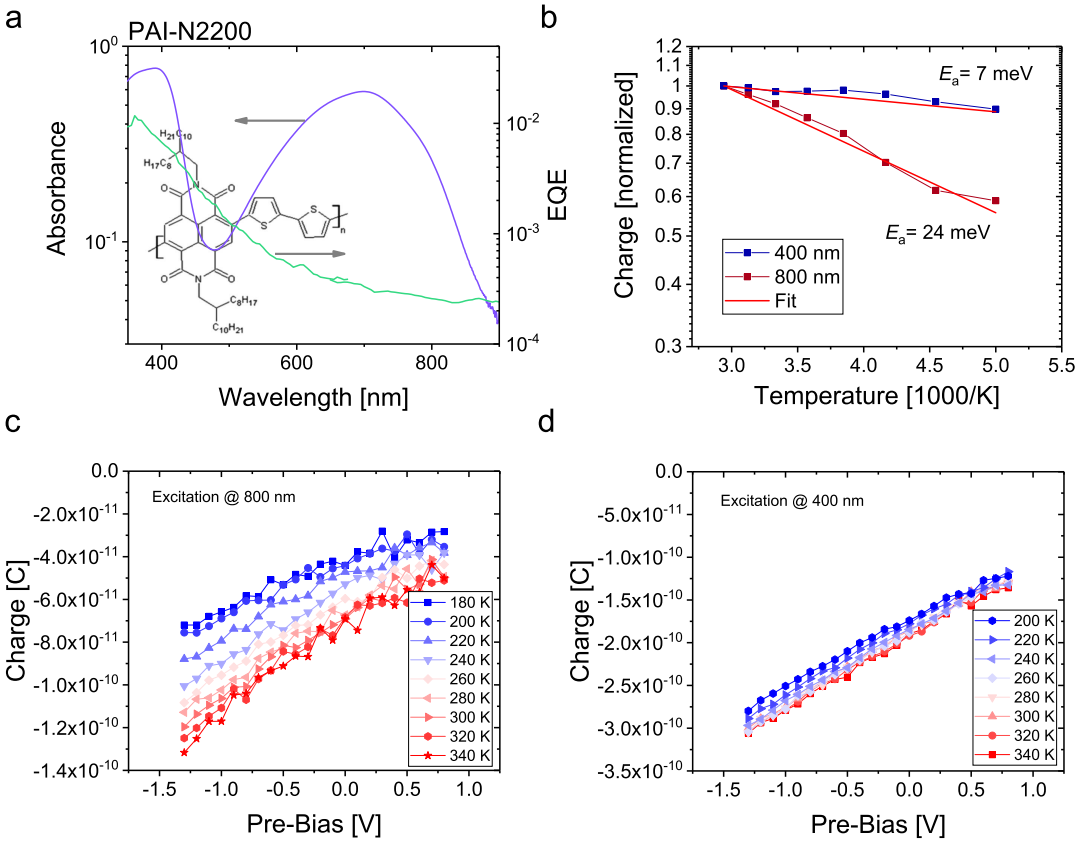

Figure 6.1.: Charge generation in N2200; (a) Absorbance and EQE spectra, the inset shows the material P(NDI2OD-2T) (b) Temperature and field dependent data from c and d at a bias of -1 V reveal activation energies of 7 meV and 24 meV for high and low photon energy excitation, respectively (Fit, red lines). Temperature dependent charge generation at different pre-biases excited at (c) 800 nm and (d) 400 nm.

A huge combination of materials was scanned and finally the PCPDTBT family blended with diffferent fullerenes was found to meet the needs for temperature dependent charge generation experiments. Most of the other blends had issues, e.g. direct charge generation in too large PCBM domains [159], fast initial non-geminate recombination [118], no field dependent charge generation [181] or fluence

dependent field dependence of charge generation and fast initial non-geminate recombination (see Figure A.6).

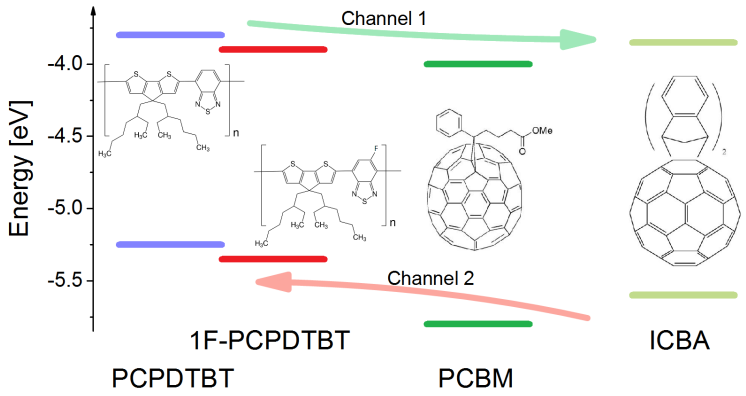

Figure 6.2.: Energy level diagram for the materials used in this study. Arrows indicate the pathways of charge formation via electron (channel 1) or hole transfer (channel 2) across the donor-acceptor heterojunction. The energy offset at the heterojunction is systematically reduced with substituting PCBM by ICBA and PCPDTBT with 1F-PCPDTBT.

The blend energetics, morphology and photovoltaic performance of the PCPDTBT family can be easily tuned by small changes of the chemical structure of the blend materials. By incorporation of a strong electron withdrawing fluorine atom to the backbone of PCPDTBT the energy offset at the heterojunction is reduced. As the energy of the polymer singlet exciton is basically unaffected by fluorination, the lower polymer HOMO will decrease the driving force for charge separation, ΔE_{CS}. The same effect arises when substituting the fullerene PCBM by its derivative ICBA with severe consequences for the photovoltaic performance Figure A.2. Raising the energy of the charge separated state clearly correlates with increase in the open circuit voltage (see Figure A.2), but the correlation between blend energetics and shape of the JV curve is not obvious and requires a better understanding of the blend morphology.

Another crucial point is to exclude fast initial non-geminate recombination over a wide temperature range. Therefore, temperature dependent TDCF experiments as a function of the delay time between excitation and extraction were measured under different conditions and some results are plotted in Figure 6.3.

Figure 6.3 a shows for the example of the PCPDTBT:PCBM blend that charges survive 20 ns without substantial recombination at low fluences, but also that

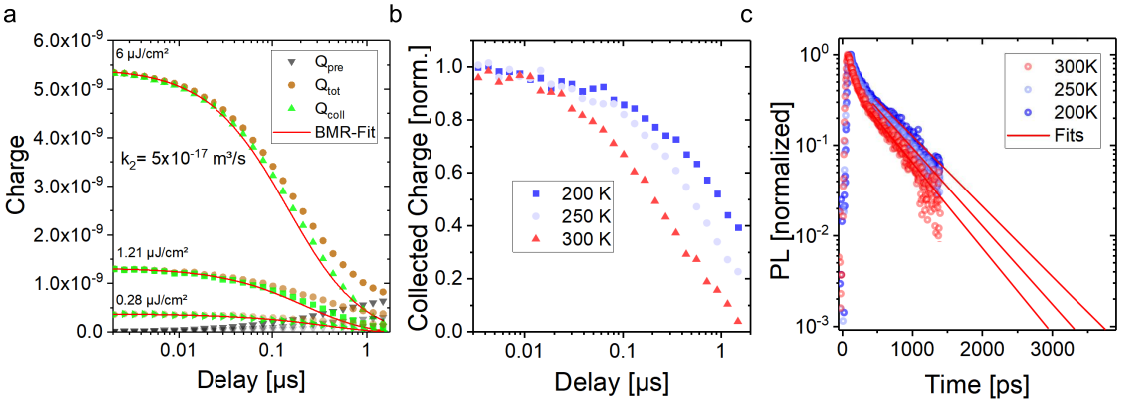

Figure 6.3.: Recombination dynamics for the PCPDTBT:PCBM blend: (a) Shown is the collected charge as a function of the delay time between the laser pulse and the onset of the collection field (green), the charge flowing out during pre-bias (grey) and the total charge (brown) for excitation at 532 nm and three different fluences. The data were fitted (red) with an iterative fit routine specified in [75] with a single $k_2 = 5 \times 10^{-17}\text{m}^3\text{s}^{-1}$ and a dark charge of $Q_{dark} = 1 \times 10^{-10}$ C. (b) Normalized collected charge and corresponding (c) time resolved Photoluminescence evaluated at the CT-emission-maximum for three different temperatures.

the decay follows exactly a second-order recombination process, with the bimolecular recombination coefficient k_2 being independent of the fluence. The absence of an initial decay rules out that dissociable CT states with a lifetime above ca. 4 ns exist in the sample, as such states would contribute to the collected charge at short delays. The lack of dispersive recombination excludes significant early non-geminate recombination. Therefore, the extracted charge at short delay is an accurate measure of the free charge that survived geminate recombination within the first few nanoseconds. Additionally, recombination slows down at low temperatures (Figure 6.3b) extending the recombination onset even further.

TDCF data is supported by the results from transient photoluminescence experiments on a PCPDTBT:PCBM without metal electrodes, shown in Figure Figure 6.3c. The data show that most CT states either undergo recombination or dissociate into free carriers within the first few nanoseconds, even for the lowest considered temperature and zero internal field.

For the studied blends, the group of Brian A. Collins probed polymer crystallinity and fullerene aggregation through grazing incidence wide-angle X-ray scattering (GIWAXS) as well as mesoscale compositional domain structure within each blend with resonant soft X-ray scattering (RSoXS) [26, 203, 204]. Figure 6.4a displays

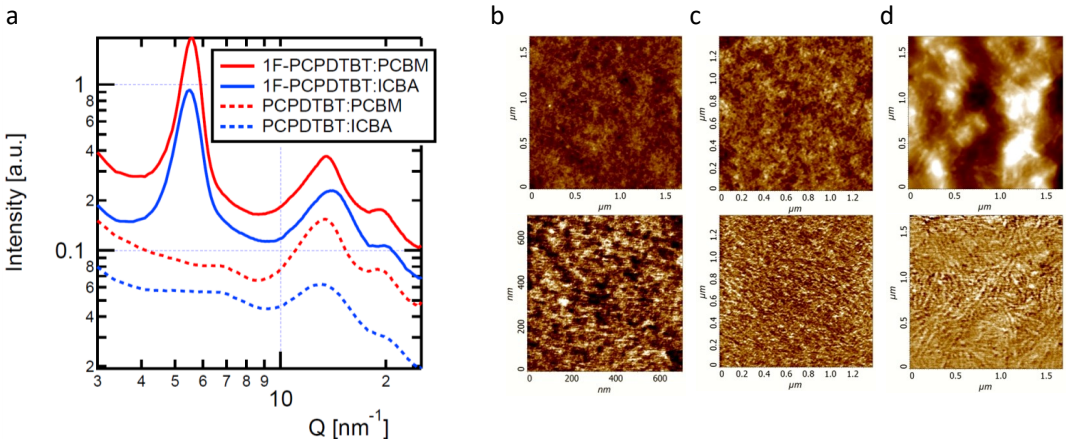

Figure 6.4.: Blend morphology: (a) GIWAXS: Scattering intensity is scaled to allow visual comparison of the lineouts. Peaks at $Q = 5.5\text{nm}^{-1}$ correspond to the polymer (100) plane, whereas the peak at $Q = 15\text{nm}^{-1}$ indicates the presence of fullerene aggregates. (b-d) AFM topology (upper) and phase (lower) pictures of (b) PCPDTBT:PCBM, (c) PCPDTBT:ICBA and (d) 1F-PCPDTBT:PCBM blends measured on a 30x30 µm^2 area in the AFM tapping mode phase images. The PCPDTBT:ICBA blend reveals a rather featureless surface while the fluorinated blend exhibits fiber-like structures which we attribute to polymer aggregates.

the resulting one-dimensional GIWAXS patterns for each blend in the out-of-plane direction of the film. Blends with PCPDTBT lack any indication of lamellar polymer packing, whereas the fluorinated polymer contains a strong peak at $Q = 5.5nm^{-1}$ that indicates polymer aggregation [75, 205]. In all blends, scattering at $Q = 15nm^{-1}$ indicates the presence of fullerene aggregation [26]. A measure of the average distance over which a periodic structure is established, the correlation length, is calculated for each fullerene peak *via* $2\pi/FWHM$ through peak fitting. Blends of PCPDTBT with PCBM and ICBA have correlation lengths of $1.44 \pm 2nm$ and $1.09 \pm 2nm$, respectively, which indicate that PCBM aggregates better than ICBA. Because of the short correlation lengths compared with the molecular size, these numbers should be considered the average distance over which ordering occurs rather than the domain size [206]. Upon fluorination of the polymer, the PCBM correlation length increases to $1.78 \pm 2nm$, indicating even stronger fullerene aggregation caused by stronger polymer packing. The presence of domains in the fluorinated blend can be confirmed by polymer fibrils made visible on the blend surface with atomic force microscopy in Figure 6.4d.

As the morphology is substantially different within the PCPDTBT:fullerene family, the role of excitation energy in free carrier generation might probably depend

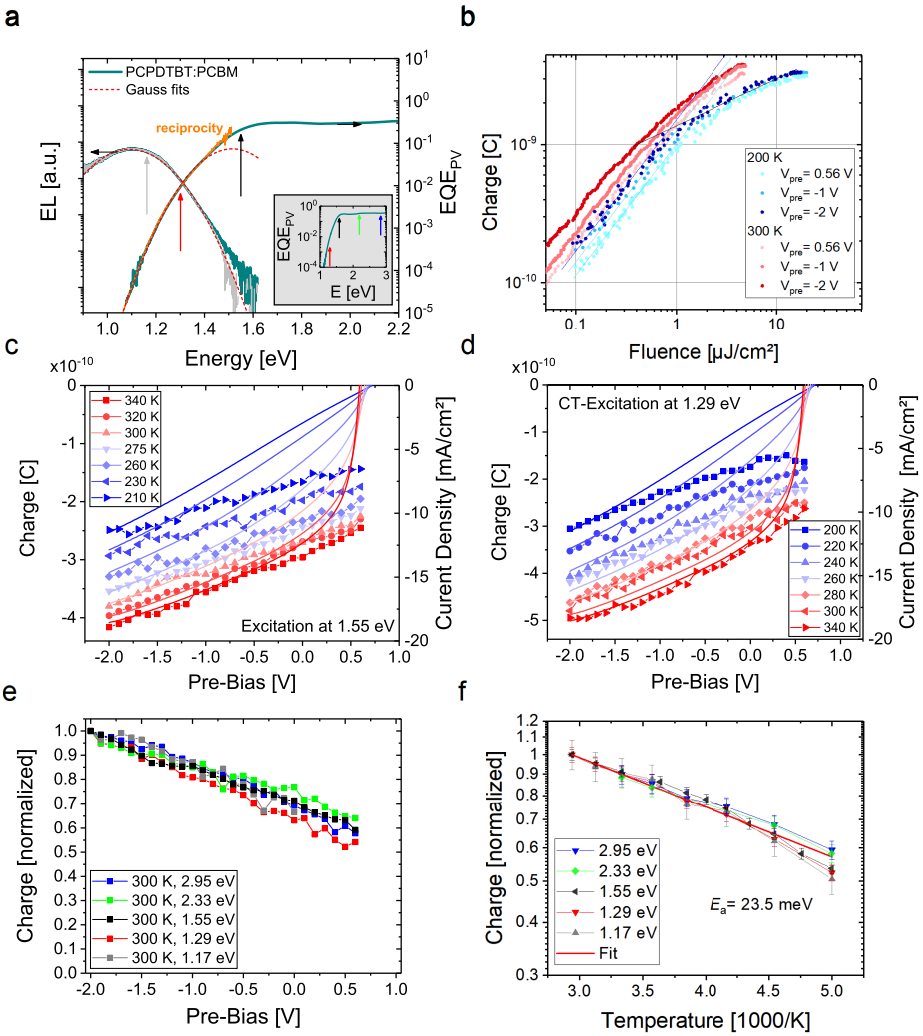

Figure 6.5.: Charge generation in a PCPDTBT:PCBM blend as function of electric field, temperature and excitation energy: (a) EQE of a 110 nm thick blend (cyan, right axis) compared to the EL spectrum measured for an injection current of 0.1 mA/cm^2 (cyan, left axis) at 300 K. Also shown is the EQE calculated from the EL spectrum with Rau's reciprocity relation (dark yellow). Red dashed lines are Gaussian fits to the EL corrected for the EL of the neat polymer. The arrows indicate the excitation energies. (b) Charge at 4 ns delay versus fluence excited at 2.95 eV for 3 different biases measured at 300 K (reddish) and 200 K (bluish). Bias-dependent charge generation (symbols) for different temperatures measured with TDCF for excitation above (c, 1.55 eV) and below (d, 1.29 eV) the band gap of the polymer. The collection voltage was -3 V. Solid lines are JV curves measured under illumination with a halogen lamp adjusted to nearly match AM1.5G. (e) Photogenerated charge normalized to the value at -2 V. (f) Temperature dependent charge generation evaluated in the 0.4-0.7 V plateau region for different excitation energies (see Figure A.4). The solid red line is an Arrhenius-type fit with $E_a = 23.5 \pm 3.4$ meV.

on the morphologically given pathways. PCPDTBT:PCBM blends exhibit a field dependent charge generation of 45% within a bias range from -2 to 1 V, which is perfect to observe a probably changing field dependence with temperature or excitation photon energy. The field dependence of charge generation is stronger for the PCPDTBT:ICBA blend (60% within the same bias range). Up to now, the field dependence of charge generation was mostly probed with TDCF. Only few people applied TAS on a fully optimized device with electrodes [54, 207] although the elucidation of the field-dependence of free charge generation plays an important role. In this work, field dependent transient absorption spectroscopy is applied to an exemplary full device stack as described in chapter 3 in reflection and a small incident angle with respect to the substrate surface. The reflection of the glass substrate is blocked such that only the reflection from the back electrode is guided to the spectrometer. The external voltage is applied with a home built amplifier (section 3.4) and an Agilent 81150A function generator in DC mode. The sample was excited at 520 nm at a fluence of only 0.2 μJ cm^{-2}while held at a bias of 0 V or -2 V (red and gray dots in Figure 6.6).

The last rate equation in Equation 2.28 is relevant for charge collection, which is not the case in Figure 6.6. At these early time scales no charge extraction is possible because of the RC-time being approximately 140 ns for the device measured in Figure 6.6. Therefore, the solid lines in Figure 6.6 b correspond to the sum of the densities in the CT and CS state. After $\sim$1 ns equilibrium is reached and the free charges can be extracted. Interestingly, a field dependent charge generation yield can be observed in combination with a slightly different CT lifetime when comparing the TAS lineouts at 950 nm for -2 V and 0 V in Figure 6.6 b.

Time delayed collection field is, as explained already in the introduction, limited in time resolution by the voltage rise time across the active layer. A voltage where non-geminate recombination is suppressed (0 V) is reached 4 ns after pulsed illumination in the case of a 110 nm thick PCPDTBT:ICBA device. This time is well within the plateau region in Figure 6.6 b. If the pre-bias, at which charges are generated in the TDCF experiment is decreased from 0 V to -2 V, the total charge increases by 48% (see inset in Figure 6.6 b) which compares very well to the increase of the equilibrium levels from 12 % at 0 V to 23 % at -2 V obtained with TAS, 77 % of the total charge is already geminately lost on early time scales. This result proves that TDCF can be used to measure the field dependence of charge generation for the selected material family.

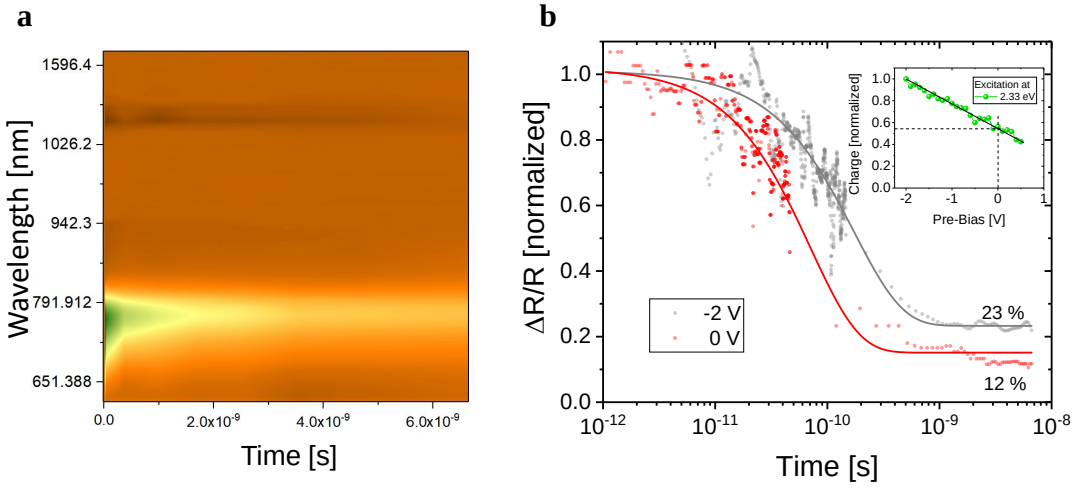

Figure 6.6.: Field dependent dissociation of the CT-exciton: (a) Exemplary transient absorption false colour plot for a PCPDTBT:ICBA blend excited at 520 nm (0.2 μJ cm^{-2}) while hold at short circuit (at a Bias of 0 V) (b) Lineouts at 950 nm (CT-exciton) for a reverse bias of -2 V (gray dots) and 0 V (red dots). Solid lines are rate equation fits according to Armin *et al.* [55] on the basis of the Braun-Onsager model. The rate equation solver source code and corresponding rates for reproducing the fits is shown in Listing A.1. The Inset shows the normalized extracted Charge from TDCF after 4 ns delay at different pre-biases.

To find out appropriate excitation energies, external quantum efficiencies and electroluminescence spectra are fitted with gaussian line shapes yielding a lowest energy excited CT_1 energy of 1.3 eV [208]. Illuminating the sample near the EL-maximum at 1.165 eV will excite the vibronically relaxed CT_1-state, at 1.55 eV the lowest energy polymer S_1-state, at 2.33 and 2.95 eV higher energy excitons on the polymer and fullerene (see also Figure 2.3). The laser fluence was adjusted such that the charge carrier density yield is comparable to AM1.5G illumination at 300 K and increases linearly in fluence within the measurement range at all temperatures (Figure 6.5b). A set of laser line and band pass filters was used to ensure selectivity.

TDCF data collected at different bias and temperatures in Figure 6.5 are compared to the bias-dependent current under 1 sun equivalent illumination performed with a halogen lamp and adjusted for an intensity to match the same short circuit current as at room temperature and AM1.5G illumination. At room temperature the current-voltage characteristics follow the field-dependent TDCF data, except for voltages near $V_{OC}$where non-geminate recombination sets in, which is in agreement with previously published TDCF data on a different PCPDTBT batch [73]. At low

temperatures, transport issues affect the JV curve in the forward bias range more severly than the TDCF generation data, while they merge at reverse bias.

To allow for an easy comparison of the behavior of the different blends, the following analysis considers only two parameters: first, the field dependence of generation at different excitation energies in Figure 6.5 e, second, Figure 6.5 f, the temperature dependence in the low field plateau region (where field-induced barrier lowering is insignificant) [209–211]. These are the cases in which hot generation pathways would be easily detectable. Increasing the bias from -2 V to V_{OC} in Figure 6.5e decreases the efficiency of charge generation by nearly 50%. The temperature dependence follows an Arrhenius-type behavior with an activation energy of 23.5 ± 3.4 meV in Figure 6.5 f. Neither the field- nor the temperature dependence are influenced by the excitation energy, even though this is varied from more than 0.3 eV below to 1.5 eV above the optical bandgap. Excitation of the CT-emission-maximum at 1.17 eV was done with a pulse width of 3.8 ns to exclude nonlinear processes *e.g.* two photon absorption at high fluences. High fluences were needed to measure the field dependence of charge generation at comparable charge carrier densities in the device as for the other photon excitation energies. The pulse width for the other photon energies was $\sim$50 fs. These findings demonstrate that the majority of free carrier generation does not occur *via* 'hot' states in this blend. A proof of this reading is the direct excitation near the CT emission maximum, where only very little extra excitation energy is provided. There is only a small reduction in generation efficiency with decreasing temperature for small excitation energies at low temperatures. This might indicate weak contributions from 'hot' CT states, but may also be caused by a certain narrowing (or shift) of the CT onset at low temperature. However, we expect the narrowing to be negligible compared to the reduction of the whole EQE at low temperatures [208].

Figure 6.5 a shows that the EQE in the sub-bandgap spectral range can be calculated from the EL spectrum with Rau's reciprocity relation [212]. This suggests that the measured EQE spectrum involves the same thermalized states as their recombination as measured with EL [26, 213]. This finding is in contrast with earlier work by Nuzzo and coworkers [30]. Nuzzo *et al.* measured EQE spectra at room temperature as function of bias. The result revealed a stronger dependence of the photogeneration efficiency on bias below an excitation energy of ca. 1.5 eV. This study [30] differs from ours in the way how the photogeneration efficiency was measured (steady-state EQE vs. TDCF), and in the used polymer batch and in the

final device efficiency (2% vs. 3% here), rendering a direct comparison difficult.

Replacing PCPDTBT with its fluorinated derivative or the acceptor fullerene PCBM with ICBA increases the energy of the charge separated state in a similar way but affects very differently the morphology (Figure 6.4). Figure 6.7a, b compare the EQE and EL spectra of the 1F-PCPDTBT:PCBM and PCPDTBT:ICBA blends. Lowering the donor HOMO level (1F-PCPDTBT vs. PCPDTBT) or the acceptor LUMO energy (ICBA vs. PCBM) increases the CT energy and consequently shifts both the EL emission maximum and the EQE onset to higher energies. We also notice the appearance of a weak shoulder at the high energy site of the EL emission of the fluorinated PCPDTBT blended with PCBM. This can be assigned to the singlet exciton emission on well-aggregated polymer chains, which was subtracted from the EL of the blend to yield the EL-CT-emission only. By contrast, the EL of the blend of PCPDTBT with PCBM is broad, homogeneous, and independent of applied bias (Figure A.1), indicating that it originates from CT emission only. Figure 6.7c and d show temperature-dependent charge generation data for below and above-bandgap excitation energies for the 1F-PCPDTBT:PCBM and PCPDTBT:ICBA blend, respectively. Here, the total extracted charge is plotted versus the inverse temperature to apply the Arrhenius-type-fits. Because of the blue-shifted EQE profiles of the two samples, it was not possible to obtain a reasonable set of TDCF data when exciting at 1064 nm (1.17 eV), which was the strongest available nanosecond laser source. But measurements with femtosecond excitation allowed to retrieve a complete set of temperature- and bias dependent TDCF data on the PCPDTBT:ICBA blend with excitation at 1.3 eV, which is exactly at the CT emission maximum (see Figure 6.7 a, b). , Importantly for the primary consideration regarding the role of excess energy in charge separation, we observe that the excitation energy has no appreciable effect on the field nor temperature dependence of free carrier generation despite the very different morphology of the two blends. This is supported by the fact that both blends follow Rau's reciprocity [212] throughout the entire sub-bandgap region, indicating that charge generation from CT excitation below the bandgap proceeds through the same state manifold as the charge recombination that leads to EL.

Both blends exhibit an Arrhenius-type temperature dependence, but the activation energy for the more disordered PCPDTBT:ICBA blend ($44 \pm 3meV$) is significantly higher than for the much better ordered 1F-PCPDTBT:PCBM blend ($19.5 \pm 2.0meV$). This suggests that the activation energy for CT separation does

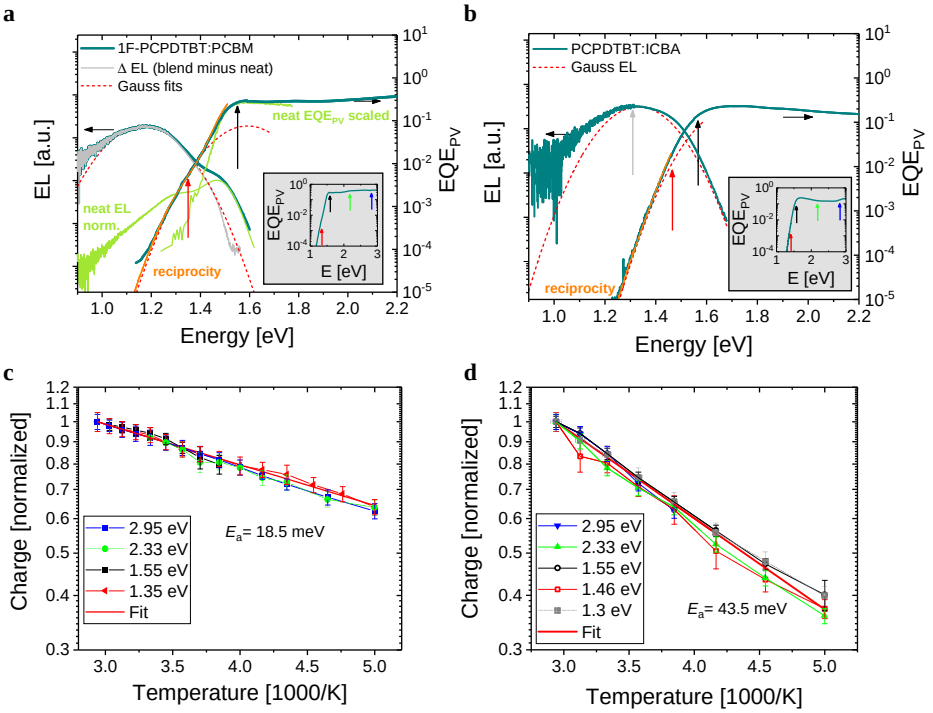

Figure 6.7.: Charge generation as function of temperature and excitation energy: EL and EQE spectra of (a) the fluorinated 1F-PCPDTBT blended with PCBM and (b) the non-fluorinated PCPDTBT blended with ICBA. Also shown are the EQE and EL spectra of neat 1F-PCPDTBT, which are assigned to the polymer singlet exciton (light-green line). The gray insets show the blend EL corrected for the polymer emission. Red dashed lines show Gaussian fits to the low energy emission and EQE, revealing CT energies of 1.38 eV (1F-PCPDTBT:PCBM) and 1.52 eV (PCPDTBT:ICBA). Temperature dependence of the photogenerated charges in the low field plateau region for excitation below, at, and well above the polymer bandgap are shown for (c) 1F-PCPDTBT:PCBM and (d) PCPDTBT:ICBA.

not simply depend on the energetic structure of the heterojunction, but also on the mesoscale morphology with spatial disorder increasing the activation energy.

Discussion

The data reveal that the excitation energy has a small to negligible effect on how field and temperature impact free charge generation: direct excitation of the low energy CT states leads to virtually the same field and temperature dependence as excitation far above the band gap. From this it is concluded that free charge generation does not benefit from the excess energy provided to the system via excitation into higher lying states. This conclusion is valid irrespective of variation in the

CT and activation energies when PCPDTBT is replaced with 1F-PCPDTBT or PCBM with ICBA, which moves the CT state closer to the energy of the relaxed singlet exciton on the polymer. Charge generation proceeds through a common state located at an energy below that of the polymer singlet state, the thermalized CT manifold. Also, our PL and EL data suggest that this very same state manifold yields most of the CT photoemission, meaning that the dissociation of such low energy CT states competes directly with its geminate recombination. As such, the efficiency of CT dissociation, and the mechanism by which electric field and temperature boosts this process depends on the details of the energetic and mesoscale morphological landscape at the heterojunction.

Several papers suggested a two-pool model, where photoexcitation either forms less-bound "dissociable" [14] or strongly bound "localized" [214] CT states, the latter kind yielding most of the monomolecular recombination [215]. To check whether such a two pool situation also exists in our blends, the emission properties of the PCPDTBT-based devices were investigated. The blend of PCPDTBT:ICBA is particularly well suited because: first, it exhibits the most pronounced effect of field and temperature on charge generation. Second, its CT emission is at short enough wavelengths to allow for accurate measurements with the sensitive Silicon detector, and third, it is highly intermixed (see also Figure 6.4). Previous studies suggested that such highly intermixed blends exhibit the largest fraction of localized CT states [100–102]. The inset of Figure 6.8b shows steady state PL spectra of a PCPDTBT:ICBA device measured at different voltages, compared to the EL spectrum of the same devices driven at 1.2 V. Importantly, the PL and EL spectra differ only little, with a slight blue shift of the PL. The small blue shift might indicate non-complete thermalization of excitations in PL. Also, despite a pronounced effect of bias on the emission intensity, the shape and maximum position of the PL is basically unaffected by the applied voltage. These results lead to the conclusion that only one state manifold governs PL and that this is essentially identical to the one being responsible for the EL.

This means, that reciprocity is important here, electroluminescence and charge generation proceeds via the same pool of states. There is no separate pool of bound CT states lying lower or higher in energy which radiates PL but is essentially unconnected to the manifold of charge separated states. To support this conclusion, we made use of the fact that TDCF provides an accurate measurement of the field dependence of generation, also at internal electric fields close to zero. If charges

are generated by field-induced dissociation of the same pool of CT-excitons that emits in PL (Figure 6.8a), the quenching of the PL and the increase in the free carrier generation yield could be related through the following relation [216]:

$$PLQE(V) = \frac{\eta_{diss}(V) - \eta_{diss}(V_0)}{1 - \eta_{diss}(V_0)}. \tag{6.1}$$

$$PLQE(V) = 1 - \frac{PL(V)}{PL(V_0)} \tag{6.2}$$

$PLQE(V)$ is the fluorescence quenching efficiency at a bias V with regard to an arbitrary reference voltage V_0, with $PL(V)$ being the bias dependent PL intensity:

$$PL(V) = \frac{A * k_r}{k_d(V) + k_r + k_{nr}} < 1, \tag{6.3}$$

and $\eta_{diss}(V)$ is the bias-dependent CT-dissociation-efficiency

$$\eta_{diss}(V) = \frac{k_d(V)}{k_d(V) + k_r + k_{nr}} < 1. \tag{6.4}$$

Here A is an unknown prefactor, k_r the radiative-, k_{nr} the non-radiative-recombination- and $k_d$the dissociation rate of the CT state, with only k_d being voltage dependent. To proof mathematically, that Equation 6.2 is given by Equation 6.1, Equation 6.1 needs to be rewritten:

$$PLQE(V) = \eta_{diss}(V) - \eta_{diss}(V_0)(1 - PLQE(V)). \tag{6.5}$$

Equation 6.4, Equation 6.1 and Equation 6.5 lead to:

$$PLQE(V) = \frac{k_d(V)}{k_d(V) + k_r + k_{nr}} - \frac{k_d(V_0)}{k_d(V_0) + k_r + k_{nr}} \frac{PL(V)}{PL(V_0)}. \tag{6.6}$$

Resorting and with Equation 6.3, Equation 6.6 can be rewritten as:

$$1 - \frac{k_d(V_0) + k_r + k_{nr}}{k_d(V) + k_r + k_{nr}} = 1 - \frac{PL(V)}{PL(V_0)} \tag{6.7}$$

which is the $PLQE(V)$ as defined in Equation 6.2.

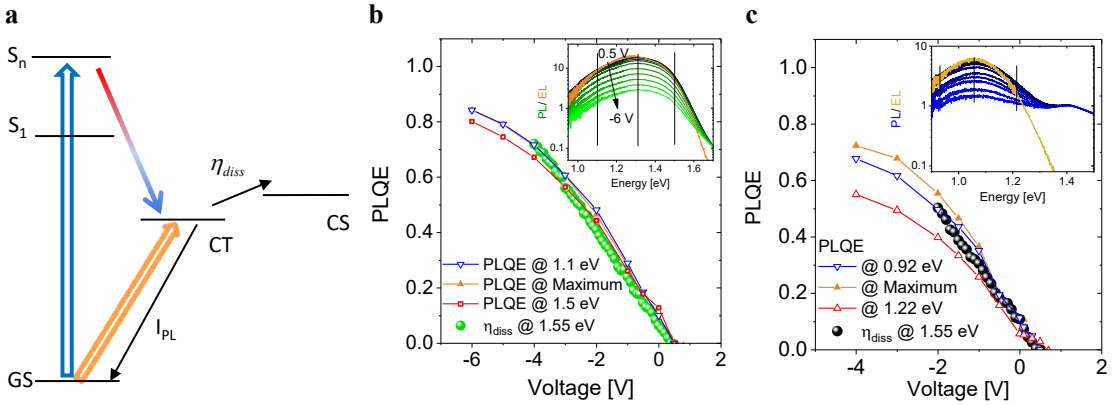

Figure 6.8.: Bias-dependent photoluminescence: (a) Energy scheme describing the competition between the recombination of the occupied CT state manifold, yielding PL with an intensity PL(V) and the dissociation of the very same manifold into free carrier with an efficiency $\eta_{diss}(V)$, (b) the bias-dependent photoluminescence quenching efficiency PLQE(V), referenced to a voltage $V_0 = 0.5$ V, for a 150 nm thick PCPDTBT:ICBA blend. The inset shows the bias-dependent PL data, compared to the EL driven at a bias of 1.2 V. PLQE data are plotted for three different detection energies, below, at and above the PL maximum (line-connected symbols). Solid black points display the prediction by Equation 6.1 based on the bias-dependent TDCF experiments on the same devices. (c) the same for a 150 nm thick PCPDTBT:PCBM blend with the EL at 0.7 V.

Values of PLQE(V), evaluated at three detection wavelengths, below, at and above the PL maximum are shown in Figure 6.8 b and c with reference to a voltage $V_0 = 0.5$V, which is below the EL onset for both devices. PLQE(V) increases almost linearly with decreasing bias, approaching values of above 80% in the considered bias range. To test the validity of Equation 6.1, the bias dependent dissociation efficiency $\eta_{diss}(V)$ was derived from a combination of bias-dependent TDCF data and JV characteristics with the assumption that the photocurrent saturation at large reverse bias corresponds to complete dissociation Figure 6.9.

Figure 6.8 demonstrates that bias-dependent PL and TDCF data obey Equation 6.1 providing firm support that the state manifold involved in charge generation also dominates the PL intensity. This situation is slightly different for the more phase separated PCPDTBT:PCBM blend. While there is again a good spectral overlap between EL and PL, the PL at higher energies is bias-independent, pointing to polymer singlet emission. Considering only the PL quenching data at lower energies, Equation 6.1 is again fulfilled.

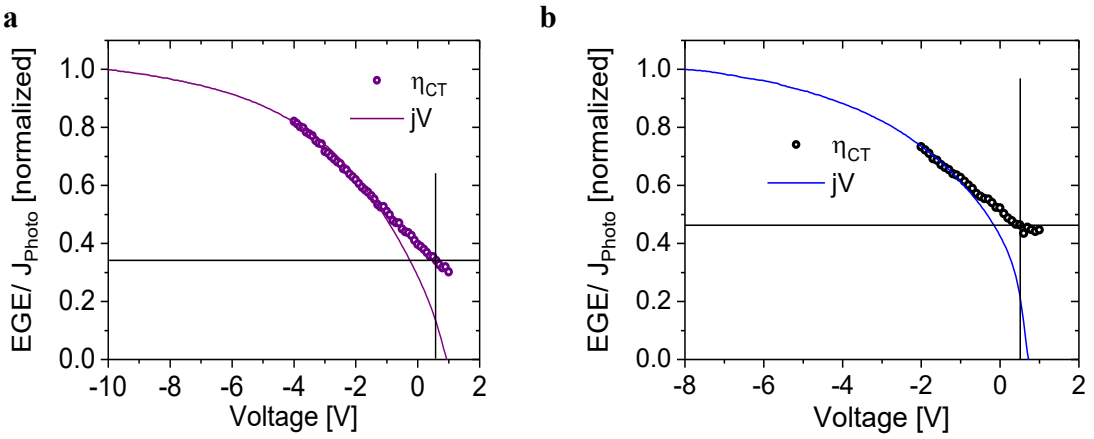

Figure 6.9.: Photogenerated charge versus photocurrent to obtain the dissociation efficiency as function of bias. Shown by the solid line is the normalized photocurrent (a) PCPDTBT:ICBA and (b) PCPDTBT:PCBM under simulated one sun illumination at 300 K. The field-dependence of the extracted charge from TDCF experiments at 300 K is scaled to give the best agreement to photocurrent characteristics. Data are shown for excitation at the polymer band edge with a photon energy of 1.55 eV. The scaled TDCF data yield the field-dependent efficiency for CT splitting, $\eta_{diss}(V)$. The splitting efficiency at the reference voltage (0.5 V) is shown with a horizontal line in the graphs.

A similar study of the well phase-separated 1F-PCPDTBT:PCBM blend would be instructive as this particular system might exhibit pools of both, delocalized and localized CT states. Unfortunately, the PL of this system was almost entirely dominated by the PL from aggregated polymer chains rendering a direct comparison of emissive states in PL and EL difficult.

This result, the insensitivity of temperature and field dependent TDCF data to the excitation energy, the bias dependent PLQE combined with the agreement between PL and EL spectra and the fulfillment of Rau's reciprocity relation between EL and EQE is inconsistent with the view that photoexcitation of these blends causes a significant occupation of low-lying, non-dissociable though emissive CT-states under the given excitation and bias conditions.

The data reveal that the excitation energy has a small to negligible effect on how temperature and field impact free charge generation: direct excitation of the low energy CT states leads to the same field and temperature dependence as excitation well above the band gap. This means, that the dissociation of such low energy CT states competes directly with its geminate recombination. As such, the CT dissociation efficiency depends on details of the energetic and mesoscale morphological

landscape at the heterojunction, e.g. its spatial and energetic disorder. This is why the choice of the components and the preparation conditions has such a strong effect on the charge generation efficiency, as reported here and in earlier work [26, 75, 181].

The presence of larger domains containing neat donor or acceptor material favors free charge formation [68, 75, 101, 103]. A systematic anti-correlation between activation energy and the fullerene correlation length supports this conclusion (see also Figure 6.4 and the corresponding text passage). On the other hand, there is no unambiguous relation between the activation energy and the driving force for charge separation $\Delta E_{CS} = E_{S_1^*} - E_{CS}$. This indicates that the excess energy provided to the system via a higher driving force alone is not necessarily sufficient for reducing the effective barrier for free charge formation in all of the investigated blend systems.

The activation energies for free charge formation found here are comparable to room temperature thermal energy being a measure of the extra thermal energy which is needed to dissociate the thermalized CT state population into free charge carriers. This observation is consistent with results from temperature-dependent EQE or PLQE experiments on various blends [66, 200]. This process is in direct competition with geminate recombination of exactly the same population. A direct correlation between the activation energy and the binding energy of the contributing states is, unfortunately, not trivial. While Braun's model predicts the zero field dissociation rate to follow an Arrhenius-type temperature dependence, as shown in subsection 2.3.2, the situation becomes more complicated in presence of energetic disorder. States close to or below the band edge become available for free charges, resulting in a concurrent reduction of the apparent activation energy or energetic disorder [217–219]. However, the observation that the most ordered system has the lowest activation energy questions the predominant effect of disorder on the activation energy. We propose that our activation energies, decreasing from around 44 meV for the highly intermixed PCPDTBT:ICBA blend down to below 20 meV for the phase-separated 1F-PCPDTBT:PCBM system, point to a significant reduction in the CT binding energy. Recent mesoscale quantum mechanical modeling has predicted the lowest interfacial CT state energy to be of the order of thermal energy [220]. Casalegno and coworkers also highlighted the importance of both carriers being able to delocalize for a weak binding of the lowest energy CT state; exactly what is seen here in the case of 1F-PCPDTBT:PCBM blend.

In conclusion, the finding that neither the temperature- nor the field dependence of generation is affected by the excitation energy settles a long lasting controversy about the fundamental processes involved in free charge generation. Notably, activation energies deduced from various temperature dependent measurements lie in the range of few tens of meV, with the lowest value for the most phase-separated blend. Electroluminescence, photoluminescence and charge generation properties are at variance to a two pool model where geminate recombination losses proceed mostly through a separate pool of strongly bound and therefore non-dissociable CT-states. Instead, population of a thermalized, low energy CT-manifold, independent of photon energy, is the precursor of most free charge and CT photon emission. Clearly, less than room temperature thermal energy is needed to render CT dissociation competitive to geminate recombination.

Chapter 7

Conclusion and Outlook

The core question of this work was the comprehensive investigation of free charge carrier generation and recombination dynamics in thin film organic and hybrid photovoltaic devices. To scope with this challenge, a new setup for all-optical and optoelectronic pump-probe measurements was designed and installed. This new setup allowed for experiments at application relevant conditions with an exceptional temporal and signal-to-noise resolution. The heart of the new setup is a new light source and an improved amplifier system for conducting Time Delayed Collection Field (TDCF) experiments. The improved temporal resolution, which was mainly determined by the rise time of the externally applied collection voltage and the pulse width of the laser pulse, was subsequently reduced from 50 ns to 2.3 ns. Another limitation was the inaccurate resolution of the voltage axis of the whole electronic part of the setup. Since the small change on top of the transient during pulsed illumination is compared to a very similar transient in the dark, the dynamic range has to be large. This problem was solved by using a real time 12 bit oscilloscope with a rather low bandwidth, and a new amplifier design with high accuracy and low noise. With these fundamental modifications, the TDCF setup is now able to safely measure low signals that correspond to an external quantum efficiency of 10^{-4}, and resolve transients of only a few nanoseconds. Thereby the signal-to-noise ratio was increased by one order of magnitude compared to Ref. [61, 75]. TDCF has been used to measure charge carrier generation, recombination and transport, as well as the field-, fluence- and temperature dependence of all parameters, in the same device and experimental setup. The device architecture is identical to the fully optimized design at application relevant conditions. This avoids experimental errors due to different preparation and measurement conditions, thereby demonstrating the strength of this technique. This improved setup was used in several

highly cited publications, reflecting its importance for the whole organic and hybrid semiconductor community [64, 67, 81, 107, 118, 159, 169, 221].

The same amplifier was used to measure the photoinduced carrier density with bias assisted charge extraction (BACE), where also the time resolution was improved by the use of fast switching CW lasers. The improved BACE method was applied to hybrid OPV materials made of inorganic-organic quantum-dots. Here, TDCF revealed fast free carrier recombination, in part assisted by traps, while the improved BACE method allowed for measurements of the high mobility present in this material.

Transient Absorption Spectroscopy (TAS) was set up with a gap-free excitation energy light source, a highly sensitive spectrometer system to cover the UV-VIS-NIR spectral range and a long mechanical optical delay line to allow for optical delays of 9 ns. The readout rate of 1 kHz ensures a good statistics of the collected data. The setup was designed to perform TAS in reflection and transmission mode, with the possibility to apply an external electric field. In TAS, the active material is excited with a short femtosecond laser pulse and the change in absorption is tracked using a delayed super continuum recorded with a high dynamic range spectrometer. The spectral resolution and sensitivity, which depend primarily on the super continuum generation, was improved. For example, conventional spectrometer systems record spectra at a maximum readout rate of 100 Hz whereas here, a custom made spectrometer with a readout rate of 1 kHz was developed to increase the signal-to-noise ratio with better statistics. First experiments were conducted in the end of this work. Thus, no comprehensive study on a large set of solar cells has been shown yet. That would be an enlightening task for future research on organic solar cells.

The improved and newly developed methods allowed for a sensitive quantification of charge generation and recombination losses, together with charge transport in organic and hybrid solar cells. A complete analysis of data recorded with the new setup was demonstrated for the model system of PbS based colloidal quantum dot solar cells. Specifically, TDCF experiments reveal a distinct field-dependence of generation, setting an upper limit to the achievable fill factor. Transient and low intensity steady state measurements highlight the role of traps, but non-geminate recombination is found to be strictly bimolecular at application relevant steady state conditions. On the other hand, the rather high effective mobility measured under steady state illumination, allows for fast extraction and ensures a reasonably high fill factor, despite fast non-geminate recombination.

The new TDCF setup also enabled for the first time the study of time-dependent non-geminate recombination for a high performance polymer-based device over a wide range of fluences and time periods – from nanosecond to microsecond, at which charge extraction occurs under relevant operation conditions. The experiments show that non-geminate recombination in the PCDTBT:PCBM blend is bimolecular at all times. This is in accordance with the findings from a large number of experiments on other organic solar cells, with various methods including transient and steady state techniques. Fast non-geminate recombination at early times was found to be contact mediated. For the PCDTBT:PCBM blend, as free charge generation was found to be field-independent, the only process which determines the field dependence of the solar cell's steady state photocurrent is indeed non-geminate recombination, which was shown to be dispersive and mediated by the contacts. Recombination at later time scales was determined by dispersive recombination in the bulk of the active layer, showing the characteristics of carrier dynamics in an exponential density of state distribution. The comparison with steady state recombination data suggested a very weak impact of non-thermalized carriers on the recombination properties of the solar cells under application relevant illumination conditions.

The highly sensitive setup was used to shed light on the pathways of charge generation in polymer-fullerene solar cells. A general finding is that neither temperature, nor excitation photon energy influence the field-dependence of the extracted charge. Moreover, the activation energy obtained from highly sensitive temperature dependent TDCF measurements does not depend on the excitation energy. Therefore, the values of the activation energy are a measure of the extra thermal energy needed to dissociate thermalized CT state populations into free charges. The activation energy values deduced from the temperature dependent measurements lie in the range of only a few tens of meV. As an important conclusion, the results provide conclusive support for the view that photoexcitation populates a thermalized CT manifold, which is the precursor of most free charge and CT photon emission, and that little thermal energy is needed to render dissociation of this CT population competitive to geminate recombination. In addition, a model was introduced to interconnect the dissociation efficiency of the charge transfer state with its recombination observable with photoluminescence. This model revealed an agreement between the photoluminescence quenching efficiency and the dissociation efficiency obtained with TDCF. This result, combined with the agreement between the PL and EL spectra, the fulfillment of Rau's reciprocity and the insensitivity of the tem-

perature and field dependent TDCF generation data to the excitation energy ruled out a previously proposed two-pool model for free charge formation and recombination. With that, this work provides an important contribution to the long-running debate regarding the predominant pathway of charge generation in organic solar cell devices. It also serves as a guide for simulation studies on the mechanism of free charge formation in the future.

In turn, the results from this thesis provided important ideas for further optimization of organic solar cells. It was found that the driving force for electron transfer plays only a minor role on charge separation, thereby opening design rules for increasing the open circuit voltage. Important for the preservation of the photogenerated current is the driving force for charge separation from the CT state to the CS state, along with an activation energy close to thermal energy. First applications where part of this requirements has been transposed have recently been published in the journal Science [3]. Here the donor polymer was blended with a non-fullerene acceptor yielding a very low donor LUMO - acceptor LUMO offset. The combination of a polymer-fullerene blend and a polymer - non-fullerene-acceptor blend in a tandem solar cell yield an efficiency of 17.3% [3]. Another interesting discovery was that the most phase separated material had the lowest activation energy. Newly designed materials should therefore show a tendency to form aggregates (as observed in fluorinated PCPDTBT [26, 67]), along with optimized energetics and a well defined morphology. This individual blend morphology, influenced by the specific preparation conditions, plays a very important role on device performance and needs to be controlled such that the interplay between efficient charge generation and transport is ensured while geminate and non-geminate recombination are highly suppressed. In the future, concepts developed here for analyzing TDCF, BACE and TAS data, along with steady state characterization methods can be applied to study other promising material classes such as non-fullerene acceptors and perovskites. The combined TDCF and TAS measurements can be improved to better understand the interaction between the states involved in free charge generation. The experimental improvements developed for this thesis and concomitantly the new insights that were gained should encourage further improvements to the various setups in the future, some suggestions are summarized in the following. Especially for TAS, a second structurally identical spectrometer should record a spectrum of the white light before the sample to obtain a transmission spectrum with only one shot. This will reduce shot to shot variations in the pumped and unpumped signals, thereby resulting in a cleaner $\Delta T/T$. Additionally, if the posi-

tion of the features are known, a transient at a single wavelength defined with a bandpass filter could be recorded with a lock-in amplifier, extending the sensitivity to the ΔOD range of 10^{-6}.

For TDCF, the electrical parts have been fully optimized. The rise time of the external voltage could be as fast as 60 *p*s, but the rise of the externally applied voltage pulse across a conventional designed organic solar cell is RC time limited, which is conventionally reduced by decreasing the active area and increasing the thickness. Although further miniaturization of the active area can increase the time resolution, the accuracy of the number of extracted charges will be reduced. It has to be taken into account that the detection efficiency decreases as bandwidth increases. Hence, a more elegant way of determining the charge carrier density in the device would be the combination of TDCF with all optical methods like TAS.

The results presented in this work and in many other publications using TDCF and similar methods show that the technical complexity of optimizing the measurement technologies has paid off and that further research into the optimization of these techniques is important in order to further expand optoelectronic time-resolved measurements at the University of Potsdam and worldwide in research and industry.

Bibliography

[1] NREL. *Best Research-Cell Efficiencies*. 2018.

[2] M. A. Green, Y. Hishikawa, E. D. Dunlop, D. H. Levi, J. Hohl-Ebinger, et al. Solar cell efficiency tables (version 51), *Prog. Photovoltaics Res. Appl.* **26**. (2018), p. 3.

[3] L. Meng, Y. Zhang, X. Wan, C. Li, X. Zhang, et al. Organic and solution-processed tandem solar cells with 17.3\% efficiency, *Science (80-.).* **2612** (2018).

[4] C. W. Tang. No Title, *Appl. Phys. Lett.* **48** (1986), p. 183.

[5] S. Nam, J. Seo, S. Woo, W. H. Kim, H. Kim, et al. Inverted polymer fullerene solar cells exceeding 10% efficiency with poly(2-ethyl-2-oxazoline) nanodots on electron-collecting buffer layers, *Nat. Commun.* **6** (2015), p. 8929.

[6] W. Zhao, S. Li, H. Yao, S. Zhang, Y. Zhang, et al. Molecular Optimization Enables over 13% Efficiency in Organic Solar Cells, *J. Am. Chem. Soc.* **139**. (2017), p. 7148.

[7] S. Zhang, Y. Qin, J. Zhu, and J. Hou. Over 14 % Efficiency in Polymer Solar Cells Enabled by a Chlorinated Polymer Donor, *Adv. Mater.* **30** (2018), p. 1800868.

[8] M. H. Park, J. H. Li, A. Kumar, G. Li, and Y. Yang. Doping of the metal oxide nanostructure and its influence in organic electronics, *Adv. Funct. Mater.* **19**. (2009), p. 1241.

[9] D. Neher. "How Hot are Organic Solar Cells", *Phys. behind Org. Semicond. Devices Occas. 80th Birthd. Heinz Bässler*. 2017.

[10] A. Armin, D. M. Stoltzfus, J. E. Donaghey, A. J. Clulow, R. Chandra, et al. Engineering dielectric constants in organic semiconductors, *J. Mater. Chem. C* (2017), p. 8.

[11] T. M. Clarke, A. Ballantyne, S. Shoaee, Y. W. Soon, W. Duffy, et al. Analysis of Charge Photogeneration as a Key Determinant of Photocurrent Density in Polymer: Fullerene Solar Cells. English, *Adv. Mater.* **22**. (2010), p. 5287.

[12] S. Few, J. M. Frost, and J. Nelson. Models of charge pair generation in organic solar cells, *Phys. Chem. Chem. Phys.* **17**. (2015), p. 2311.

[13] C. Deibel, T. Strobe, and V. Dyakonov. Role of the charge transfer state in organic donor-acceptor solar cells, *Adv. Mater.* **22**. (2010), p. 4097.

[14] H. Bässler and A. Köhler. "Hot or cold": How do charge transfer states at the donor–acceptor interface of an organic solar cell dissociate?, *Phys. Chem. Chem. Phys.* **17**. (2015), p. 28451.

[15] T. M. Clarke, A. M. Ballantyne, J. Nelson, D. D. C. Bradley, and J. R. Durrant. Free Energy Control of Charge Photogeneration in Polythiophene/-Fullerene Solar Cells: The Influence of Thermal Annealing on P3HT/PCBM Blends, *Adv. Funct. Mater.* **18**. (2008), p. 4029.

[16] S. D. Dimitrov, A. A. Bakulin, C. B. Nielsen, B. C. Schroeder, J. P. Du, et al. On the Energetic Dependence of Charge Separation in Low-Band-Gap Polymer/Fullerene Blends. English, *J. Am. Chem. Soc.* **134**. (2012), p. 18189.

[17] F. Etzold, I. A. Howard, N. Forler, D. M. Cho, M. Meister, et al. The Effect of Solvent Additives on Morphology and Excited-State Dynamics in PCPDTBT:PCBM Photovoltaic Blends. English, *J. Am. Chem. Soc.* **134**. (2012), p. 10569.

[18] G. Grancini, N. Martino, M. R. Antognazza, M. Celebrano, H.-j. Egelhaaf, et al. Influence of Blend Composition on Ultrafast Charge Generation and Recombination Dynamics in Low Band Gap Polymer-Based Organic Photovoltaics, *J. Phys. Chem. C* **116** (2012), p. 9838.

[19] J. M. Guo, H. Ohkita, S. Yokoya, H. Benten, and S. Ito. Bimodal Polarons and Hole Transport in Poly(3-hexylthiophene):Fullerene Blend Films. English, *J. Am. Chem. Soc.* **132**. (2010), p. 9631.

[20] S. Shoaee, S. Subramaniyan, H. Xin, C. Keiderling, P. S. Tuladhar, et al. Charge photogeneration for a series of thiazolo-thiazole donor polymers blended with the fullerene electron acceptors PCBM and ICBA, *Adv. Funct. Mater.* **23**. (2013), p. 3286.

[21] A. Troisi. How quasi-free holes and electrons are generated in organic photovoltaic interfaces. English, *Faraday Discuss.* **163** (2013), p. 377.

[22] G. Grancini, R. Sai Santosh Kumar, M. Maiuri, J. Fang, W. T. S. Huck, et al. Panchromatic "dye-doped" polymer solar cells: From femtosecond energy relays to enhanced photo-response, *J. Phys. Chem. Lett.* **4**. (2013), p. 442.

[23] I. A. Howard, F. Etzold, F. Laquai, and M. Kemerink. Nonequilibrium Charge Dynamics in Organic Solar Cells. English, *Adv. Energy Mater.* **4**. (2014), p. 1301743.

[24] R. R. Chance and C. L. Braun. Temperature dependence of intrinsic carrier generation in anthracene single crystals, *J. Chem. Phys.* **64**. (1976), p. 3573.

[25] M. C. Scharber, D. Mühlbacher, M. Koppe, P. Denk, C. Waldauf, et al. Design rules for donors in bulk-heterojunction solar cells - Towards 10 % energy-conversion efficiency, *Adv. Mater.* **18**. (2006), p. 789.

[26] S. Albrecht, K. Vandewal, J. R. Tumbleston, F. S. U. Fischer, J. D. Douglas, et al. On the Efficiency of Charge Transfer State Splitting in Polymer: Fullerene Solar Cells. English, *Adv. Mater.* **26**. (2014), p. 2533.

[27] G. Grancini, M. Binda, L. Criante, S. Perissinotto, M. Maiuri, et al. Measuring internal quantum efficiency to demonstrate hot exciton dissociation Reply. English, *Nat. Mater.* **12** (2013), p. 594.

[28] K. Vandewal, S. Albrecht, E. T. Hoke, K. R. Graham, J. Widmer, et al. Efficient charge generation by relaxed charge-transfer states at organic interfaces. eng, *Nat. Mater.* **13**. (2014), p. 63.

[29] C. Deibel, M. Mingebach, S. Walter, and C. Dyakonov. Direct and charge transfer state mediated photogeneration in polymer-fullerene bulk heterojunction solar cells, *Appl. Phys. Lett.* **100** (2012), p. 193302.

[30] D. D. Nuzzo, L. J. A. Koster, V. S. Gevaerts, S. C. J. Meskers, and R. A. J. Janssen. The Role of Photon Energy in Free Charge Generation in Bulk Heterojunction Solar Cells, *Adv. Energy Mater.* **4** (2014), p. 1400416.

[31] K. Vandewal, K. Tvingstedt, J. V. Manca, and O. Inganas. Charge-Transfer States and Upper Limit of the Open-Circuit Voltage in Polymer: Fullerene Organic Solar Cells. English, *Ieee J. Sel. Top. Quantum Electron.* **16**. (2010), p. 1676.

[32] S. T. Turner, P. Pingel, R. Steyrleuthner, E. J. W. Crossland, S. Ludwigs, et al. Quantitative Analysis of Bulk Heterojunction Films Using Linear Absorption Spectroscopy and Solar Cell Performance. English, *Adv. Funct. Mater.* **21**. (2011), p. 4640.

[33] O. V. Mikhnenko, F. Cordella, A. B. Sieval, J. C. Hummelen, P. W. M. Blom, et al. Temperature Dependence of Exciton Diffusion in Conjugated Polymers, *J. Phys. Chem. B* **112**. (2008), p. 11601.

[34] S. T. Hoffmann, H. Bässler, J. M. Koenen, M. Forster, U. Scherf, et al. Spectral diffusion in poly(para-phenylene)-type polymers with different energetic disorder, *Phys. Rev. B - Condens. Matter Mater. Phys.* **81**. (2010), p. 1.

[35] S. T. Hoffmann, S. Athanasopoulos, D. Beljonne, H. Bässler, and A. Köhler. How do triplets and charges move in disordered organic semiconductors? A Monte Carlo study comprising the equilibrium and nonequilibrium regime, *J. Phys. Chem. C* **116**. (2012), p. 16371.

[36] J. Orenstein and M. Kastner. Photocurrent Transient Spectroscopy: Measurement of the Density of Localized States, *Phys. Rev. Lett.* **46**. (1981), p. 1421.

[37] M. Schubert, E. Preis, J. C. Blakesley, P. Pingel, U. Scherf, et al. Mobility relaxation and electron trapping in a donor/acceptor copolymer, *Phys. Rev. B - Condens. Matter Mater. Phys.* **87**. (2013), p. 1.

[38] S. Athanasopoulos, S. T. Hoffmann, H. Bässler, A. Köhler, and D. Beljonne. To hop or not to hop? Understanding the temperature dependence of spectral diffusion in organic semiconductors, *J. Phys. Chem. Lett.* **4**. (2013), p. 1694.

[39] A. Melianas, V. Pranculis, Y. Xia, N. Felekidis, O. Inganäs, et al. Photogenerated Carrier Mobility Significantly Exceeds Injected Carrier Mobility in Organic Solar Cells, *Adv. Energy Mater.* **7** (2017), p. 1602143.

[40] J. Nelson. Diffusion-limited recombination in polymer-fullerene blends and its influence on photocurrent collection. English, *Phys. Rev. B* **67**. (2003).

[41] D. A. Vithanage, A. Devizis, V. Abramavicius, Y. Infahsaeng, D. Abramavicius, et al. Visualizing charge separation in bulk heterojunction organic solar cells, *Nat Commun* **4** (2013), p. 2334.

[42] V. Abramavičius, D. Amarasinghe Vithanage, A. Devižis, Y. Infahsaeng, A. Bruno, et al. Carrier motion in as-spun and annealed P3HT:PCBM blends revealed by ultrafast optical electric field probing and Monte Carlo simulations, *Phys. Chem. Chem. Phys.* **16**. (2014), p. 2686.

[43] A. Melianas, V. Pranculis, A. Devižis, V. Gulbinas, O. Inganäs, et al. Dispersion-dominated photocurrent in polymer:fullerene solar cells, *Adv. Funct. Mater.* **24**. (2014), p. 4507.

[44] A. Melianas, F. Etzold, T. J. Savenije, F. Laquai, O. Inganäs, et al. Photogenerated carriers lose energy during extraction from polymer-fullerene solar cells, *Nat. Commun.* **6**. (2015).

[45] Z. M. Beiley, E. T. Hoke, R. Noriega, J. Dacuna, G. F. Burkhard, et al. Morphology-Dependent Trap Formation in High Performance Polymer Bulk Heterojunction Solar Cells. English, *Adv. Energy Mater.* **1**. (2011), p. 954.

[46] P. A. Staniec, A. J. Parnell, A. D. F. Dunbar, H. N. Yi, A. J. Pearson, et al. The Nanoscale Morphology of a PCDTBT: PCBM Photovoltaic Blend. English, *Adv. Energy Mater.* **1**. (2011), p. 499.

[47] M. Scheidler, B. Cleve, H. Bässler, and P. Thomas. Monte Carlo simulation of bimolecular exciton annihilation in an energetically random hopping system, *Chem. Phys. Lett.* **225**. (1994), p. 431.

[48] T. M. Clarke, J. Peet, P. Denk, G. Dennler, C. Lungenschmied, et al. Non-Langevin bimolecular recombination in a silole-based polymer:PCBM solar cell measured by time-resolved charge extraction and resistance-dependent time-of-flight techniques, *Energy Environ. Sci.* **5**. (2012), p. 5241.

[49] D. Strickland and G. Mourou. Compression of Amplified Chirped Optical Pulses, *Opt. Commun.* **56**. (1985), p. 219.

[50] B. Kraabel, C. H. Lee, D. Mcbranch, D. Moses, N. S. Sariciftci, et al. Ultrafast photoinduced electron transfer in conducting polymer-buckminsterfullerene composites, *Chem. Phys. Lett.* **213**. (1993), p. 389.

[51] M. Hugenschmidt. *Lasermesstechnik: Diagnostik der Kurzzeitphysik.* Springer, Berlin / Heidelberg, 2007.

[52] C. G. Shuttle, B. O'Regan, A. M. Ballantyne, J. Nelson, D. D. C. Bradley, et al. Bimolecular recombination losses in polythiophene: Fullerene solar cells, *Phys. Rev. B* **78** (2008), p. 113201.

[53] J. D. Jonghe-risse, M. Causa, E. Buchaca-domingo, and M. Heeney. Using the Stark effect to understand charge generation in organic solar cells, *SPIE* **9549** (2015).

[54] M. Causa, I. Ramirez, J. F. M. Hardigree, M. Riede, and N. Banerji. Femtosecond Dynamics of Photoexcited C 60 Films, *J. Phys. Chem. Lett.* **9** (2018), p. 1885.

[55] A. Armin, J. R. Durrant, and S. Shoaee. Interplay Between Triplet - , Singlet-Charge Transfer States and Free Charge Carriers Defining Bimolecular Recombination Rate Constant of Organic Solar Cells, *J. Phys. Chem. C* **121** (2017), p. 13969.

[56] P. Langevin. "Recherches sur les gaz ionisés". PhD thesis. Université de Paris, 1902.

[57] J. Mort, I. Chen, A. Troup, J. Knights, R. Lujan, et al. Nongeminate Recombination of a-Si:H, **45**. (1980), p. 1348.

[58] D. Hertel, E. V. Soh, H. Bassler, and L. J. Rothberg. Electric field dependent generation of geminate electron-hole pairs in a ladder-type pi-conjugated polymer probed by fluorescence quenching and delayed field collection of charge carriers. English, *Chem. Phys. Lett.* **361**. (2002), p. 99.

[59] P. Langevin. Recombinaison et mobilite des ions dans les gaz, *Ann. Chim. Phys.* **28** (1903), p. 433.

[60] T. Offermans, S. C. J. Meskers, and R. A. J. Janssen. Time delayed collection field experiments on polymer: Fullerene bulk-heterojunction solar cells, *J. Appl. Phys.* **100**. (2006), p. 074509.

[61] J. Kniepert, M. Schubert, J. C. Blakesley, and D. Neher. Photogeneration and Recombination in P3HT/PCBM Solar Cells Probed by Time-Delayed Collection Field Experiments, *J. Phys. Chem. Lett.* **2**. (2011), p. 700.

[62] E. J. Ryder. Mobility of Holes and Electrons in High Electric Fields, *Phys. Rev.* **90**. (1953), p. 766.

[63] K. Pakbaz, C. H. Lee, A. J. Heeger, T. W. Hagler, and D. McBranch. Nature of the primary photoexcitations in poly(arylene-vinylenes), *Synth. Mater.* **64** (1994), p. 295.

[64] J. A. Love, M. Feuerstein, C. M. Wol, A. Facchetti, and D. Neher. Lead Halide Perovskites as Charge Generation Layers for Electron Mobility Measurement in Organic Semiconductors, *ACS Appl. Mater. Interfaces* **9**. (2017).

[65] T. Manaka, E. Lim, R. Tamura, and M. Iwamoto. Direct imaging of carrier motion in organic transistors by optical second- harmonic generation, *Nat. Photonics* **1** (2007), p. 581.

[66] M. Gerhard, A. P. Arndt, M. Bilal, U. Lemmer, M. Koch, et al. Field-induced exciton dissociation in PTB7-based organic solar cells, *Phys. Rev. B* **95**. (2017).

[67] J. Kurpiers, T. Ferron, S. Roland, M. Jakoby, T. Thiede, et al. Probing the pathways of free charge generation in organic bulk heterojunction solar cells, *Nat. Commun.* **9**. (2018).

[68] A. A. Bakulin, A. Rao, V. G. Pavelyev, P. H. M. van Loosdrecht, M. S. Pshenichnikov, et al. The Role of Driving Energy and Delocalized States

for Charge Separation in Organic Semiconductors. English, *Science (80-.).* **335**. (2012), p. 1340.

[69] G. Grancini, M. Maiuri, D. Fazzi, A. Petrozza, H.-J. J. Egelhaaf, et al. Hot exciton dissociation in polymer solar cells. English, *Nat. Mater.* **11** (2013), p. 29.

[70] P. K. Nayak, K. L. Narasimhan, and D. Cahen. Separating charges at organic interfaces: Effects of disorder, hot states, and electric field, *J. Phys. Chem. Lett.* **4**. (2013), p. 1707.

[71] A. A. Bakulin, S. D. Dimitrov, A. Rao, P. C. Y. Chow, C. B. Nielsen, et al. Charge-Transfer State Dynamics Following Hole and Electron Transfer in Organic Photovoltaic Devices. English, *J. Phys. Chem. Lett.* **4**. (2013), p. 209.

[72] D. M. Balazs, M. I. Nugraha, S. Z. Bisri, M. Sytnyk, W. Heiss, et al. Reducing charge trapping in PbS colloidal quantum dot solids. English, *Appl. Phys. Lett.* **104**. (2014).

[73] S. Albrecht, W. Schindler, J. Kurpiers, J. Kniepert, J. C. Blakesley, et al. On the Field Dependence of Free Charge Carrier Generation and Recombination in Blends of PCPDTBT/PC70BM: Influence of Solvent Additives, *J. Phys. Chem. Lett.* **3**. (2012), p. 640.

[74] M. H. Mingebach. "Photocurrent in Organic Solar Cells". PhD thesis. Julius Maximilians Universität Würzburg, 2012.

[75] S. Albrecht, S. Janietz, W. Schindler, J. Frisch, J. Kurpiers, et al. Fluorinated Copolymer PCPDTBT with Enhanced Open-Circuit Voltage and Reduced Recombination for Highly Efficient Polymer Solar Cells. English, *J. Am. Chem. Soc.* **134**. (2012), p. 14932.

[76] W. Shockley. The Theory of p-n Junctions in Semiconductors and p-n Junction Transistors, *Bell Syst. Tech. J.* **28**. (1949), p. 435.

[77] P. Würfel. *Physics of Solar Cells*. Second, Up. Wiley-VCH, 2009.

[78] U. Würfel, D. Neher, A. Spies, and S. Albrecht. Impact of charge transport on current-voltage characteristics and power-conversion efficiency of organic solar cells. eng, *Nat Commun* **6** (2015), p. 6951.

[79] D. Neher, J. Kniepert, A. Elimelech, and L. J. A. Koster. A New Figure of Merit for Organic Solar Cells with Transport-limited Photocurrents, *Nat. Publ. Gr.* **6**. (2016), p. 1.

[80] D. Bartesaghi, J. Kniepert, S. Roland, M. Turbiez, C. Pe, et al. Competition between recombination and extraction of free charges determines the fill factor of organic solar cells, *Nat. Commun.* **6**. (2015).

[81] J. Kurpiers, D. M. Balazs, A. Paulke, S. Albrecht, I. Lange, et al. Free carrier generation and recombination in PbS quantum dot solar cells, *Appl. Phys. Lett.* **108**. (2016).

[82] M. A. Green. Accuracy of analytical expressions for solar cell fill factors, *Sol. Cells* **7** (1982), p. 337.

[83] M. C. Scharber and N. S. Sariciftci. Efficiency of bulk-heterojunction organic solar cells, *Prog. Polym. Sci.* **38**. (2013), p. 1929.

[84] G. Yu and A. J. Heeger. Charge separation and photovoltaic conversion in polymer composites with internal donor / acceptor heterojunctions, *J. Appl. Phys.* **78** (1995), p. 4510.

[85] A. Köhler, D. A. dos Santos, D. Beljonne, Z. Shuai, J. L. Bredas, et al. Charge separation in localized and delocalized electronic states in polymeric semiconductors, *Nature* **392** (1998), p. 903.

[86] K. Vandewal, K. Tvingstedt, A. Gadisa, O. Inganäs, and J. V. Manca. On the origin of the open-circuit voltage of polymer–fullerene solar cells, *Nat. Mater.* **8**. (2009), p. 904.

[87] K. Tvingstedt, K. Vandewal, F. Zhang, and O. Inganäs. On the Dissociation Efficiency of Charge Transfer Excitons and Frenkel Excitons in Organic Solar Cells: A Luminescence Quenching Study, *J. Phys. Chem. C* **114**. (2010), p. 21824.

[88] K. Vandewal. Interfacial Charge Transfer States in Condensed Phase Systems, *Annu. Rev. Phys. Chem.* **67** (2016), p. 113.

[89] K. Vandewal, J. Benduhn, and V. C. Nikolis. How to determine optical gaps and voltage losses in organic photovoltaic materials, *Sustain. Energy Fuels* **2** (2017), p. 538.

[90] L. Onsager. Initial Recombination of Ions. *Phys. Rev.* **54** (1938), p. 554.

[91] F. Etzold, I. A. Howard, N. Forler, A. Melnyk, D. Andrienko, et al. Sub-ns triplet state formation by non-geminate recombination in PSBTBT:PC 70 BM and PCPDTBT:PC 60 BM organic solar cells, *Energy Environ. Sci.* **8**. (2015), p. 1511.

[92] C. Braun. Electric field assisted dissociation of charge transfer states as a mechanism of photocarrier production, *J. Chem. Phys.* **80**. (1984), p. 4157.

[93] T. E. Goliber and J. H. Perlstein. Analysis of photogeneration in a doped polymer system in terms of a kinetic model for electric-field-assisted dissociation of charge-transfer states, *J. Chem. Phys.* **80**. (1984), p. 4162.

[94] S. Barth, H. Bässler, U. Scherf, and K. Müllen. Photoconduction in thin films of a ladder-type poly-para-phenylene, *Chem. Phys. Lett.* **288**. (1998), p. 147.

[95] C. Schwarz, S. Tscheuschner, J. Frisch, S. Winkler, N. Koch, et al. Role of the effective mass and interfacial dipoles on exciton dissociation in organic donor-acceptor solar cells. English, *Phys. Rev. B* **87**. (2013), p. 155205.

[96] D. Veldman, S. C. J. Meskers, and R. A. J. Janssen. The Energy of Charge-Transfer States in Electron Donor-Acceptor Blends: Insight into the Energy Losses in Organic Solar Cells, *Adv. Funct. Mater.* **19**. (2009), p. 1939.

[97] I. W. Hwang, D. Moses, and A. J. Heeger. Photoinduced carrier generation in P3HT/PCBM bulk heterojunction materials. English, *J. Phys. Chem. C* **112**. (2008), p. 4350.

[98] F. L. Zhang, K. G. Jespersen, C. Bjorstrom, M. Svensson, M. R. Andersson, et al. Influence of solvent mixing on the morphology and performance of solar cells based on polyfluorene copolymer/fullerene blends, *Adv. Funct. Mater.* **16**. (2006), p. 667.

[99] S. D. Dimitrov, B. C. Schroeder, C. B. Nielsen, H. Bronstein, Z. Fei, et al. Singlet Exciton Lifetimes in Conjugated Polymer Films for Organic Solar Cells, *Polymers (Basel).* **8**. (2016).

[100] I. A. Howard, R. Mauer, M. Meister, and F. Laquai. Effect of Morphology on Ultrafast Free Carrier Generation in Polythiophene:Fullerene Organic Solar Cells, *J. Am. Chem. Soc.* **132** (2010), p. 14866.

[101] A. J. Barker, K. Chen, and J. M. Hodgkiss. Distance distributions of photogenerated charge pairs in organic photovoltaic cells, *J. Am. Chem. Soc.* **136**. (2014), p. 12018.

[102] A. C. Jakowetz, M. L. Bo, J. Zhang, A. Sadhanala, S. Huettner, et al. What Controls the Rate of Ultrafast Charge Transfer and Charge Separation E ffi ciency in Organic Photovoltaic Blends, *J. Am. Chem. Soc.* **138** (2016), p. 11672.

[103] M. Causa, J. De Jonghe-Risse, M. Scarongella, J. C. Brauer, E. Buchaca-Domingo, et al. The fate of electron-hole pairs in polymer:fullerene blends for organic photovoltaics. *Nat. Commun.* **7** (2016), p. 12556.

[104] S. Shoaee, T. M. Clarke, C. Huang, S. Barlow, S. R. Marder, et al. Acceptor Energy Level Control of Charge Photogeneration in Organic Donor/Acceptor Blends, *J. Am. Chem. Soc.* **132**. (2010), p. 12919.

[105] E. Buchaca-Domingo, a. J. Ferguson, F. C. Jamieson, T. McCarthy-Ward, S. Shoaee, et al. Additive-assisted supramolecular manipulation of polymer:fullerene blend phase morphologies and its influence on photophysical processes, *Mater. Horizons* **1**. (2014), p. 270.

[106] T. M. Burke and M. D. McGehee. How high local charge carrier mobility and an energy cascade in a three-phase bulk heterojunction enable >90% quantum efficiency, *Adv. Mater.* **26**. (2014), p. 1923.

[107] E. Collado-Fregoso, S. N. Hood, S. Shoaee, B. C. Schroeder, I. Mcculloch, et al. Intercalated vs Nonintercalated Morphologies in Donor Acceptor Bulk Heterojunction Solar Cells: PBTTT:Fullerene Charge Generation and Recombination Revisited, *J. Phys. Chem. Lett.* **8** (2017), p. 4061.

[108] R. Noriega, A. Salleo, and A. J. Spakowitz. Chain conformations dictate multiscale charge transport phenomena in disordered semiconducting polymers. *Proc. Natl. Acad. Sci. U. S. A.* **110**. (2013), p. 16315.

[109] P. Peumans and S. R. Forrest. Separation of geminate charge-pairs at donor – acceptor interfaces in disordered solids, *Chem. Phys. Lett.* **398** (2004), p. 27.

[110] N. J. Van Der Kaap and L. J. Koster. Charge carrier thermalization in organic diodes, *Sci. Rep.* **6** (2016), p. 19794.

[111] R. Mauer. Charge Generation , Transport and Recombination in Organic Solar Cells, *Thesis* (2012), p. 175.

[112] M. Schubert. "Elementary Processes in Layers of Electron Transporting Donor-Acceptor Copolymers : Investigation of Charge Transport and Application to Organic Solar Cells". PhD thesis. University of Potsdam, 2014.

[113] N. Tessler, Y. Preezant, N. Rappaport, and Y. Roichman. Charge transport in disordered organic materials and its relevance to thin-film devices: A tutorial review, *Adv. Mater.* **21**. (2009), p. 1.

[114] H. Bässler. Charge Transport in Disordered Organic Photoconductors, A Monte-Carlo Simulation Study, *Phys. Status Solidi B* **175** (1993), p. 15.

[115] A. J. Mozer, N. S. Sariciftci, A. Pivrikas, R. Österbacka, G. Juška, et al. Charge carrier mobility in regioregular poly(3-hexylthiophene) probed by

transient conductivity techniques: A comparative study, *Phys. Rev. B - Condens. Matter Mater. Phys.* **71**. (2005), p. 1.

[116] B. E. Wang, L. Hou, Z. Wang, S. Hellström, F. Zhang, et al. An Easily Synthesized Blue Polymer for High-Performance Polymer Solar Cells, *Adv. Mater.* **22** (2010), p. 5240.

[117] A. Melianas, V. Pranculis, D. Spoltore, J. Benduhn, O. Inganäs, et al. Charge Transport in Pure and Mixed Phases in Organic Solar Cells, *Adv. Energy Mater.* **7** (2017), p. 1700888.

[118] J. Kurpiers and D. Neher. Dispersive Non-Geminate Recombination in an Amorphous Polymer:Fullerene Blend, *Sci. Rep.* **6** (2016), p. 26832.

[119] V. Pranculis. "CHARGE TRANSFER DYNAMICS IN ORGANIC SOLAR CELLS". PhD thesis. Vilnius University, 2017.

[120] W. Shockley and W. T. Read. Statistics of the Recombination of Holes and Electrons, *Phys. Rev.* **87**. (1952), p. 835.

[121] A. Armin, J. Subbiah, M. Stolterfoht, S. Shoaee, Z. Xiao, et al. Reduced Recombination in High Efficiency Molecular Nematic Liquid Crystalline : Fullerene Solar Cells, *Adv. Energy Mater.* **2** (2016), p. 1600939.

[122] C. G. Shuttle, B. O'Regan, A. M. Ballantyne, J. Nelson, D. D. C. Bradley, et al. Experimental determination of the rate law for charge carrier decay in a polythiophene: Fullerene solar cell. English, *Appl. Phys. Lett.* **92**. (2008), p. 93311.

[123] G. Juška and K. Arlauskas. Charge Carrier Recombination in Bulk Heterojunction Organic Solar Cells, *Sol. Energy* (2010).

[124] J. Gorenflot, A. Paulke, F. Piersimoni, J. Wolf, Z. Kan, et al. From Recombination Dynamics to Device Performance : Quantifying the Efficiency of Exciton Dissociation , Charge Separation , and Extraction in Bulk Heterojunction Solar Cells with Fluorine-Substituted Polymer Donors, *Adv. Energy Mater.* **8** (2018), p. 1701678.

[125] S. L. Sheng. *Semiconductor Physical Electronics*. New York: Springer, 2006.

[126] C. Deibel, A. Baumann, and V. Dyakonov. Polaron recombination in pristine and annealed bulk heterojunction solar cells, *Appl. Phys. Lett.* **93**. (2008).

[127] C. Deibel, A. Wagenpfahl, and V. Dyakonov. Origin of reduced polaron recombination in organic semiconductor devices, *Phys. Rev. B* **80**. (2009), p. 75203.

[128] C. G. Shuttle, B. O'Regan, A. M. Ballantyne, J. Nelson, D. D. C. Bradley, et al. Experimental determination of the rate law for charge carrier decay in a polythiophene: Fullerene solar cell, *Appl. Phys. Lett.* **92**. (2008), p. 90.

[129] A. Hofacker and D. Neher. Dispersive and steady-state recombination in organic disordered semiconductors, *Phys. Rev. B* **96** (2017), p. 245204.

[130] J. Nelson. Diffusion-limited recombination in polymer-fullerene blends and its influence on ... *Phys. Rev. B* (2003), p. 1.

[131] C. Jacoboni, C. Canali, G. Otiaviani, and A. A. Quaranta. A review of some charge transport properties of silicon, *Solid. State. Electron.* **20** (1977), p. 77.

[132] I. A. Howard, H. Mangold, F. Etzold, D. Gehrig, and F. Laquai. Transient absorption data analysis by soft-modelling, *Ultrafast Dyn. Mol. Nanostructures Interfaces* (2013), p. 53.

[133] J. Kurpiers. Untersuchung der Ladungsträgergeneration und Rekombinationsdynamik in Polymer/Fulleren Solarzellen, *Diplomarbeit* (2013).

[134] THS309x High-voltage , Low-distortion , Current-feedback Operational Amplifiers, *Texas Instruments data sheet* (2015).

[135] R. Mancini. *Op Amps For Everyone*. Texas Instruments, 2002.

[136] A. Wentzel, C. Meliani, and W. Heinrich. RF Class-S Power Amplifiers: State-of-the-Art Results and Potential, *IMS* (2010), p. 812.

[137] N. H. Mahmoud and Y. I. Ismail. Accurate Rise Time and Overshoots Estimation in, *IEEE* **3**. (2003), p. 477.

[138] D. G. Cooke, F. C. Krebs, and P. U. Jepsen. Direct observation of sub-100 fs mobile charge generation in a polymer-fullerene film, *Phys. Rev. Lett.* **108**. (2012), p. 1.

[139] A. Kumar, S. L. Smith, W. Alex, T. S. V. D. Poll, G. C. Bazan, et al. Ultrafast Long-Range Charge Separation in Organic Semiconductor Photovoltaik Diodes, *Sciencexpress* **2**. (2013).

[140] P. Malý, J. Ravensbergen, J. T. Kennis, R. Van Grondelle, R. Croce, et al. Polarization-controlled optimal scatter suppression in transient absorption spectroscopy, *Sci. Rep.* **7**. (2017).

[141] N. W. Duffy, L. M. Peter, R. M. G. Rajapakse, and K. G. U. Wijayantha. A novel charge extraction method for the study of electron transport and interfacial transfer in dye sensitised nanocrystalline solar cells, *Electrochem. commun.* **2**. (2000), p. 658.

[142] I. Lange, J. Kniepert, P. Pingel, I. Dumsch, S. Allard, et al. Correlation between the Open Circuit Voltage and the Energetics of Organic Bulk Heterojunction Solar Cells. English, *J. Phys. Chem. Lett.* **4**. (2013), p. 3865.

[143] S. Albrecht, J. R. Tumbleston, S. Janietz, I. Dumsch, S. Allard, et al. Quantifying Charge Extraction in Organic Solar Cells: The Case of Fluorinated PCPDTBT. English, *J. Phys. Chem. Lett.* **5**. (2014), p. 1131.

[144] Y. Shirasaki, G. J. Supran, M. G. Bawendi, and V. Bulović. Emergence of colloidal quantum-dot light-emitting technologies, *Nat. Photonics* **7**. (2013), p. 13.

[145] C. H. M. Chuang, P. R. Brown, V. Bulovic, and M. G. Bawendi. Improved performance and stability in quantum dot solar cells through band alignment engineering. English, *Nat. Mater.* **13**. (2014), p. 796.

[146] Z. J. Ning, O. Voznyy, J. Pan, S. Hoogland, V. Adinolfi, et al. Air-stable n-type colloidal quantum dot solids, *Nat. Mater.* **13**. (2014), p. 822.

[147] F. Hetsch, N. Zhao, S. V. Kershaw, and A. L. Rogach. Quantum dot field effect transistors, *Mater. Today* **16**. (2013), p. 312.

[148] D. K. Kim, Y. M. Lai, B. T. Diroll, C. B. Murray, and C. R. Kagan. Flexible and low-voltage integrated circuits constructed from high-performance nanocrystal transistors. English, *Nat Commun* **3** (2012).

[149] M. I. Nugraha, R. Hausermann, S. Z. Bisri, H. Matsui, M. Sytnyk, et al. High Mobility and Low Density of Trap States in Dual-Solid-Gated PbS Nanocrystal Field-Effect Transistors, *Adv. Mater.* **27**. (2015), p. 2107.

[150] L. H. Lai, W. Gomulya, L. Protesescu, M. V. Kovalenko, and M. A. Loi. High performance photoelectrochemical hydrogen generation and solar cells with a double type II heterojunction, *Phys. Chem. Chem. Phys.* **16**. (2014), p. 7531.

[151] G. I. Koleilat, L. Levina, H. Shukla, S. H. Myrskog, S. Hinds, et al. Efficient, stable infrared photovoltaics based on solution-cast colloidal quantum dots, *ACS Nano* **2**. (2008), p. 833.

[152] C. Piliego, L. Protesescu, S. Z. Bisri, M. V. Kovalenko, and M. A. Loi. 5.2% efficient PbS nanocrystal Schottky solar cells. English, *Energy Environ. Sci.* **6**. (2013), p. 3054.

[153] K. Szendrei, W. Gomulya, M. Yarema, W. Heiss, and M. A. Loi. PbS nanocrystal solar cells with high efficiency and fill factor, *Appl. Phys. Lett.* **97**. (2010).

[154] X. Lan, O. Voznyy, A. Kiani, G. d. A. F. Pelayo, A. S. Abbas, et al. Passivation Using Molecular Halides Increases Quantum Dot Solar Cell Performance, *Adv. Mater.* (2015), n/a.

[155] M. J. Speirs, D. M. Balazs, H. H. Fang, L. H. Lai, L. Protesescu, et al. Origin of the increased open circuit voltage in PbS-CdS core-shell quantum dot solar cells, *J. Mater. Chem. A* **3**. (2015), p. 1450.

[156] A. A. Bakulin, S. Neutzner, H. J. Bakker, L. Ottaviani, D. Barakel, et al. Charge Trapping Dynamics in PbS Colloidal Quantum Dot Photovoltaic Devices, *ACS Nano* **7**. (2013), p. 8771.

[157] D. Zherebetskyy, M. Scheele, Y. Zhang, N. Bronstein, C. Thompson, et al. Hydroxylation of the surface of PbS nanocrystals passivated with oleic acid, *Science (80-.).* **344**. (2014), p. 1380.

[158] F. Deledalle, P. Shakya Tuladhar, J. Nelson, J. R. Durrant, and T. Kirchartz. Understanding the Apparent Charge Density Dependence of Mobility and Lifetime in Organic Bulk Heterojunction Solar Cells, *J. Phys. Chem. C* **118**. (2014), p. 8837.

[159] J. Kniepert, I. Lange, H. Wurst, K. Steffen, D. Neher, et al. Effect of bla, *J. Phys.* **25** (2014), p. 812537965.

[160] A. Foertig, J. Kniepert, M. Gluecker, T. Brenner, V. Dyakonov, et al. Nongeminate and Geminate Recombination in PTB7:PCBM Solar Cells, *Adv. Funct. Mater.* **24**. (2014), p. 1306.

[161] D. Rauh, C. Deibel, and V. Dyakonov. Charge Density Dependent Nongeminate Recombination in Organic Bulk Heterojunction Solar Cells. English, *Adv. Funct. Mater.* **22**. (2012), p. 3371.

[162] I. Lange, J. Kniepert, P. Pingel, I. Dumsch, S. Allard, et al. Correlation between the Open Circuit Voltage and the Energetics of Organic Bulk Heterojunction Solar Cells. English, *J. Phys. Chem. Lett.* **4**. (2013), p. 3865.

[163] S. Z. Bisri, C. Piliego, M. Yarema, W. G. Heiss, and M. A. Loi. Low Driving Voltage and High Mobility Ambipolar Field-Effect Transistors with PbS Colloidal Nanocrystals, *Adv. Mater.* **25**. (2013), p. 4309.

[164] A. Foertig, J. Rauh, V. Dyakonov, and C. Deibel. Shockley equation parameters of P3HT:PCBM solar cells determined by transient techniques, *Phys. Rev. B - Condens. Matter Mater. Phys.* **86**. (2012), p. 1.

[165] W. L. Leong, S. R. Cowan, and A. J. Heeger. Differential resistance analysis of charge carrier losses in organic bulk heterojunction solar cells: Observing

the transition from bimolecular to trap-assisted recombination and quantifying the order of recombination, *Adv. Energy Mater.* **1**. (2011), p. 517.

[166] T. M. Clarke, C. Lungenschmied, J. Peet, N. Drolet, and A. J. Mozer. A Comparison of Five Experimental Techniques to Measure Charge Carrier Lifetime in Polymer/Fullerene Solar Cells, *Adv. Energy Mater.* **5**. (2015).

[167] A. H. Ip, S. M. Thon, S. Hoogland, O. Voznyy, D. Zhitomirsky, et al. Hybrid passivated colloidal quantum dot solids, *Nat. Nanotechnol.* **7**. (2012), p. 577.

[168] C. Wehrenfennig, G. E. Eperon, M. B. Johnston, H. J. Snaith, and L. M. Herz. High charge carrier mobilities and lifetimes in organolead trihalide perovskites, *Adv. Mater.* **26**. (2014), p. 1584.

[169] A. Paulke, S. D. Stranks, J. Kniepert, J. Kurpiers, C. M. Wolff, et al. Charge carrier recombination dynamics in perovskite and polymer solar cells, *Appl. Phys. Lett.* **108** (2016), p. 113505.

[170] O. Oklobia and T. S. Shafai. A study of donor/acceptor interfaces in a blend of P3HT/PCBM solar cell: Effects of annealing and PCBM loading on optical and electrical properties, *Solid. State. Electron.* **87** (2013), p. 64.

[171] S. T. Hoffmann, F. Jaiser, A. Hayer, H. B??ssler, T. Unger, et al. How do disorder, reorganization, and localization influence the hole mobility in conjugated copolymers?, *J. Am. Chem. Soc.* **135**. (2013), p. 1772.

[172] J. Orenstein and M. Kastner. Thermalization and Recombination in Amorphous Semiconductors, *Solid State Commun.* **40** (1981), p. 85.

[173] A. Devizis, A. Serbenta, K. Meerholz, D. Hertel, and V. Gulbinas. Ultrafast dynamics of carrier mobility in a conjugated polymer probed at molecular and microscopic length scales, *Phys. Rev. Lett.* **103**. (2009), p. 1.

[174] D. Amarasinghe Vithanage, a. Devižis, V. Abramavičius, Y. Infahsaeng, D. Abramavičius, et al. Visualizing charge separation in bulk heterojunction organic solar cells. *Nat. Commun.* **4** (2013), p. 2334.

[175] N. J. van der Kaap and L. J. A. Koster. Charge carrier thermalization in organic diodes. *Sci. Rep.* **6** (2016), p. 19794.

[176] E. Wang, L. Wang, L. Lan, C. Luo, W. Zhuang, et al. High-performance polymer heterojunction solar cells of a polysilafluorene derivative, *Appl. Phys. Lett.* **92**. (2008), p. 2008.

[177] B. C. Schroeder, Z. Huang, R. S. Ashraf, J. Smith, P. D'Angelo, et al. Silaindacenodithiophene-based low band gap polymers - The effect of fluo-

rine substitution on device performances and film morphologies, *Adv. Funct. Mater.* **22**. (2012), p. 1663.

[178] F. Etzold, I. A. Howard, R. Mauer, M. Meister, T. D. Kim, et al. Ultrafast exciton dissociation followed by nongeminate charge recombination in PCDTBT:PCBM photovoltaic blends, *J. Am. Chem. Soc.* **133**. (2011), p. 9469.

[179] S. Roland, M. Schubert, B. A. Collins, J. Kurpiers, Z. H. Chen, et al. Fullerene-Free Polymer Solar Cells with Highly Reduced Bimolecular Recombination and Field-Independent Charge Carrier Generation. English, *J. Phys. Chem. Lett.* **5**. (2014), p. 2815.

[180] D. W. Gehrig, S. Roland, I. A. Howard, V. Kamm, H. Mangold, et al. Efficiency-Limiting Processes in Low-Bandgap Polymer:Perylene Diimide Photovoltaic Blends. English, *J. Phys. Chem. C* **118**. (2014), p. 20077.

[181] J. Kniepert, I. Lange, N. J. Van Der Kaap, L. J. A. Koster, and D. Neher. A Conclusive view on charge generation, recombination, and extraction in as-prepared and annealed P3HT:PCBM Blends: Combined experimental and simulation work, *Adv. Energy Mater.* **4** (2014), p. 1301401.

[182] L. J. A. Koster, E. C. P. Smits, V. D. Mihailetchi, and P. W. M. Blom. Device model for the operation of polymer/fullerene bulk heterojunction solar cells, *Phys. Rev. B - Condens. Matter Mater. Phys.* **72**. (2005), p. 085205.

[183] R. Kohlrausch. Theorie des elektrischen Rückstandes in der Leidner Flasche, *Ann. der Phys. und Chemie* **91**. (1854), p. 179.

[184] M. Stolterfoht, A. Armin, B. Philippa, R. D. White, P. L. Burn, et al. Photocarrier drift distance in organic solar cells and photodetectors, *Sci. Rep.* **5** (2015).

[185] T. M. Clarke, J. Peet, A. Nattestad, N. Drolet, G. Dennler, et al. Charge carrier mobility, bimolecular recombination and trapping in polycarbazole copolymer:fullerene (PCDTBT:PCBM) bulk heterojunction solar cells, *Org. Electron.* **13**. (2012), p. 2639.

[186] W. L. Leong, G. Hernandez-Sosa, S. R. Cowan, D. Moses, A. J. Heeger, et al. Manifestation of Carrier Relaxation Through the Manifold of Localized States in PCDTBT:PC60BM Bulk Heterojunction Material: The Role of PC84BM Traps on the Carrier Transport. English, *Adv. Mater.* **24**. (2012), p. 2273.

[187] A. Foertig, J. Kniepert, M. Gluecker, T. Brenner, V. Dyakonov, et al. Nongeminate and Geminate Recombination in PTB7:PCBM Solar Cells, *Adv. Funct. Mater.* **24**. (2013), p. 1306.

[188] D. A. Vithanage, E. Wang, Z. Wang, F. Ma, O. Inganäs, et al. Charge carrier dynamics of polymer:fullerene blends: From geminate to non-geminate recombination, *Adv. Energy Mater.* **4**. (2014), p. 1.

[189] T. M. Clarke, F. C. Jamieson, and J. R. Durrant. Transient Absorption Studies of Bimolecular Recombination Dynamics in Polythiophene/Fullerene Blend Films. English, *J. Phys. Chem. C* **113**. (2009), p. 20934.

[190] A. J. Ferguson, N. Kopidakis, S. E. Shaheen, and G. Rumbles. Dark Carriers, Trapping, and Activation Control of Carrier Recombination in Neat P3HT and P3HT:PCBM Blends. English, *J. Phys. Chem. C* **115**. (2011), p. 23134.

[191] S. Yamamoto, H. Ohkita, H. Benten, and S. Ito. Role of Interfacial Charge Transfer State in Charge Generation and Recombination in Low-Bandgap Polymer Solar Cell, *J. Phys. Chem. C* **116**. (2012), p. 14804.

[192] C. S. Ponseca, A. Yartsev, E. Wang, M. R. Andersson, D. Vithanage, et al. Ultrafast terahertz photoconductivity of bulk heterojunction materials reveals high carrier mobility up to nanosecond time scale, *J. Am. Chem. Soc.* **134**. (2012), p. 11836.

[193] L. M. Andersson, A. Melianas, Y. Infahasaeng, Z. Tang, A. Yartsev, et al. Unified study of recombination in polymer: Fullerene solar cells using transient absorption and charge-extraction measurements, *J. Phys. Chem. Lett.* **4**. (2013), p. 2069.

[194] D. H. K. Murthy, M. Gao, M. J. W. Vermeulen, L. D. A. Siebbeles, and T. J. Savenije. Mechanism of Mobile Charge Carrier Generation in Blends of Conjugated Polymers and Fullerenes: Significance of Charge De localization and Excess Free Energy. English, *J. Phys. Chem. C* **116**. (2012), p. 9214.

[195] B. Philippa, M. Stolterfoht, R. D. White, M. Velusamy, P. L. Burn, et al. Molecular weight dependent bimolecular recombination in organic solar cells, *J. Chem. Phys.* **141**. (2014).

[196] C. M. Proctor, M. Kuik, and T.-Q. Nguyen. Charge carrier recombination in organic solar cells, *Prog. Polym. Sci.* **38**. (2013), p. 1941.

[197] K. M. Pelzer and S. B. Darling. Charge generation in organic photovoltaics: a review of theory and computation, *Mol. Syst. Des. Eng.* **1**. (2016), p. 10.

[198] D. M. Stoltzfus, J. E. Donaghey, A. Armin, P. E. Shaw, P. L. Burn, et al. Charge Generation Pathways in Organic Solar Cells: Assessing the Contribution from the Electron Acceptor, *Chem. Rev.* **116**. (2016), p. 12920.

[199] R. Scholz, R. Luschtinetz, G. Seifert, T. Jägerler-Hoheisel, C. Körner, et al. Quantifying charge transfer energies at donor-acceptor interfaces in small-molecule solar cells with constrained DFTB and spectroscopic methods, *J. Phys. Condens. Matter* **25** (2013), p. 473201.

[200] F. Gao, W. Tress, J. Wang, and O. Inganäs. Temperature dependence of charge carrier generation in organic photovoltaics, *Phys. Rev. Lett.* **114** (2015), p. 128701.

[201] T. Hahn, S. Tscheuschner, C. Saller, P. Strohriegl, B. Puttaraju, et al. The Role of Intrinsic Photogeneration in Single Layer and Bilayer Solar Cells with C 60 and PCBM, *J. Phys. Chem. C* **120**. (2016), p. 25083.

[202] M. Caironi, M. Bird, D. Fazzi, Z. Chen, R. Di Pietro, et al. Very low degree of energetic disorder as the origin of high mobility in an n-channel polymer semiconductor, *Adv. Funct. Mater.* **21**. (2011), p. 3371.

[203] J. T. Rogers, K. Schmidt, M. F. Toney, E. J. Kramer, and G. C. Bazan. Structural order in bulk heterojunction films prepared with solvent additives, *Adv. Mater.* **23**. (2011), p. 2284.

[204] X. Du, X. Jiao, S. Rechberger, J. D. Perea, M. Meyer, et al. Crystallization of Sensitizers Controls Morphology and Performance in Si-/C-PCPDTBT-Sensitized P3HT:ICBA Ternary Blends, *Macromolecules* **50**. (2017), p. 2415.

[205] C. Scharsich, F. S. U. Fischer, K. Wilma, R. Hildner, S. Ludwigs, et al. Revealing structure formation in PCPDTBT by optical spectroscopy, *J. Polym. Sci. Part B Polym. Phys.* **53**. (2015), p. 1416.

[206] J. A. Bartelt, Z. M. Beiley, E. T. Hoke, W. R. Mateker, J. D. Douglas, et al. The importance of fullerene percolation in the mixed regions of polymer-fullerene bulk heterojunction solar cells, *Adv. Energy Mater.* **3**. (2013), p. 364.

[207] N. Banerji, S. Cowan, M. Leclerc, E. Vauthey, and A. J. Heeger. Exciton Formation, Relaxation, and Decay in PCDTBT, *J. Am. Chem. Soc.* **132**. (2010), p. 17459.

[208] K. Vandewal, K. Tvingstedt, A. Gadisa, O. Inganas, and J. V. Manca. Relating the open-circuit voltage to interface molecular properties of

donor:acceptor bulk heterojunction solar cells. English, *Phys. Rev. B* **81**. (2010), p. 125204.

[209] V. D. Mihailetchi, L. J. A. Koster, J. C. Hummelen, and P. W. M. Blom. Photocurrent Generation in Polymer-Fullerene Bulk Heterojunctions, *Phys. Rev. Lett.* **93**. (2004), p. 216601.

[210] V. Dyakonov, C. Deibel, and T. Strobel. Origin of the Efficient Polaron-Pair Dissociation in Polymer-Fullerene Blends, *Phys. Rev. Lett.* **103**. (2009), p. 036402.

[211] M. Wojcik, A. Nowak, and K. Seki. Geminate electron-hole recombination in organic photovoltaic cells . A semi-empirical theory, *J. Chem. Phys.* **146** (2017), p. 054101.

[212] U. Rau. Reciprocity relation between photovoltaic quantum efficiency and electroluminescent emission of solar cells, *Phys. Rev. B* **76** (2007), p. 085303.

[213] K. Vandewal, J. Widmer, T. Heumueller, C. J. Brabec, M. D. McGehee, et al. Increased open-circuit voltage of organic solar cells by reduced donor-acceptor interface area, *Adv. Mater.* **26**. (2014), p. 3839.

[214] Y. S. Huang, S. Westenhoff, I. Avilov, P. Sreearunothai, J. M. Hodgkiss, et al. Electronic structures of interfacial states formed at polymeric semiconductor heterojunctions, *Nat. Mater.* **7**. (2008), p. 483.

[215] T. Hahn, S. Tscheuschner, F. J. Kahle, M. Reichenberger, S. Athanasopoulos, et al. Monomolecular and Bimolecular Recombination of Electron–Hole Pairs at the Interface of a Bilayer Organic Solar Cell, *Adv. Funct. Mater.* **27**. (2017).

[216] Z. D. Popovic. A study of carrier generation in x-metal-free phthalocyanine, *Chem. Phys.* **78**. (1983), p. 1552.

[217] U. Albrecht and B. Heinz. Yield of geminate pair dissociation in an energetically random hopping system, *Chem. Phys. Lett.* **235** (1995), p. 389.

[218] E. V. Emelianova, M. V. D. Auweraer, H. Bässler, E. V. Emelianova, M. V. D. Auweraer, et al. Hopping approach towards exciton dissociation in conjugated polymers, *J. Chem. Phys.* **128** (2008), p. 224709.

[219] S. N. Hood and I. Kassal. Entropy and disorder enable charge separation in organic solar cells, *J. Phys. Chem. Lett.* **7**. (2016), p. 4495.

[220] M. Casalegno, R. Pastore, J. Idé, R. Po, and G. Raos. Origin of Charge Separation at Organic Photovoltaic Heterojunctions: A Mesoscale Quantum Mechanical View, *J. Phys. Chem. C* **121** (2017), 1669316701.

[221] N. A. Ran, S. Roland, J. A. Love, V. Savikhin, C. J. Takacs, et al. Impact of interfacial molecular orientation on radiative recombination and charge generation efficiency, *Nat. Commun.* **8** (2017), p. 79.

Appendix A

Appendix

A.1. Organic Solar Cell Characterization and Evaluation

A.1.1. Electroluminescence

For Electroluminescence the device is hold at a constant voltage (Keithley 2400) for one second. The emission spectrum is recorded with an Andor Solis SR393i-B spectrograph with a silicon detector DU420A-BR-DD and an Indium Gallium Arsenide DU491A-1.7 detector. A calibrated Oriel 63355 lamp was used to correct the spectral response. EL spectra where recorded with different gratings with center wavelengths of 800 nm, 1100 nm and 1400 nm and merged afterwards with a home-built software.

A.1.2. External Quantum Efficiency

A broad white light from a 300 W Halogen lamp (Phillips) is chopped (thorlabs MC2000), guided through a cornerstone Monochromator and coupled into an optical quartz fiber, calibrated with Newport Photodiodes (818-UV and 818-IR) and a SR 830 Lock-In Amplifier which measures also the response of the solar cell. Absorbance was measured with a Varian Cary 5000 in double beam mode.

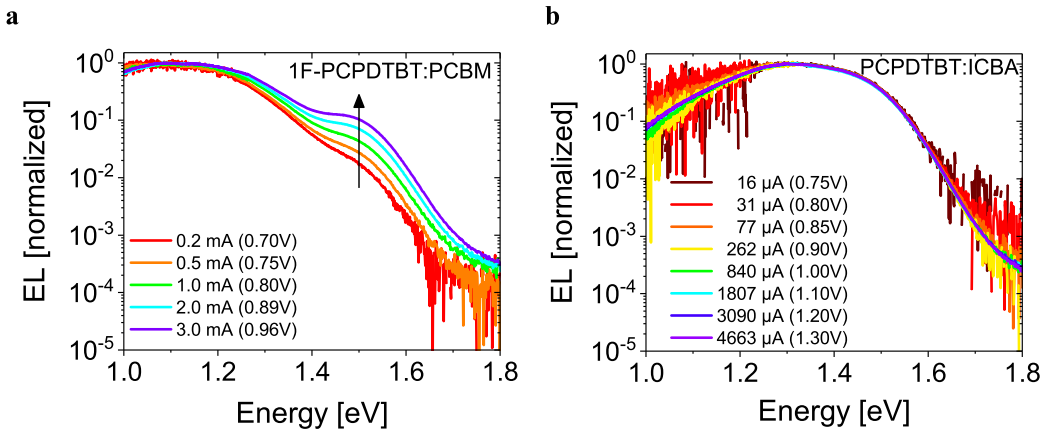

Figure A.1.: Room temperature bias-dependent electroluminescence spectra devices made from 1F-PCPDTBT (a) and PCPDTBT:ICBA (b). Spectra were normalized to their maximum.

A.1.3. Current Voltage Characteristics

The solar cell characteristics were measured with a Newport Oriel Sol2A simulator calibrated to 100 mW/cm² and a Keithley 2400 source/measure device. The samples were held at 25°C during measurement. The sun simulator was calibrated with a KG3 filtered silicon reference cell calibrated at Fraunhofer ISE.

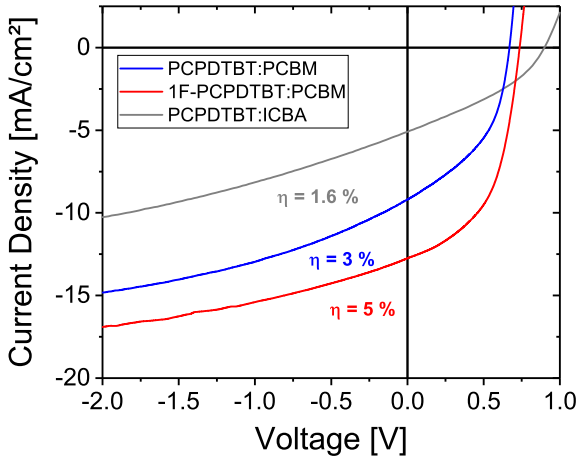

Figure A.2.: Current voltage characteristics of the studied blends in chapter 6 with a thickness of approx. 110 nm under simulated AM1.5G illumination.

A.1.4. Rate Equation Solver - Source Code

Listing A.1: *copy-paste* Matlab Source Code for solving rate equations [55] following all states involved in charge generation here for a PCPDTBT:ICBA device.

```
close all
clear

RGB = {  [252,141,89; %% each line is a color; each two lines in par define
           44,131,186]./255, ...
          ...
         [241,163,64;
         153,142,195]./255 , ...
          ...
         [77,77,77;
          178,24,43]./255 , ...
          ...
         [228,26,28;
          77,175,74]./255 } ; %Set two gradient colors


 RGBsingle = RGB{1}; %%select the gradient
t_max = 1e-4;
set(0, 'DefaultAxesFontName','Calibri Light');
set(0,'DefaultTextFontname', 'Calibri Light')

font_size = 10;
set(0, 'DefaultAxesFontSize',font_size);
set(0, 'DefaultAxesFontSize',font_size);


%%%%%%%%rate equation solver%%%%%%%%%%%%
%%
size        = 6e6;
exponent    = 2;
delta_t     = 1e-14;
times       = logspace(-11, -5, size);
diff_times  = 0.*diff(times)+ delta_t;
```

```
Gen_rates    = 1e16;%fliplr(logspace(14, 17, 5));

        M = numel(Gen_rates);

        R = fliplr(linspace(RGBsingle(1,1),RGBsingle(2,1),M)) .';
        G = fliplr(linspace(RGBsingle(1,2),RGBsingle(2,2),M)) .';
        B = fliplr(linspace(RGBsingle(1,3),RGBsingle(2,3),M)) .';
        MyColorMap = flipud(horzcat(R, G, B));

set(groot,'defaultAxesColorOrder',MyColorMap)

n_ph_safe             =    zeros(10^exponent,numel(Gen_rates))   ;
n_exc_safe            =    zeros(10^exponent,numel(Gen_rates))   ;
n_S1_safe             =    zeros(10^exponent,numel(Gen_rates))   ;
n_T1_safe             =    zeros(10^exponent,numel(Gen_rates))   ;
n_CT1_safe            =    zeros(10^exponent,numel(Gen_rates))   ;
n_CT3_safe            =    zeros(10^exponent,numel(Gen_rates))   ;
n_CS_safe             =    zeros(10^exponent,numel(Gen_rates))   ;


time_safe             =    zeros(10^exponent,1)   ;
BMR                   =    zeros(10^exponent,numel(Gen_rates))   ;
BMR_no_dark_holes     =    BMR;
Gen_rate_safe         =    zeros(size,1)   ;
time2_safe            =    Gen_rate_safe;




n_ph    =    0;
n_exc   =    0;
n_S1    =    0;
n_T1    =    0;
n_CT1   =    0;
n_CT3   =    0;
n_CS    =    0;
```

```
dn_ph       =    0;
dn_exc      =    0;
dn_S1           =0;
dn_T1           =0;
dn_CT1 = 0;
dn_CT3 = 0;
dn_CS      =0;


k_d_ex        =    8e12;
k_f_ex             =    1e10;
k_TA             =    0;
k_BET             =    0;
k_ISC       =    0;

k_r       =    0;
k_d       =    4e8; %8e8; Hz at 0 V and -2 V

k_f       =    2.7e9;
k_coll = 0;

t = 0;




for index_gen_rates = 1:numel(Gen_rates)
    time = 0;
    t = 0;
for index = 1:size

    time = time + delta_t;

%
    Gen_rate = Gen_rates(index_gen_rates) ;


   if index == 1
```

```
        n_S1        =    Gen_rate ;%%
    else
        dn_S1       =     - k_d_ex.*n_S1 -k_f_ex.*n_S1     ;

        dn_T1       =     - k_TA.*n_T1.*n_CS + k_BET.*n_CT3;

    %end
        dn_CT1      =     0.25*k_r.*n_CS.^2- k_d.*n_CT1 - k_f.*n_CT1 + k_d_ex
        dn_CT3      =     0.75*k_r.*n_CS.^2- k_d.*n_CT3 - k_BET.*n_CT3 + k_IS
        dn_CS       =     -k_r.*n_CS.^2 + k_d.*(n_CT1+n_CT3) - k_coll.*n_CS;



      n_S1              =    n_S1         +    dn_S1.*delta_t;
     n_T1               =    n_T1         +    dn_T1.*delta_t;
     n_CT1              =    n_CT1        +    dn_CT1.*delta_t;
     n_CT3              =    n_CT3        +    dn_CT3.*delta_t;
     n_CS               =    n_CS         +    dn_CS.*delta_t;
    end
if n_S1 <=0
     n_S1 = 0;
end

if n_T1 <=0
     n_T1 = 0;
end
if n_CT1 <=0
     n_CT1 = 0;
end
if n_CT3 <=0
     n_CT3 = 0;
end

if n_CS <=0
     n_CS = 0;
end
```

```
    if mod(index,10^exponent) == 0
        t = t + 1;
        n_S1_safe(t,index_gen_rates)          =   n_S1 ;
        n_T1_safe(t,index_gen_rates)          =   n_T1 ;
        n_CT1_safe(t,index_gen_rates)         =   n_CT1   ;
        n_CT3_safe(t,index_gen_rates)         =   n_CT3   ;
       n_CS_safe(t,index_gen_rates)           =   n_CS   ;
       if index_gen_rates == 1
            time_safe(t,1)                    =   index.*delta_t   ;
        end

    elseif index == 1;
        t = t + 1;
        n_S1_safe(t,index_gen_rates)          =   n_S1 ;
        n_T1_safe(t,index_gen_rates)          =   n_T1 ;
        n_CT1_safe(t,index_gen_rates)         =   n_CT1   ;
        n_CT3_safe(t,index_gen_rates)         =   n_CT3   ;
       n_CS_safe(t,index_gen_rates)           =   n_CS   ;



        if index_gen_rates == 1
            time_safe(t,1)                    =   index.*delta_t   ;
        end


    end

end

end

%%
```

```
n_tot_safe = n_CT1_safe + n_CT3_safe + n_CS_safe;

figure(1);
p1 = semilogx(time_safe, n_S1_safe,'g','LineWidth', 1); hold on
p2 = plot(time_safe, n_CT1_safe,'-') ;
plot(time_safe, n_CT3_safe,'--') ;
plot(time_safe, n_CS_safe,'o') ;
plot(time_safe, n_tot_safe, ':','LineWidth', 2 )
ylabel('n / cm^{-3}')
xlabel('time / s')
xlim([1e-12 3e-8])
legend('S_1','CT_1','CT_3','CS','n_{tot}')


hold off
```

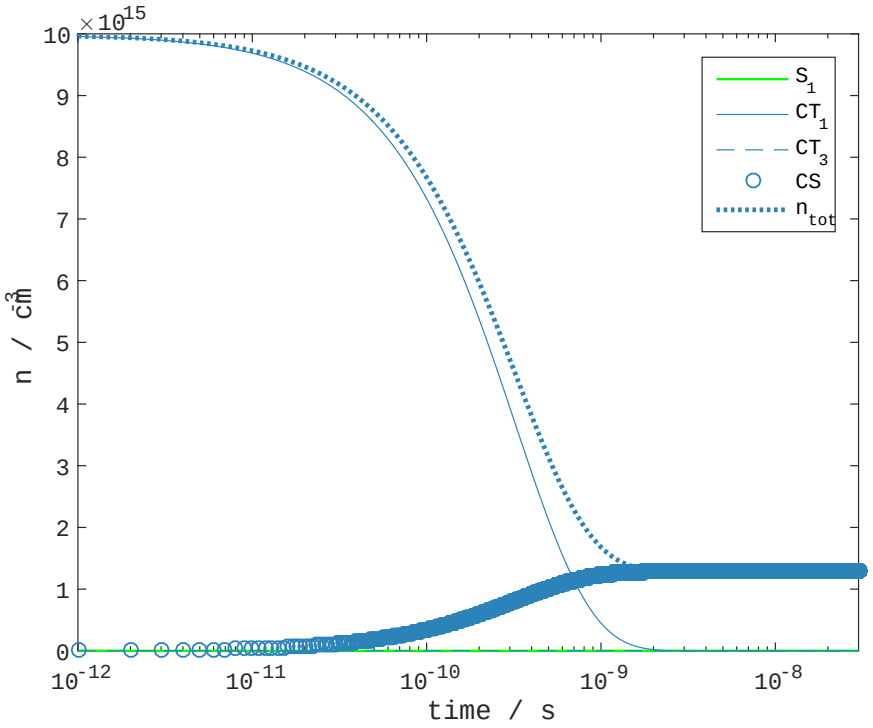

Figure A.3.: Calculated kinetics and rates of charge transfer state, free charges and total charges of a PCPDTBT:ICBA blend studied in chapter 6 with a thickness of approx. 110 nm for an excitation density of 10^{16} cm^{-3} photons.

A.1.5. Drift Diffusion Simulation - Source Code

Listing A.2: *copy-paste* Matlab Source Code for Drift Diffusion Simulations of a time-delayed charge extraction experiment on a 70 nm thin PCDTBT:PCBM device

```
clear
% specify time steps
% t = logspace(-9,-6,1000); %or
t = linspace(0,5e-6,1e3);

% specify spatial coordinates

dx = 2E-9;      % position step
xMax = 70E-9;   % active layer thickness
x = 0:dx:xMax; % position simulation interval

numx = length(x);
dtAll = diff(t);
numt = length(t);

% Diffusion coefficients, k2, profiles

mue = 1*1e-4*1e-4;   % cm^2/Vs
muh = 1*1e-6*1e-4;   % cm^2/Vs
alpha = 0*1E7; % 0 means homogeneous generation profile
k2 = 1*1e-17;  % bimolecular recombination coefficient

% Analytical Fit to Background charge profiles simulated with
% J.A. Koster's Simulation Zimtwickel for a 70nm PCDTBT:PCBM device
nBG = 1*x.^4.3./((x - 70.5*1e-9).*(x-70.5*1e-9))*1e-1*(1E9)^4*1e3;

% specify initial photogeneration profile for three densities

n_x_t1(:,1) = 1e23*exp(-x*alpha);
h_x_t1(:,1) = n_x_t1(:,1);

n_x_t2(:,1) = 2e23*exp(-x*alpha);
h_x_t2(:,1) = n_x_t2(:,1);
```

```
n_x_t3(:,1) = 3e23*exp(-x*alpha);
h_x_t3(:,1) = n_x_t3(:,1);

Bleft = 1; %left Boundary   0 = Surface Recombination
Bright = 1; %right Boundary 0 = Surface Recombination
%%
T = 300;            % K
e = 1.602E-19;      % C
kB = 1.38E-23;      % J/K
De = mue*kB*T/e;    % m^2/s
Dh = muh*kB*T/e;    % m^2/s
%D = 1*1e-9;        % m^2/s

nBG = wrev(nBG);
hBG = wrev(nBG);

tic
for it = 1:numt-1
 ti = t(it);

   for ix = 2:numx-1

    % Calculate Diffusion to next time Step
    n_x_t1(ix, it+1) = (n_x_t1(ix,it) + De*(dtAll(it)/...
      dx^2)*((n_x_t1(ix+1,it) - 2*n_x_t1(ix,it) + n_x_t1(ix-1,it))));
    h_x_t1(ix, it+1) = (h_x_t1(ix,it) + Dh*(dtAll(it)/...
      dx^2)*((h_x_t1(ix+1,it) - 2*h_x_t1(ix,it) + h_x_t1(ix-1,it))));

    % Recombination
    n_x_t1(ix, it+1) = n_x_t1(ix,it+1) - k2*(n_x_t1(ix,it+1)*...
      h_x_t1(ix,it+1) + n_x_t1(ix,it+1)*hBG(ix) )*dtAll(it);
    h_x_t1(ix, it+1) = h_x_t1(ix,it+1) - k2*(h_x_t1(ix,it+1)*...
      n_x_t1(ix,it+1) + h_x_t1(ix,it+1)*nBG(ix) )*dtAll(it);
    %%
    % Calculate Diffusion to next time Step
    n_x_t2(ix, it+1) = (n_x_t2(ix,it) + De*(dtAll(it)/...
      dx^2)*((n_x_t2(ix+1,it) - 2*n_x_t2(ix,it) + n_x_t2(ix-1,it))));
    h_x_t2(ix, it+1) = (h_x_t2(ix,it) + Dh*(dtAll(it)/...
```

```
    dx^2)*((h_x_t2(ix+1,it) - 2*h_x_t2(ix,it) + h_x_t2(ix-1,it))));

    % Recombination
  n_x_t2(ix, it+1) = n_x_t2(ix,it+1) - k2*(n_x_t2(ix,it+1)*...
    h_x_t2(ix,it+1) + n_x_t2(ix,it+1)*hBG(ix) )*dtAll(it);
  h_x_t2(ix, it+1) = h_x_t2(ix,it+1) - k2*(h_x_t2(ix,it+1)*...
    n_x_t2(ix,it+1) + h_x_t2(ix,it+1)*nBG(ix) )*dtAll(it);
  %%
  % Calculate Diffusion to next time Step
  n_x_t3(ix, it+1) = (n_x_t3(ix,it) + De*(dtAll(it)/...
    dx^2)*((n_x_t3(ix+1,it) - 2*n_x_t3(ix,it) + n_x_t3(ix-1,it))));
  h_x_t3(ix, it+1) = (h_x_t3(ix,it) + Dh*(dtAll(it)/...
    dx^2)*((h_x_t3(ix+1,it) - 2*h_x_t3(ix,it) + h_x_t3(ix-1,it))));

  % Recombination
  n_x_t3(ix, it+1) = n_x_t3(ix,it+1) - k2*(n_x_t3(ix,it+1)*...
    h_x_t3(ix,it+1) + n_x_t3(ix,it+1)*hBG(ix) )*dtAll(it);
  h_x_t3(ix, it+1) = h_x_t3(ix,it+1) - k2*(h_x_t3(ix,it+1)*...
    n_x_t3(ix,it+1) + h_x_t3(ix,it+1)*nBG(ix) )*dtAll(it);
end

%% no-flux Boundary Conditions

  n_x_t1(1,it+1) = Bleft*n_x_t1(2,it+1);
  n_x_t1(numx,it+1) = Bright*n_x_t1(numx-1,it+1);

  h_x_t1(1,it+1) = Bleft*h_x_t1(2,it+1);
  h_x_t1(numx,it+1) = Bright*h_x_t1(numx-1,it+1);

  n_x_t2(1,it+1) = Bleft*n_x_t2(2,it+1);
  n_x_t2(numx,it+1) = Bright*n_x_t2(numx-1,it+1);

  h_x_t2(1,it+1) = Bleft*h_x_t2(2,it+1);
  h_x_t2(numx,it+1) = Bright*h_x_t2(numx-1,it+1);

  n_x_t3(1,it+1) = Bleft*n_x_t3(2,it+1);
  n_x_t3(numx,it+1) = Bright*n_x_t3(numx-1,it+1);
```

```
    h_x_t3(1,it+1) = Bleft*h_x_t3(2,it+1);
    h_x_t3(numx,it+1) = Bright*h_x_t3(numx-1,it+1);

    %% Extraction

     nExtr1(it) = sum((x').*n_x_t1(:,it)*dx)/xMax^2;
     hExtr1(it) = sum((xMax- x').*h_x_t1(:,it)*dx)/xMax^2;

     nExtr2(it) = sum((x').*n_x_t2(:,it)*dx)/xMax^2;
     hExtr2(it) = sum((xMax- x').*h_x_t2(:,it)*dx)/xMax^2;

     nExtr3(it) = sum((x').*n_x_t3(:,it)*dx)/xMax^2;
     hExtr3(it) = sum((xMax- x').*h_x_t3(:,it)*dx)/xMax^2;

end
toc
%%
figure(1)
    plot(x,n_x_t1(:,1:100:end),'-k')

figure(2)
    plot(x,h_x_t1(:,1:100:end),'--k');

figure(3)
    semilogy(x, nBG); hold on
    semilogy(x, hBG,'--')
    hold off

   Nextr1 =  nExtr1+ hExtr1;
   Nextr2 =  nExtr2+ hExtr2;
   Nextr3 =  nExtr3+ hExtr3;

figure(4)
    semilogx(t(1:end-1),nExtr1); hold on
    semilogx(t(1:end-1),hExtr1)
    hold off

figure(5)
```

```
loglog(Nextr1(1:end-1),abs(diff(Nextr1)./diff(t(1:end-1))));
hold on
loglog(Nextr2(1:end-1),abs(diff(Nextr2)./diff(t(1:end-1))));
loglog(Nextr3(1:end-1),abs(diff(Nextr3)./diff(t(1:end-1))));
loglog(Nextr1,Nextr1.^2*k2,'--')
grid on; grid minor; grid minor
hold off
```

A.1.6. Temperature-dependent time resolved Photoluminescence

The temperature of the sample was controlled by a closed cycle cryostat (Oxford Instruments, Optistat Dry TLEX). For excitation a mode-locked Ti:sapphire laser (Coherent, Chameleon Ultra) with a pulse width of 140fs and a repetition rate of 80MHz was used. The photoluminescence transients were recorded by a Hamamatsu Universal Streak Camera C10910 coupled to an Acton SpectraPro SP2300 spectrometer. The camera was used in synchroscan mode to allow for a $2ns$ time window and a FWHM of the instrumental response function of $44ps$.

A.1.7. Temperature dependent TDCF Experiments

To extract the activation energy datasets are replotted as a function of internal electric field for the example of 1.55 eV excitation in Figure A.4. The field dependence of free charge generation (plotted in a log-log scale) exhibits the characteristic shape predicted and measured for D-A BHJ blends [209–211], with an apparent plateau at lower fields followed by a continuous rise that becomes less steep with increasing temperature.

A.2. Fluence dependent Charge Generation in MEH-PPV:PCBM blends

Several types of devices were screened for temperature dependent charge generation experiments. The deficits of blends made from MEH-PPV and PCBM are insurmountable for these experiments because of fluence dependent field dependence

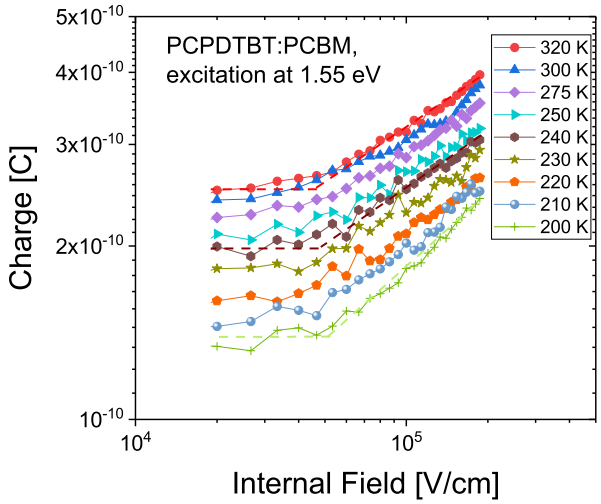

Figure A.4.: Temperature and electric field dependent charge generation in the 110 nm thick PCPDTBT:PCBM blend for an excitation energy of 1.55 eV. A flat band potential of +0.8 V was used in the calculation of the internal electric field.

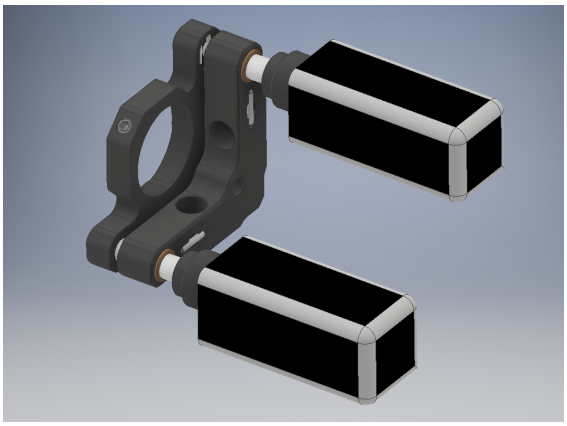

Figure A.5.: Motorized Mirror used for TDCF and TAS to increase the beam-pointing stability.

of charge generation probably caused by fast initial non-geminate recombination which severely effects TDCF traces especially at low temperatures.

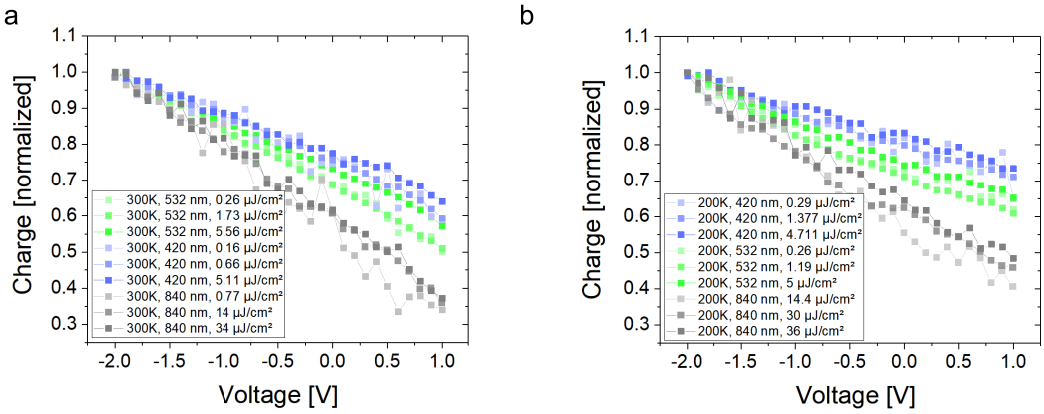

Figure A.6.: Charge generation for MEH-PPV:PCBM devices measured at the shortest possible delay of 4 ns and at different fluences at (a) 300 K and (b) 200 K.

Appendix B

Publications

Kurpiers, J., Ferron, T., Roland, S., Thiede, T., Jaiser, F., Albrecht, S., Janietz, S., Collins, B. A., Howard, I., Neher, D. "Probing the Pathways of Free Charge Generation in Organic Bulk Heterojunction Solar Cells" *Nature Communications* **9** 2038 (2018).

Hosseini, S. M., Roland, S., Kurpiers, J., Chen, Z., Zhang, K., Huang, F., Armin, A., Neher, D. and Shoaee, S. "Impact of bimolecular recombination on the fill factor of a fullerene and non-fullerene based solar cell: a comparative study of charge generation and extraction." *submitted to Advanced Energy Materials* (2018)

Kurpiers, J., and Neher, D., "Dispersive Non-Geminate Recombination in an Amorphous Polymer:Fullerene Blend." Scientific Reports **6** 26832 (2016).

Kurpiers, J., Daniel M Balazs, Andreas Paulke, Steve Albrecht, Ilja Lange, Loredana Protesescu, Maksym V Kovalenko, et al. "Free Carrier Generation and Recombination in PbS Quantum Dot Solar Cells." *Appl. Phys. Lett.* **108** 103102 (2016).

Paulke, A., Stranks, S.D., Kniepert, J., Kurpiers, J., Wolff, C.M., Schön, N., Snaith, H.J., Brenner, T.J.K., and Neher, D.. "Charge Carrier Recombination Dynamics in Perovskite and Polymer Solar Cells" *Appl. Phys. Lett.* **108** 113505 (2016).

Kniepert, J., Lange, I., Heidbrink, J., Kurpiers, J., Brenner, T.J.K.; Koster, J.A. and Neher, D. "Effect of Solvent Additive on Generation, Recombination, and Extraction in PTB7:PCBM Solar Cells: A Conclusive Experimental and Numerical Simulation Study." *Journal of Physical Chemistry C* **119** 8310 (2015).

Roland, S., Schubert, M., Collins, B.A., Kurpiers, J., Chen, Z.H., Facchetti, A., Ade, H., and Neher, D. "Fullerene-Free Polymer Solar Cells with Highly Reduced Bimolecular Recombination and Field-Independent Charge Carrier Generation." *Journal of Physical Chemistry Letters* **16** 2815 (2014).

Albrecht, S., Janietz, S., Schindler, W., Frisch, J., Kurpiers, J., Kniepert, J., Inal, S., Neher, D. et al. "Fluorinated Copolymer PCPDTBT with Enhanced Open-Circuit Voltage and Reduced Recombination for Highly Efficient Polymer Solar Cells." *Journal of the American Chemical Society* **36** 14932 (2012).

Albrecht, S., Schindler, W., Kurpiers, J., Kniepert, J., Blakesley, J.C., Dumsch, I., Allard, S., Fostiropoulos, K., Scherf, U., and Neher, D. "On the Field Dependence of Free Charge Carrier Generation and Recombination in Blends of PCPDTBT/PC70BM: Influence of Solvent Additives." *Journal of Physical Chemistry Letters* **5** 640 (2012).

B.1. Author Contribution

The experimental work including the built-up of the TDCF and TAS setups, development of the electronics part and automation control programming for all presented publications and supporting information in this thesis was performed by the author. TDCF data analysis, fitting and modeling was implemented and carried out by the author with the help of Dieter Neher. The data analysis programming code was further improved by Andreas Paulke and John A. Love.

For Kurpiers *et al. Appl. Phys. Lett.* **108** 103102 (2016), the author, Maria A. Loi and Dieter Neher wrote the main manuscript text, Loredana Protesescu synthesized the quantum dots, Daniel M. Balazs prepared the devices, the author performed TDCF and BACE experiments, Steve Albrecht and Ilja Lange performed BACE and steady state measurements. The author prepared all figures. All authors and John A. Love reviewed the manuscript. For the presented publication; Jona Kurpiers and Dieter Neher, *Scientific Reports* **6** 26832 (2016), the author performed all experiments including sample preparation and optimization. Both authors analyzed the data and wrote the manuscript. John A. Love, Andreas Paulke and Steve Albrecht revised the manuscript. For Kurpiers *et al. Nature Communications* **9**, 2038 (2018), the author and Steffen Roland prepared the samples and devices used for all measurements according to a further optimized device preparation recipe originally provided by Steve Albrecht. The author performed all TDCF measurements, Steffen Roland, Tobias Thiede and the author performed PL, EL, EQE and Absorbance. Silvia Janietz and Anne Katholing synthesized 1F-PCPDTBT. Thomas Ferron and Brian A. Collins completed all X-ray diffraction measurements and analysis for structural characterization. Ian Howard and Marius Jakoby performed temperature dependent transient PL measurements and Burkhard Stiller provided AFM pictures for the supporting information. Dieter Neher supervised the project. The author, Dieter Neher, Thomas Ferron and Steffen Roland wrote the manuscript, and all authors revised the final manuscript. For all publications listed in Appendix B the author contributed with data, data analysis and preparation of the manuscripts.

Potsdam, May 21, 2019

Prof. Dr. Dieter Neher

Appendix C

Conference Contributions

European Conference on Molecular Electronics, 2017, Dresden, Germany – Poster entitled: "Charge Generation in Polymer Fullerene Solar Cells".

New Trends and Faces IV Workshop, 2016, Stellenbosch, South Africa – talk entitled: "Time Delayed Collection Field and Bias Assisted Charge Extraction" and second talk: "Hot or Not? Temperature Dependent Charge Generation in Polymer-Fullerene Solar Cells"

DPG spring meeting, 2016, Regensburg, Germany – talk entitled: "Rapid Non-geminate Recombination in Organic Solar Cells"

ICANS 2015, 2015, Aachen, Germany – talk entitled: "Charge carrier dynamics in PbS quantum dot solar cells"

MRS Spring meeting, 2015, San Francisco, USA – Poster entitled: "Hot charges speed up non geminate recombination but have no effect on device performance"

XVP, 2014, - Poster entitled: "Additive-assisted supramolecular manipulation of polymer:fullerene blend phase morphologies and its influence on photophysical processes"

BCCMS, 2013, Bremen, Germany – Poster entitled: "Charge carrier dynamics in PCDTBT:PC70BM Bulk heterojunction solar cells"

Appendix D

Acknowledgment

My greatest thanks to Prof. Dieter Neher, for the freedoms he has given me during my work has always granted, and the trust on which these establish for hours of discussions, the constant support and relentless way of questioning arguments and results. His unlimited assistance and wise guidelines enabled several publications in high impact journals being also the basis of this thesis.

An indescribably big *thank you* to Frank, was there ever something that you could not help me with? Your help with purchase requests and endless orders for optical components and polimeric materials never ceased.

I would also like to thank every member of the "Soft Matter Physics" group, especially; Apu, Tobias, Juliane, Steffen, Andreas, Steve and Christian.

The basis of many investigations were the synthesized fluorinated polymers of the team of Silvia Janietz, Fraunhofer IAP, and special thanks to Eileen Katholing, who did the lab work. For their willingness to discuss and their commitment in several collaborations during the last years, I especially thank Brian Akira Collins, Koen Vandewal, Andreas Hofacker, Frédéric Laquai, Marius Jakoby and Ian Howard.

I also want to thank my girlfriend Hanna, she was always supporting me in focusing on the endless experiments, sometimes waking up every two hours during the night when the experiments were conducted. She has taken care of our child Noam every day.

Appendix E

Thesis Declaration

I, Jona Kurpiers, Matrikel-Nr. 779662, hereby certify that this thesis

> *Probing the Pathways of Free Charge Generation and Recombination in Organic Solar Cells: The Role of Excess Energy and Dispersive Effects.*

has been written by me, that it is the record of work carried out by me, that i did not use source material or aids other than those mentioned and that it was not submitted to any other university.

Potsdam, May 21, 2019

Dipl. Phys. Jona Kurpiers